

# **Quantitative Analysis of Thermophysical Properties of Lava Flows on Earth and Mars**

by

**Christine Marie Simurda**

Bachelor of Arts, Washington University in St Louis, 2011

Submitted to the Graduate Faculty of

The Dietrich School of Arts and Sciences in partial fulfillment

of the requirements for the degree of

Doctor of Philosophy

University of Pittsburgh

2019

UNIVERSITY OF PITTSBURGH  
DIETRICH SCHOOL OF ARTS AND SCIENCES

This dissertation was presented

by

**Christine Marie Simurda**

It was defended on

March 1, 2019

and approved by

William Harbert, Professor, University in Pittsburgh

Brian Stewart, Associate Professor, University of Pittsburgh

Eitan Shelef, Assistant Professor, University of Pittsburgh

David Crown, Senior Scientist, Planetary Science Institute

Dissertation Director: Michael Ramsey, Professor, University of Pittsburgh

Copyright © by Christine Simurda

2019

# **Quantitative Analysis of Thermophysical Properties of Lava Flows on Earth and Mars**

Christine Marie Simurda, PhD

University of Pittsburgh, 2019

Multi-instrument approaches, at different spatial and spectral resolutions, are used to investigate the thermophysical properties of lava flows at the subpixel scale. Development of remote sensing aerial and terrain technology has provided higher spatial resolution data that can improve the derivation of surface properties from satellite datasets. TIR data have applications to interpret surface properties of planetary bodies, but are limited by the lower spatial resolution. This research utilizes multi-instrument approaches to improve the understanding of the subpixel surface properties derived from TIR data, specifically to quantify the presence of shadowing, mixed pixels, and complex surfaces with horizontal mixing and vertical layering. Visible data, with higher spatial resolutions, are used to interpret the surface topography and/or structures and TIR data, with lower spatial resolutions, are used to understand thermal properties to derive particle size and composition. Two study areas were the focus of this research: a terrestrial analog at the North Coulee, part of the Mono-Inyo Crater System, and the Daedalia Planum flow field on Mars. At the North Coulee, studies assessed the effect of shadows on ATI and aimed to better understanding the relationship between mixed pixels (with subpixel particle and block sizes variability) and ATI. The locations of shadows were identified using a DEM and a correction applied based on the areal percentage of a pixel in shadow. Analysis of the relationship



between mixed pixels and ATI demonstrates that the current assumption of uniform material at the pixel scale will cause incorrect derivation of moderate and coarse materials at higher ATI values. The studies on Daedalia Planum, Mars, aim to determine the cause of the thermophysical variation between lava flows and define the areal percentage of dust, sand, and lava outcrops on the flow surfaces. Through this quantitative analysis, the variability was determined to be caused by different vertical layering and horizontal mixing of these components and that some flows have up to 40% identifiable lava outcrops with a dust layer of 0.2 mm. These techniques demonstrate the application of multi-instrument approaches to investigate complex surfaces with mixtures and layering below the spatial resolution of current TIR instruments.

## Table of Contents

Preface.....	xxii
1.0 Introduction.....	1
2.0 A Quantitative Error Correction Approach for Shadowing in Apparent Thermal Inertia Data.....	5
2.1 Introduction .....	5
2.2 Background .....	7
2.2.1 Geologic History of the Mono-Inyo Crater System .....	7
2.2.1.1 Age Constraints on the Mono Craters .....	8
2.2.1.2 Identifying the Source of the Mono Craters Section .....	8
2.2.2 North Coulee.....	10
2.2.3 Advanced Spaceborne Thermal Emission and Reflection Radiometer (ASTER).....	12
2.2.4 Thermal Inertia (TI) and Apparent Thermal Inertia (ATI).....	14
2.2.5 Shadowing Effects .....	16
2.3 Methods .....	18
2.3.1 Calculating Apparent Thermal Inertia .....	21
2.3.2 Products Derived from Digital Terrain Models: Slope and Hillshade.....	25
2.3.3 Identifying Areas Affected by Shadowing Errors.....	27
2.3.4 Calculating Correction for Shadowing Errors.....	32
2.4 Results.....	34
2.4.1 Identification of Shadowed Pixels.....	34

2.4.2 Single Value Correction vs. Adjusted Correction .....	35
2.4.3 Evaluation of Surface Temperature and Albedo Corrections .....	36
2.4.4 ATI Correction Evaluation .....	40
2.5 Conclusion .....	42
2.6 Acknowledgements .....	43
<b>3.0 Assessing Subpixel Surface Roughness and Block Size Distribution to Improve</b>	
<b>Thermal Inertia Interpretations .....</b>	<b>44</b>
3.1 Introduction .....	44
3.2 Background .....	46
3.2.1 Geologic Setting of the North Coulee .....	46
3.2.2 WorldView-2.....	48
3.2.3 Apparent Thermal Inertia and Particle Size .....	49
3.2.4 Sub-pixel Particle Size Mixtures.....	50
3.2.5 Photogrammetry .....	51
3.2.5.1 Areal and Terrestrial Techniques .....	54
3.2.6 Roughness Calculations .....	55
3.3 Methods .....	57
3.3.1 Datasets .....	59
3.3.2 Field Campaign .....	61
3.3.3 Categories: Particle Sizes and Vegetation .....	63
3.3.4 Photogrammetry Dataset and Category Assessment.....	67
3.3.5 Roughness Calculations from Photogrammetry Dataset .....	69
3.3.6 Categories and ATI.....	69

<b>3.4 Results.....</b>	<b>70</b>
<b>3.4.1 Category Evaluation .....</b>	<b>70</b>
<b>3.4.2 Roughness Calculation of Categories .....</b>	<b>73</b>
<b>3.4.3 Location Distribution.....</b>	<b>75</b>
<b>3.4.4 Category Distributions and ATI.....</b>	<b>78</b>
<b>3.4.5 Improved Relationship between ATI and Mixed Surface Properties .....</b>	<b>80</b>
<b>3.5 Conclusions .....</b>	<b>82</b>
<b>3.6 Acknowledgements .....</b>	<b>83</b>
<b>4.0 The Unusual Thermophysical and Surface Properties of the Daedalia Planum</b>	
<b>Lava Flows .....</b>	<b>85</b>
<b>4.1 Introduction .....</b>	<b>85</b>
<b>4.2 Background .....</b>	<b>87</b>
<b>4.2.1 Geologic Setting.....</b>	<b>87</b>
<b>4.2.2 Thermophysical Response and Thermal Inertia.....</b>	<b>90</b>
<b>4.2.3 Dust Cover .....</b>	<b>91</b>
<b>4.2.4 Mixed Surfaces .....</b>	<b>92</b>
<b>4.2.5 Previous Work.....</b>	<b>93</b>
<b>4.3 Methods .....</b>	<b>94</b>
<b>4.3.1 Datasets .....</b>	<b>94</b>
<b>4.3.2 Decorrelation Stretch.....</b>	<b>97</b>
<b>4.3.3 Geomorphologic Analysis.....</b>	<b>98</b>
<b>4.3.4 Thermophysical Analysis .....</b>	<b>99</b>
<b>4.3.5 Regions of Interest.....</b>	<b>100</b>

4.3.6 Defined Categories .....	102
4.4 Results.....	103
4.4.1 Thermal Inertia of the Flow Field .....	104
4.4.2 Unique Diurnal Signatures of the Flow Field .....	105
4.4.3 Thermal Response of Categories B and C Flows .....	105
4.4.4 Thermal Response of Categories A and D Flows .....	108
4.4.5 Latitude Distribution .....	110
4.4.6 Correlation Between Thermal Response and Surface Morphology.....	111
4.5 Conclusions .....	114
4.6 Acknowledgements .....	116
5.0 Quantifying the Vertical Layering and Horizontal Mixing of Dust, Sand, and Lava Outcrops on Lava Flow Surfaces in Daedalia Planum, Mars .....	118
5.1 Introduction .....	118
5.2 Background .....	119
5.2.1 Geologic Setting: Daedalia Planum .....	119
5.2.2 Thermal Conductivity Dominating Thermal Inertia ~ Particle Size Implications .....	121
5.2.3 Skin Depth .....	122
5.2.4 Complications for Thermal Inertia: Presence of Vertical Layering .....	123
5.2.5 Thermal Numerical Models: Horizontal Mixing and Vertical Layering...	124
5.2.5.1 MARSTHERM: A Horizontal Mixing Thermal Model.....	125
5.2.5.2 KRC: A Vertical Layering Thermal Model .....	125
5.3 Methods .....	126

5.3.1 Datasets .....	127
5.3.2 A Dual Method Approach to Interpreting Thermal Inertia .....	128
5.3.3 MARSTHERM Modeling of Horizontally Mixed Areas.....	131
5.3.4 Modeling Vertically Layered Units in the KRC Model.....	133
5.3.4.1 Horizontal Mixture of Vertically Layered Units .....	135
5.3.5 Look-Up Tables Matched to THEMIS Data .....	136
5.3.6 Supervised Classification of Lava Outcrops in HiRISE Data.....	138
5.3.7 ROTO Data.....	140
5.4 Results.....	141
5.4.1 Mixtures of Single Layer Systems .....	141
5.4.2 Layered Units .....	144
5.4.3 Horizontal Mixtures of Layered Systems .....	146
5.4.4 ROTO Data.....	150
5.5 Conclusion .....	153
5.6 Acknowledgements .....	155
6.0 Concluding Remarks .....	157
Appendix A .....	163
Appendix B .....	167
Appendix C .....	171
C.1 Daytime High/Low Assignment and $\Delta T$ .....	172
C.2 Nighttime High/Low Assignment and $\Delta T$ .....	174
Appendix D .....	176
Appendix E .....	179

<b>Bibliography .....</b>	<b>182</b>
---------------------------	------------

## List of Tables

Table 1. ASTER profile with spatial and spectral resolutions of each band (Yamaguchi et al., 1998). .....	13
Table 2. List of datasets and derived products used to identify and correct shadowing errors (Yamaguchi et al., 1998; USGS, 2013 & 2018). .....	20
Table 3. ASTER dataset used to calculate ATI. ....	24
Table 4. Dataset descriptions of instrument spatial resolution and spectral range with study applications (Yamaguchi et al., 1998; DigitalGlobe, 2013). ....	60
Table 5. Description of the four category types, three based on particle and block sizes and the fourth on vegetation, used to define surface characteristics. ....	65
Table 6. Category descriptions and maximum calculated roughness range from the photogrammetry dataset. ....	74
Table 7. Summary description of datasets, including any instrument limitations, used to conduct this study. ( <sup>a</sup> Malin et al., 2007; <sup>b</sup> McEwen et al., 2007; <sup>c</sup> Christensen et al., 2004; <sup>d</sup> Ferguson et al., 2006; <sup>e</sup> Ruff and Christensen, 2002). ....	95
Table 8. The thermophysical response of the four flow categories based on daytime and nighttime brightness temperature differences. The assigned color of each category correlates to Figures 4 and 6. ....	103
Table 9. Statistical summary of the correlation between surface morphology and thermophysical response. Smooth flows predominantly display a category B or C response with inverse day and night delta brightness temperatures ( $\pm\Delta T$ ; see section 4.3.5 for explanation) in relation to the flow field as a whole, whereas rough flows principally have category C or D responses. ....	111



Table 10. Applications of visible and thermal infrared datasets to investigate the lava flows in Daedalia Planum ( <sup>a</sup> Malin et al., 2007; <sup>b</sup> McEwen et al., 2007; <sup>c</sup> Christensen et al., 2004; <sup>d</sup> Ferguson et al., 2006; <sup>e</sup> Ruff and Christensen, 2002). .....	128
Table 11. Description of the ideal components used in the KRC model from Putzig and Mellon (2007) and Ferguson et al. (2006). .....	130
Table 12. Input parameters for MARSTHERM to model single layered, horizontally mixed systems (Putzig, 2013). .....	132
Table 13. KRC input parameters, including a description and how it is derived, used to calculate vertically layered diurnal temperatures and thermal inertia (Kieffer, 2013). .....	134
Table 14. ROTO data collection parameters.....	141
Table 15. Results of the comparison between the KRC vertically layered and horizontally mixed diurnal curves and THEMIS derived temperatures at two specific times. These values represent the potential areal percentages of layered sand and lava outcrops layered components (the bold and underlines percentages corresponding to the HiRISE classification results).....	147
Table 16. High/Low daytime temperature assignment for each flow in each THEMIS stamp with surface morphology and category descriptions.....	172
Table 17. Daytime $\Delta T$ for each flow in each THEMIS stamp with surface morphology and category descriptions. ....	173
Table 18. High/Low nighttime temperature assignment for each flow in each THEMIS stamp with surface morphology and category descriptions. ....	174
Table 19. Nighttime $\Delta T$ for each flow in each THEMIS stamp with surface morphology and category descriptions. ....	175

Table 20. THEMIS stamp information used to define the collection parameters used in the thermal numerical models.....	177
---	-----

## List of Figures

Figure 1. Conceptual diagram created by Peacock et al. (2015) depicting the subsurface geologic model based on resistivity features. Arc-shaped dike swarms connected the granodioritic crystal-melt mush columns (C1 and C3) to the surface, producing the Holovene Mono Craters. ....	9
Figure 2. Aerial image of Mono Craters System with the red rectangle showing the location of the North Coulee (WorldView-2 images courtesy of DigitalGlobe Foundation). North Coulee outline in black for study boundary context. ....	11
Figure 3. Illustration of the shadows created by topographic slopes such as those along the edge of the North Coulee. The length of the shadow is dependant on the solar elevation angle ( $\sigma$ ). ...	17
Figure 4. Workflow for calculating apparent thermal inertia (ATI) values from ASTER VNIR and TIR datasets.....	23
Figure 5. ATI calculated from ASTER TIR and VNIR data with red outline of the North Coulee (Yamaguchi et al., 1998). North facing slopes display unusually high ATI value.....	24
Figure 6. (A) Slope data demonstrating the variation in surface slope on the North Coulee. The steepest slopes are located along the coulee edge and the top displays significant variation. (B) Hillshade image displaying the degree to which an area is affected by shadows with a depiction of the sun direction for context. ....	26
Figure 7. ROIs (black regions) defined by values less than 175 in the hillshade data are used to identify areas with significant shadowing.....	28
Figure 8. ROIs of pixels significantly affected by shadowing at the spatial resolution of the ASTER TIR temperature data (Yamaguchi et al., 1998). The correction applied to each of the	

idenitified pixels is based on the areal percentage of the hillshade ROIs multiplied by the maximum identified correction.....	30
Figure 9. ROIs of pixels significantly affected by shadowing at the spatial resolution of ASTER VNIR data (Yamaguchi et al., 1998). The correction applied to each of the idenitified pixels is based on the areal percentage of the hillshade ROIs multiplied by the maximum identified correction. ....	31
Figure 10. Photograph taken in the field depicting the typical slope material along the sides of the North Coulee including trees, boulders, finer particles and moderate rocks. ....	33
Figure 11. Comparison of the original and corrected daytime temperature data with black outline of the North Coulee demonstrating significant improvement to affected pixels in the corrected data. ....	38
Figure 12. Comparison of the original and corrected albedo data with white outline of the North Coulee demonstrating significant improvement to affected pixels in the corrected data. ....	39
Figure 13. Comparison of the original and corrected ATI data with a red outline showing the extent of the North Coulee. The results demonstrate significant improvement to affected pixels in the corrected data. ....	41
Figure 14. Field photography illustrating the range of grain sizes present on the surfae of the North Coulee, specifically at ‘the bowl’ study area.....	47
Figure 15. Description of the process used in Structure from Motion (SfM) in which multiple, overlapping photographs are used to produce a 3D construction of the surface (Westoby et al., 2012). ....	53
Figure 16. Vertical profile of a simple surface demonstrating the calculation of surface roughness normalized to a slope. ....	56

Figure 17. Flowchart of the methods used to better understand the relationship between particle and block size distributions within a pixel (mixed pixels) and ATI values.....	58
Figure 18. Photographs of the sampling areas investigated during the field campaign: (A) coulee slope, (B) ‘the Bowl’, and (C) fine grained deposit.....	62
Figure 19. Examples of the four category types overlain on WorldView-2 data to demonstrate the variation seen on the surface (DigitalGlobe, 2013). .....	66
Figure 20. 3D rendering of the point cloud from photographs taken during the field with dots representing the location of image captures. WorldView-2 image of the northeast corner of the North Coulee with yellow arrow demonstrating the perspective of the 3D point cloud rendering (DigitalGlobe, 2013). .....	68
Figure 21. Northeast lobe of the North Coulee study site. (A) DTM, created from the point cloud data, to interpret local topographic slopes. (B) Point cloud density for visual interpretation of surface particle and block size distribution (5 cm). (C) Category shapefiles defined from WorldView-2 data to determine the accuracy of particle size identification (DigitalGlobe, 2013). Categories: red = coarse, orange = moderate, blue = fine, and green = vegetation. (D) ATI data with identified pixels 1 and 2 labeled for discussion. ....	72
Figure 22. Roughness calculation from the density point cloud with a kernel size of 2 m demonstrating the variation present in ‘the bowl’ study area. ....	74
Figure 23. Category distributions (red=coarse, orange=moderate, blue=smooth, and green=trees) on WorldView-2 data with white outline of the North Coulee boundaries (DigitalGlobe, 2013). This study focused on the top of the coulee to avoid any complications from significant slopes.	76
Figure 24. Calculated ATI values from ASTER visible and thermal infrared data displaying the variability in the study area. The red outline displays the boundaries of the North Coulee. ....	77

Figure 25. Ternary plot of the three particle size categories demonstrating the relationship between mixed pixels and ATI values on the surface of the North Coulee. The sample interval for the ATI values is determined by five equal divisions. ....	79
Figure 26. THEMIS daytime thermal IR brightness temperature mosaic by Edwards et al. (2011) with lava flow margins (white, dashed) by Crown et al. (2015). The orange dot signifies the center location of Figure 27a-c. The MOLA color inset for regional context shows the study area denoted with the black rectangle. Bounding coordinates: longitude 120.4-127.5° W and latitude 22.0-26.8° S. ....	89
Figure 27. The lava flows in Daedalia Planum shown at various spatial scales: (a) daytime brightness temperature mosaic (Edwards et al., 2011) with the flow boundaries (white, dashed) of Crown et al. (2015), (b) nighttime brightness temperature mosaic (Edwards et al., 2011), and (c) thermal inertia (Ferguson et al., 2006) showing the thermophysical variations (the center of this region is shown as the yellow dot in Figure 26). CTX images of representative (d) rough (P01_001590_1567) and (e) smooth (P18_008038_1544) surface morphologies (black and white boxes respectively indicate the areas shown in (f) and (g)). Representative HiRISE images showing the (f) rough (ESP_036731_1570) and (g) smooth (ESP_036586_1560) morphologies. ....	97
Figure 28. THEMIS IR decorrelation stretch (DCS) of a mosaic of stamps I52299002, I51737003, and I50713002 using bands (a) 6-4-2, (b) 8-7-5, and (c) 9-6-4. The minor color variations (and the consistency of color between the images) indicates that significant compositional variability is likely not present. ....	98
Figure 29. Representative ROI distribution (category colors defined in Table 8) overlain on the daytime brightness temperature mosaic (from Edwards et al., 2011) with flow boundaries in	

white (dashed) by Crown et al. (2015). Location within the study area designated by the white arrow in Figure 31.....	101
Figure 30. Possible idealized configurations (a, b, e, f) of surficial deposits covering lava outcrops in the Daedalia Planum study site. Simple configurations are shown of (a) a vertically layered system with dust uniformly covering the lava flow, and (b) a horizontally mixed system with sand deposited in low-lying regions and the lava flow surface free of dust. HiRISE images displayed at the same scale showing rough flow surfaces that correspond to (c) category B (ESP_046450_1535) and (d) category C (ESP_041940_1570) thermophysical responses. More complex scenarios showing both horizontal mixing and vertical layering with sand deposited in low-lying regions for (e) category B rough flows with a greater areal coverage of sand and/dust and (f) category C rough flows with the greatest abundance of exposed lava outcrops.....	108
Figure 31. THEMIS nighttime brightness temperature mosaic (from Edwards et al., 2011) of the Daedalia Planum study area showing the categorized flows (bounding coordinates: longitude 120.4-127.5° W and latitude 22.0-26.8° S). The Crown et al. (2015) flow boundaries are shown with white dashed lines and the flow colors correspond to the thermophysical response categories (Table 8). The white arrow marks the location of Figure 29.....	109
Figure 32. Delta brightness temperature ( $\Delta T$ ) values shown for each flow, grouped by flow category and surface morphology. These delta values were computed by calculating the difference between the average value for the THEMIS stamp and average value for each flow in order to compare values between stamps with different observation parameters (see section 4.3.5 for explanation; Christensen et al., 2004). Data were further separated between (a) rough and (b) smooth surface morphologies. ....	114

Figure 33. Flowchart of the method combining modeling and remote sensing techniques to identify the horizontal mixing and vertically layering of dust, sand, and lava outcrops present on the surface. ....	130
Figure 34. Seasonal curves for dust at four different times of day (6 hour increments) to demonstrate the seasonal and diurnal variability. The diurnal curve usually reaches the peak at ~12:00, but the maximum temperture reached by the surface varies by ~60 K depending on the season. ....	137
Figure 35. (A) Supervised classification of a rough category C flow with ~40% lava outcrops in white and sand/dust in black and (B) HiRISE data from which the supervised classification was derived (PSP_002711_1550). ....	139
Figure 36. Modeled diurnal brightness temperature curves of a (A) 90% sand and 10% rock mixture and (B) 60% dust and 40% rock mixture that best match the THEMIS data for a category C rough flow. The local time for two THEMIS stamps are denoted by red and blue circles (day = 16:31 and night = 4:46). ....	143
Figure 37. Diurnal temperature curves of (A) rock (lava outcrop) with increasing thickness of dust cover and (B) sand with increasing thickness of dust cover. These plots show how increasing dust thickness masks the thermal signature of the lower layer and that the dust has a greater impact on the thermal response of rock. ....	145
Figure 38. Diurnal curve of a horizontally mixed layered system that best matches the THEMIS data for category C rough flows 5, 18, and 29. The local time for THEMIS stamps are shown (day: 16:31 and night: 4:46). ....	148
Figure 39. Temperature differences between ROTO images with lava flow boundaries shown in black (Crown et al., 2015) with higher negative values suggestive of fine grained surfaces. (A)	



I68222002 (nadir) minus I68197002 (-13°), (B) I68197002 (-13°) minus I68172002 (-28°), and (C) I68222002 (nadir) minus I68172002 (-28°). Note that these comparisons always follow the formula (later local time minus earlier local time). .....	152
Figure 40. Hillshade calculated for 07:51 local time on May 31, 2014.....	163
Figure 41. Hillshade calculated for 09:51 local time on May 31, 2014.....	164
Figure 42. Hillshade calculated for 13:51 local time on May 31, 2014.....	164
Figure 43. Hillshade calculated for 15:51 local time on May 31, 2014.....	165
Figure 44. Hillshade calculated for 17:51 local time on May 31, 2014.....	165
Figure 45. Hillshade calculated for 19:51 local time on May 31, 2014.....	166
Figure 46. Kernel size 20 m roughness calculation. ....	167
Figure 47. Kernel size 15 m roughness calculation. ....	168
Figure 48. Kernel size 10 m roughness calculation. ....	168
Figure 49. Kernel size 5 m roughness calculation. ....	169
Figure 50. Kernel size 2 m roughness calculation. ....	169
Figure 51. Kernel size 1 m roughness calculation. ....	170
Figure 52. Kernel size 0.102422 m roughness calculation (the automatically assigned value). .	170

## **Preface**

I would like to thank Michael Ramsey, David Crown, and Stephen Scheidt for their guidance and support through these projects. I am grateful to William Harbert, Eitan Shelef, and Brian Stewart as members of my defense committee for all of their advice and recommendations.

I would also like to thank my family for the unending support through this process. Without your guidance and love, I would not have succeeded in this endeavor. To most of all my husband, thank you for helping me through this process (especially at the worst moments) and teaching me to see life in the best of ways. Your advice and kindness have been and always will be invaluable to me.

## **1.0 Introduction**

Remote sensing datasets provide an effective non-destructive method to investigate the surface of Earth or Mars, especially dangerous or hard to reach locations that pose a significant risk to local communities. Another benefit of these datasets is the continued collection over a designated site to provide a basis for many studies of changing surfaces. Faster repeat and continued collection times create detailed temporal collections of these datasets that provide observations of changing surface structures and environmental conditions. With the increasing access to higher spatial and spectral resolution datasets, the application of multi-instrument approaches provides critical information to understanding the surface properties at a significantly higher detail and accuracy. For examples, higher spatial resolution visible (VIS) datasets can be used to improve the techniques used to derive surface properties derived from thermal infrared (TIR) data with a lower spatial resolution.

Each of the wavelength regions in the electro-magnetic spectrum provide unique information about the surface. VIS remote sensing has long been used to define the geological context of morphologic features and provide information regarding composition, producing numerous maps that depict the morphology and geology of a region. VIS instrumentation usually has relatively high spatial resolution compared to other instruments, allowing for greater details to be discerned. The properties of the TIR region allow these investigations to derive information about the physical properties of the surface materials including particle size and the presence of volatiles. This is attributed to the fact that in the TIR region, instruments measure the radiation emitted from a body or surface due to absorption of solar radiation, convection, and conduction. One of the most useful derived products from TIR data is thermal inertia, which represents the

resistance of a material to changes in temperature over a diurnal cycle and is calculated from the thermal conductivity, thermal capacity, and density of the material. However, TIR instruments have a significantly lower spatial resolution compared to VIS instrumentation. By creating a method combining data from multiple wavelength regions, a more detailed understanding of the surface properties and structure is possible.

Topographic shadowing and the presence of mixed pixels, with variations in particle and block sizes, on the surface significantly complicate the derivation of surface materials from TIR data. Shadows will lower the daytime temperature of the material and ultimately increase the derived apparent thermal inertia (ATI) value. For an affected area, this error would result in the interpretation as containing larger particle sizes than is actually present. This effect can vary dramatically depending on the topography of the study area. For locations with high topographic reliefs, this error can be particularly hinder because a significant portion of the scene may not be analyzed due to cast shadows. Another complex issue to solve in thermal infrared datasets is caused by the assumption of pure pixels on the surface with uniform material properties. Inspection of higher spatial resolution visible data demonstrates that surfaces are significantly more complex with varying mixtures of different particle and block sizes displaying significantly different thermal inertia responses. By continuing to assume uniform properties at the spatial resolution of the dataset, the surface material properties will either be under- or overestimated, depending on the distribution of particle and block sizes on the surface. With continued advances in technology creating higher spatial and spectral resolution instruments, these complex surfaces can be studied in greater detail and the subpixel surface properties can be superficially targeted.

Determination of grain size and composition from remote sensing data provides critical information for the interpretation of eolian and volcanic processes on planetary surfaces such as

Mars. However, infrared (IR) spectral analysis can be hindered by the presence of optically thin (and in some places, very thick) dust deposits, which appear to occur over the lava flow fields in Daedalia Planum, Mars. Typically, Martian dust is spectrally-bland and globally homogenized, thus obscuring the accurate spectral signatures of the underlying bedrock. However, high resolution image analysis of wind streaks in this region by Edgett and Malin (2000) demonstrate the presence of a thin cover of fine-grained sand rather than extensive thick dust deposits. This suggests coarse particles may not be fully obscured by a cover of fines (thick vertical layering) and these complex surfaces contain both horizontal mixing and vertical layering of different particle and block sizes that is currently misinterpreted as a single unit. Laboratory studies that examined the thermal conductivity of different mixtures of material with various grain sizes found that fine particles within a large pixel area will dominate (Mellon et al., 2014). Thus, the averaged spectral result derived from a large pixel (e.g., TES at 3 km) may be overestimating the dust and at the very least may be missing the small scale spatial variability of the surface. Modeled thermal conductivity measurements under Mars conditions suggest that the detection of coarse-grained particles are obscured by interstitial fines and low thermal inertia regions may be explained by a mixture of coarse plus fine grained material (Mellon et al., 2014). For the lava flows of Daedalia Planum, such a mixture may represent larger outcrops rising above low-lying regions filled with dust/sand. With a multi-instrument combined IR and VIS approach, it may be possible to quantify the presence of dust, sand, and lava outcrops on the surface to potentially extrapolate the spectral signature of lava outcrops.

The studies in this dissertation aim to: 1) identify pixels affected by significant shadowing at the time of the ASTER collection and calculate an areal percentage correction for those pixels, 2) better understand the relationship between mixed pixels, with subpixel particle

and block size variation, and ATI values, 3) develop a method to quantify the thermophysical variation between lava flows in an area considered too dusty for analysis and identify surfaces with significant portions of lava outcrops, and 4) model and quantify the areal percentages of dust, sand, and lava outcrops on the surface of lava flows. Through the use of multi-instrument and multispectral approach, the results of these studies will provide an improved understanding of the surface properties derived from TIR datasets.

## **2.0 A Quantitative Error Correction Approach for Shadowing in Apparent Thermal Inertia Data**

### **2.1 Introduction**

Studying the particle and block size distribution over a volcanic surface provides important information regarding recent events (such as recent ash fall or pyroclastic flows) and the stability of the surface for either vehicular access or structural collapse. For example, to insure the safety of group traversing a volcanic surface or rovers on other planetary bodies, it is essential to identify surfaces with a high concentration of finer particles or large boulders on which the vehicles are no longer maneuverable. Locating areas of weakness on steep slopes can also be used to determine the potential for flank collapse or landslides that can endanger local populations. Many of these areas are difficult or dangerous to reach and must be evaluated remotely for any hazard assessment to local populations.

One solution for this problem is the use of thermal infrared (TIR) datasets to remotely understand surface material characteristics (composition, particle size, and cementation). Thermal inertia (TI) is a derived product of TIR data and measures the resistance of a material to heating over the course of a day (diurnal cycle). The particle or block sizes on the surface can be estimated from TI due to the high dependence of thermal conductivity on the size of the object and thus the maximum temperature reached by and heating/cooling rates of the surface (Kahle et al., 1981). However, analysis of these datasets can be complicated by topographic variation, complex surface structures and/or instrument limitations. One such topographic complication, affecting the surface at the pixel and subpixel scale, occurs where shadows are cast on the

surface by large objects or steep slopes, lowering the maximum temperature reached by the surface during the day. These complications will lead to inaccurate characterizations of the surface and potentially inaccurate estimates in hazard models. Thus, it is important to be able to identify and assess this complication in TIR analysis to accurately derive the surface material properties. This study also has application for other surface property studies that are affected by shadowing.

With a compositionally homogenous surface, the North Coulee, part of the Mono-Inyo Crater system, is an ideal study site due to the steep sides and vast particle and block size distribution on the surface. These slopes are also large enough to cover an entire pixel in some areas, which is beneficial for the study to have an endmember to investigate the effect of a steep slope at the pixel scale. A multi-instrument and multispectral approach with different spatial and spectral resolutions is used to quantify the degree of shadowing on the surface. Higher spatial resolution visible data and DEMs can be used to understand the morphology of the coulee surface and the terrain variation that would cause shadowing throughout the diurnal cycle. With this understanding of the surface, the degree to which the TIR data is affected can be assessed.

The research proposed here aims to understand and constrain the effect of shadows from slopes and large boulders on thermally derived products. Without a better understanding of this effect, any derived surface properties will be inaccurate and the particle size will have a larger size estimate. This study seeks to: 1) establish a method by which significant shadowing can be identified that would affect ATI calculations, 2) quantify the degree of influence each shadowed area has on the resulting ATI value at the pixel and subpixel scales, and 3) provide a correction for the effect of shadowing to improve derivations of surface properties.



## **2.2 Background**

### **2.2.1 Geologic History of the Mono-Inyo Crater System**

Located on the eastern edge of the Sierra Nevada, the 11 km long chain of Mono-Inyo Craters formed from rhyolitic volcanic activity that began around 40 ka (Bailey, 1989; Bursik and Sieh, 1989). North of the Long Valley Caldera, this system rises roughly 610 m above the surrounding area, creating a prominent physiological feature. The Mono-Inyo crater system consists of the 11 km long Inyo Craters section and the Mono Craters just south of Mono Lake. Within the Inyo Craters section, roughly  $0.8 \text{ km}^3$  of rhyolitic-rhyodacitic magma erupted along a north-trending fracture during at least 3 eruption episodes localized at 6 magmatic and over 15 phreatic eruptive centers (Miller, 1985). In comparison, the Mono Craters section contains 28 domes and coulees that include explosion craters and ejecta rings (Bursik and Sieh, 1989, 2012). Hildreth (2004) estimated that the volcanic deposits in the Mono Craters amount to  $4 \text{ km}^3$  and Bursik and Sieh (1989) demonstrated that older eruptive events remain buried by recently formed domes. Analysis of age estimates and composition for both the Mono and Inyo crater sections suggest that this chain originates from a single magmatic system (Hildreth, 2004).

The Mono Craters are located within the Mono Basin that formed from regional warping and faulting causing subsidence in the area during frequent basaltic volcanism (Christensen et al., 1969). Hildreth (2004) emphasized the presence of 1-2 km of Pleistocene and Holocene lacustrine silts, non-welded Bishop Tuff from the 760 ka eruption of the Long Valley Caldera, and many thin ash layers within the basin. Using isotope studies to identify Argon ages in pre-Holocene rhyolitic ash layers in the lacustrine silts of the lake, roughly 15 explosive eruptions were identified dating before 20 ka (Chen et al., 1996; Kent et al., 2002). This basin is part of the

Long Valley volcanic region that has a complex tectonic setting between the Mina Deflection zone, the Eastern California Shear Zone, the Sierra Nevada microplate, and the Walker Lane fracture zone (Peacock et al., 2015). This volcanic region is located on the east-dipping faults on the western edge of the Basin and Range Province (Hill, 2006).

#### **2.2.1.1 Age Constraints on the Mono Craters**

This system is still considered to be potentially active and studies suggest that the Mono Craters erupted as recently as the 14th century (Miller, 1985; Hill, 2006). Studies have dated a majority of the rhyolite lavas in this system to the Holocene, with three dated to around 13 ka and a single around 20 ka (Wood, 1983; Bursik and Sieh, 1989). Evidence for this activity includes deposits of pyroclastic fallout, flows, and surges, as well as, lava domes and flows. The domes are covered with thick tephra deposits up to 200 meters in depth and ranging in grain size from ashy to blocky (Sieh and Bursik, 1986). Analysis of the correlation between age and texture characteristics demonstrates the dominance of moderately to lightly porphyritic textures in older extrusions from 35 to 3 ka and an aphyric texture in younger deposits (Wood, 1983). Further analysis of this shift in texture demonstrates a concurrent increase in the estimated volumetric eruption rate from  $0.2 \text{ km}^3/\text{ka}$  to  $0.8 \text{ km}^3/\text{ka}$  (Wood, 1983). This change in eruption characteristics provides critical information about what may have occurred at the source.

#### **2.2.1.2 Identifying the Source of the Mono Craters Section**

Comparison of the geographic orientation of the Mono Craters and the derived age constraints reveals the north-south alignment of these domes in the Mono-Inyo system (Hildreth, 2004). To explain this orientation, Bursik and Sieh (1989) proposed the presence of a regional extensional margin created by oblique-slip faults with NW-trends that produced a pull-apart

basin. Subsequent geophysical studies were completed in this area to identify the presence and extent of the eruption source. Seismic studies of the Mono craters suggest the presence of a north-south elongate magma chamber at roughly a depth of 10 to 20 km that fed dikes creating this system (Achauer et al., 1986). Recent three-dimensional modeling using magnetotelluric stations placed along the Mono Basin further support these conceptualized models by confirming the presence of two magmatic crystal-melt mush columns 10 km below the eastern edge of the Mono craters system and conductive east dipping dike swarms connecting the columns to the surface (Figure 1) (Peacock et al., 2015). These mush columns are the most likely source for the Holocene eruptions of the Mono Craters section.

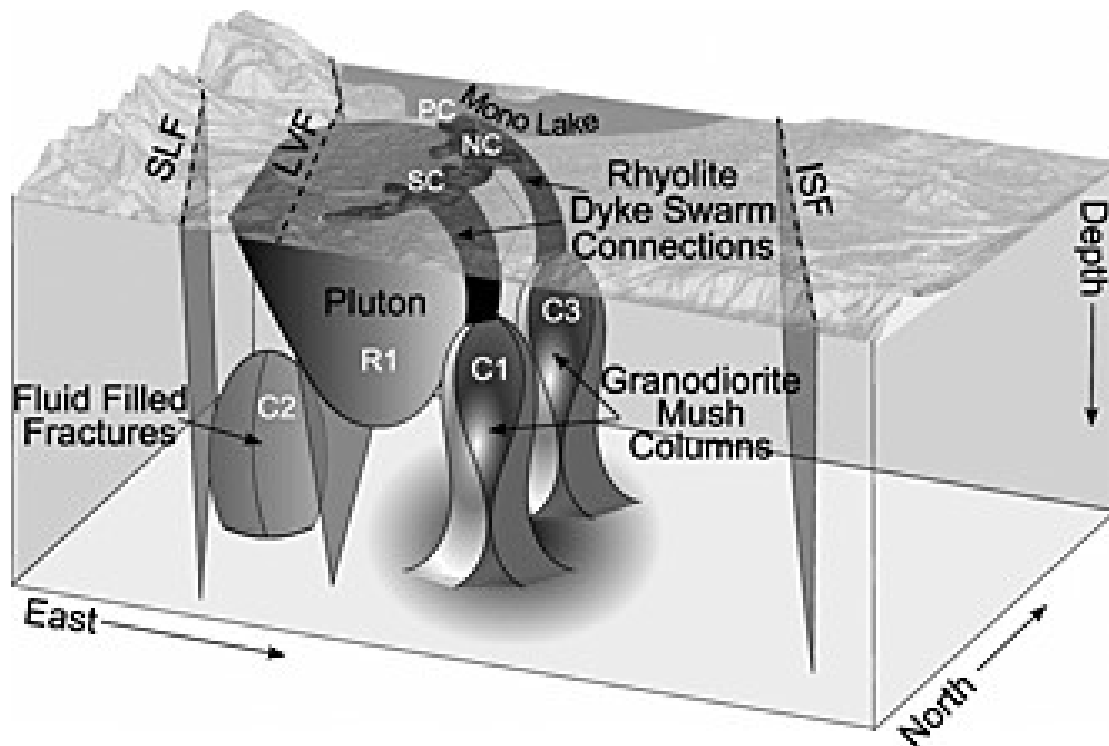


**Figure 1. Conceptual diagram created by Peacock et al. (2015) depicting the subsurface geologic model based on resistivity features. Arc-shaped dike swarms connected the granodioritic crystal-melt mush columns (C1 and C3) to the surface, producing the Holocene Mono Craters.**

### 2.2.2 North Coulee

The North Coulee was specifically selected for this study due to the range of tephra deposits, sporadic mantling, and semi-arid climate (Figure 2). This coulee, originating from a north-west oriented fissure, is the largest and most southern of the most recent aphyric rhyolite lava flows, making up the upper half of the Mono Craters, with a volume of  $0.4 \text{ km}^3$  (Russell, 1889; Seih and Bursik, 1986). Even though minor differences in trace elements exist, the deposits in the Mono-Inyo Crater area are considered to be homogenous in mineralogy and are composed of high-silica rhyolite with roughly 75.4-77 wt. %  $\text{SiO}_2$  (Bailey, 1989; Hildreth, 2004). However, analysis has shown that these minor differences in trace elements suggest that the deposits did not erupt from a single chamber (Kelleher and Cameron, 1990; Bailey, 1989). The mantling deposits have a comparable composition to the flows and originated from the surrounding vents in the last eruption phase the deposited airfall of pyroclastic material. The surface of the North Coulee contains a variety of block sizes and steep slopes along the edge that create shadowing throughout the day, providing the location necessary to study the effect of shadowing at the pixel and subpixel scales. Ultimately, these factors constrain the potential causes of any variation in thermal inertia to be the result of variations in particle or block size, presence of vegetation, or the effect of shadowing.

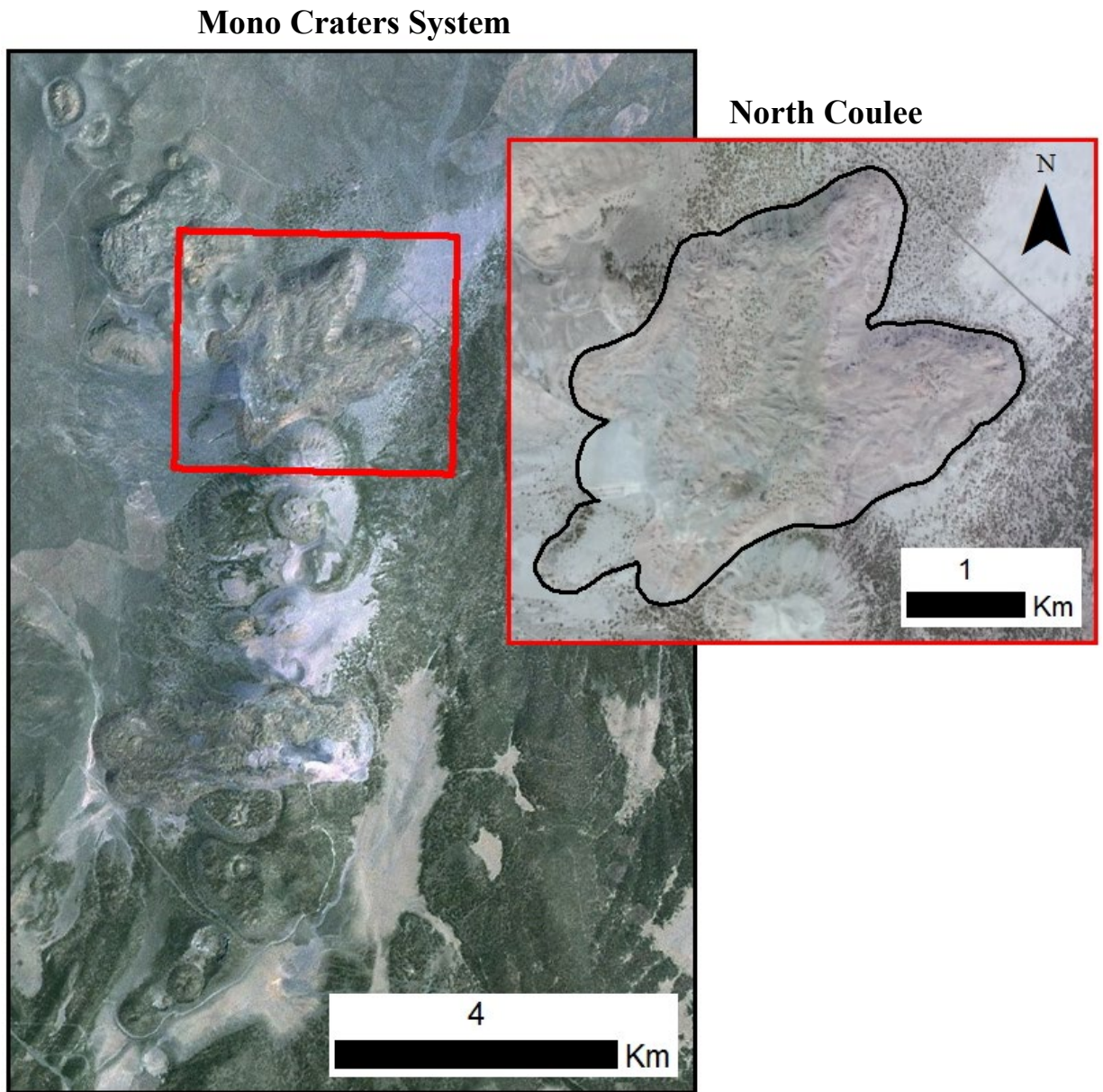


**Figure 2. Aerial image of Mono Craters System with the red rectangle showing the location of the North Coulee (WorldView-2 images courtesy of DigitalGlobe Foundation). North Coulee outline in black for study boundary context.**

### **2.2.3 Advanced Spaceborne Thermal Emission and Reflection Radiometer (ASTER)**

Advanced Spaceborne Thermal Emission and Reflection Radiometer (ASTER) data can be used to investigate the thermophysical and compositional properties of the surface. This instrument has three bands in the visible and near infrared (VNIR) ranging from 0.52 to 0.86  $\mu\text{m}$  with a 15 meter ground resolution, six bands in the shortwave infrared (SWIR) ranging from 1.60 to 2.43  $\mu\text{m}$  with a 30 meter ground resolution, and five bands in the thermal infrared (TIR) ranging from 8.125 to 11.65  $\mu\text{m}$  with 90 meter ground resolution (Yamaguchi et al., 1998; Table 1). The instrument has a repeat cycle of 16 days, providing the data necessary for temporal studies. Unfortunately, the SWIR data became saturated, and therefore unusable, in April 2008 due to a failure in the cryocooling system producing high temperatures in the detectors. The high spatial resolution, smaller pixel size, and wide spectral coverage of ASTER compared to previous instruments allow for a variety of surface materials to be distinguished and give a better understanding of compositional mixing (Yamaguchi et al., 1998). ASTER VNIR bands are predominantly used to investigate iron-oxide minerals and vegetation on the surface and TIR data is used to estimate silica content and thermophysical properties (Hellman and Ramsey, 2004; Rowan et al., 2006; Watanabe and Matsuo, 2003). Additionally, high spatial resolution digital elevation models (DEMs) are also produced from the VNIR bands. ASTER is an invaluable instrument to geologic studies due to the high spatial resolution, global coverage, and extended temporal coverage in the thermal infrared.

**Table 1. ASTER profile with spatial and spectral resolutions of each band (Yamaguchi et al., 1998).**

<b>Band Number</b>	<b>Spectral Range (<math>\mu\text{m}</math>)</b>	<b>Spectrum</b>	<b>Spatial Resolution</b>
1	0.52 – 0.60	VNIR	15 m
2	0.63 – 0.69		
3N and 3B	0.78 – 0.86		
4	1.600 – 1.700	SWIR	30 m
5	2.145 – 2.185		
6	2.185 – 2.225		
7	2.235 – 2.285		
8	2.295 – 2.365		
9	2.360 – 2.430	TIR	90 m
10	8.125 – 8.475		
11	8.475 – 8.825		
12	8.925 – 9.275		
13	10.25 – 10.95		
14	10.95 – 11.65		

#### 2.2.4 Thermal Inertia (TI) and Apparent Thermal Inertia (ATI)

Thermal inertia (TI) represents the resistance of a material to natural changes in temperature over the diurnal cycle and is used to estimate surface properties such as particle size, moisture content, and cementation (Pratt and Ellyett, 1979; Hardgrove et al., 2009). More specifically, TI is a measurement of the surface material's ability to store heat in the day and radiate it at night (Cracknell and Xue, 1996; Putzig and Mellon, 2007). It is calculated directly from the thermal conductivity ( $k$ ), density ( $\rho$ ), and thermal capacity ( $c$ ) of the material and is defined as  $I = \sqrt{k\rho c}$  with the units ( $\text{Jm}^{-2}\text{s}^{-1/2}\text{K}^{-1}$ ). Thermal conductivity ( $k$ ) measures the ability of a material to conduct heat or the rate heat passes through a specific thickness of a substance. Thermal capacity ( $c$ ) measures the amount of energy required to raise the temperature of a material by one degree. TI is primarily controlled by the thermal conductivity of the targeted surface, which in turn is the most dependent on the particle size and shape of the surface material (Presley and Christensen, 1997). Thus, specific relationships can be drawn between particle sizes and the resulting TI values. Large boulders have a higher TI value because the material takes longer to heat up during the day and cool down at night (higher thermal conductivity). The opposite response of quickly heating and cooling over the day causes smaller rocks or fine particles, such as sand or dust, to display low TI values (from lower thermal conductivity). Moisture content also has a significant impact on TI, with large bodies of water producing higher values.

The variables for TI cannot be determined remotely, so apparent thermal inertia (ATI) is utilized as an Earth-based approximation to extrapolate the grain size of surface materials (Hardgrove et al., 2009). ATI is the ratio of  $1 - \text{albedo}$  and the difference in diurnal temperature



$[ATI = (1 - \alpha)/\Delta T]$  with units of  $\text{K}^{-1}$  (Price, 1997). Albedo is amount of solar energy that is reflected by a surface, so  $1 - \alpha$  is the portion of radiation that is absorbed by the surface materials. Thus, ATI can be described as the measure of the amount of absorbed radiation energy divided by the temperature range over the day. In order to accurately capture the diurnal temperature variation, the day and night temperature data must be collected at specific times correlating with the maximum and minimum temperatures of a day to capture the maximum contrast. Numerous studies have utilized the unique qualities of ATI to investigate the soil moisture content and geologic identification in many different regions of Earth by modeling surface energy budgets (Matusima et al., 2018, Scheidt et al., 2009).

Though the potential applications for remote ATI studies are boundless, atmospheric, vegetation, and climate complications on the Earth can hinder the interpretation of ATI values. Earth's thick, heterogeneous atmosphere absorbs and scatters energy affecting the transfer of radiant energy on the surface between grains and creating a complicated path of radiant energy (Price, 1977). Kahle (1977) unified the radiative heat transfer model and the latent and sensible heat transfer between the atmosphere and ground. This model was developed to produce a remote sensing tool with applications for geology and soil moisture determination that would take into account the complicated atmosphere. Sabol et al. (2006) addressed any change in weather or atmospheric conditions by attempting to shorten the period of collection time necessary to capture the maximum variation in surface temperature. This study explored the technique of capturing the rate of temperature change ( $dT/dt$ ) by measuring the temperature at short time intervals to calculate ATI values. By using this method, the chance of clouds, rainfall, or wind developing during data acquisition would reduce significantly. However, this requires a short repeat collection time for an instrument, a parameter that may not be possible for a satellite.

The current method for orbital data requires the collection of local climate information to determine the potential complications from precipitation and atmospheric humidity, which can significantly hinder TI studies (Matsushima et al., 2012). Heavy vegetation may also complicate geologic ATI studies as it will mask the underlying surface. Studies have attempted to separate the signature of vegetation and local geology in areas with low to moderate vegetation coverage with a maximum cover of 25% the total area (Maltese et al., 2012; Zhang et al., 2016). With access to higher spatial and spectral resolution data, additional complication can be addressed that have been avoided.

### **2.2.5 Shadowing Effects**

A significant complication to the derivation of surface properties from ATI data occurs where pixels are covered in shadows for a significant portion of the day, particularly the time of data acquisition. Shadows happen when direct solar radiation is completely or partially occluded from a surface (Figure 3) and can result from topographic slopes, such as the steep sides of the North Coulee, or rough terrain with larger shadows cast by boulders or clouds. Shadowing is a significant problem in all remote sensing datasets that hinders information extraction and alters the response received by the sensor. In regards to VIS datasets, the calculated reflectance of the shadowed surface will be reduced compared to a surface with the same material properties without shadows because a significantly less solar radiation is interacting with the surface. This effect will have a significant impact on TIR datasets because the amount of energy emitted by a material depends on the amount of solar radiation absorbed. Shadows will cause materials to have lower albedo and daytime temperature (the solar radiation is blocked by the object casting the shadow), both of which are used to calculate ATI.

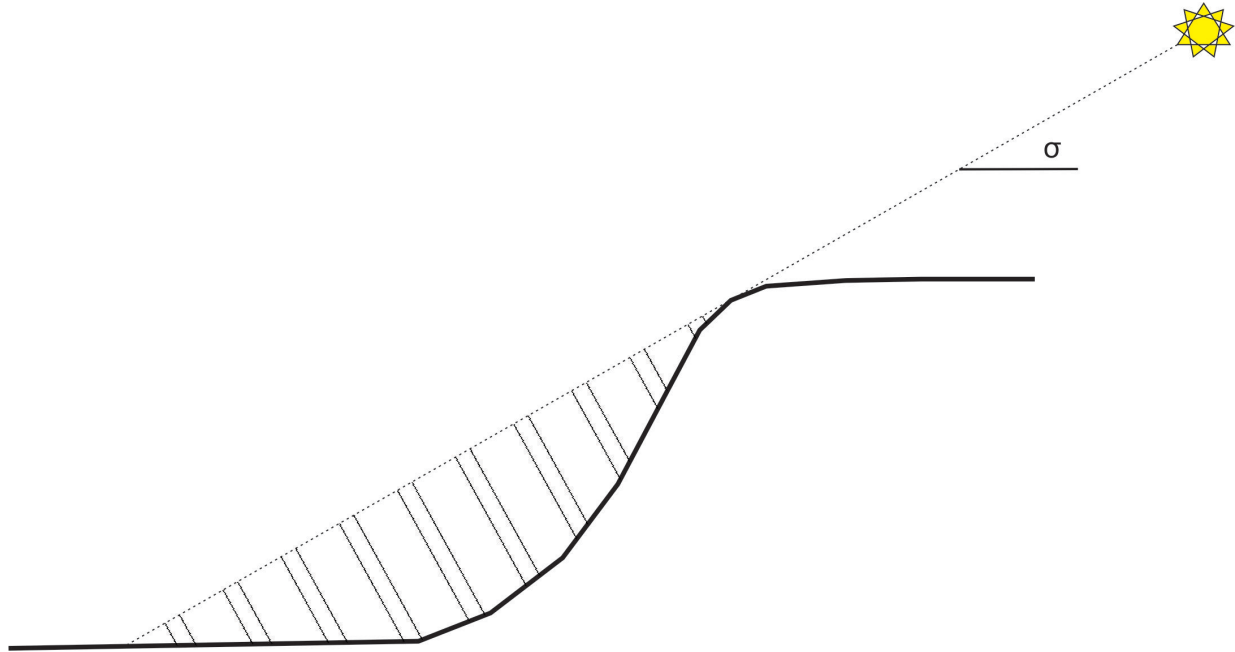


**Figure 3. Illustration of the shadows created by topographic slopes such as those along the edge of the North Coulee. The length of the shadow is dependant on the solar elevation angle ( $\sigma$ ).**

Previous studies have focused on identifying the locations of shadowing affecting remote sensing data. Giles (2001) compared and evaluated the accuracy of identifying shadowing in multiple images using a delineation algorithm and human interpretation. The algorithm only correctly identified roughly 86% of the shadows, most likely due to the high dependency on the Digital Elevation Model (DEM) accuracy compared to the actual landscape. However, the human interpretation approach also contained potential errors, specifically in areas along the edge of shadowing zones which require expertise to identify (Giles, 2001). Some studies have even attempted to develop a correction to remove the effect of shadows. Richter (1998) formulated a radiometric correction to remove both topographic effects using DEMs and Lambertian models. However, these corrections require atmospheric parameters that are not always available or easy to collect and the results are difficult to assess. A recent study by Tolt et

al. (2011) utilized LIDAR data to create a Digital Surface Model (DSM) that was used to train a supervised classifier on hyperspectral data. This method sufficiently identified shadowed and non-shadowed areas, but was subject to uncertainties. These studies demonstrate that the most important factor in determining a proper correction for shadows in the collection of the highest spatial resolution DEM.

## **2.3 Methods**

Multiple spatial and spectral resolution orbital datasets were used to identify and correct for the effect of topographic shadowing (Table 2). ATI derived from ASTER TIR and VIS data was derived to investigate the thermophysical and compositional properties of the study area. A few assumptions must be discussed in order to fully understand the use of the ASTER data. Even though clouds can also cause shadows, this does not apply to this study and is thus not included in any further analysis. Furthermore, the arid environment present during the summer at the Mono Craters make issues with soil moisture, such as humidity and dew, minimal to insignificant for this study. Rainfall records from Sonora Junction and Bridgeport Ranger Station, the two closest weather stations, demonstrate a lack of precipitation 10 days prior to the collection days. Additionally, the average high daytime temperature in the area during May was 299.93 K and 280.32 K overnight.

In order to understand the topographic variation on the surface, the DEM used is a mosaic of the best-quality elevation data from a variety of sources (USGS, 2013 & 2018). A DEM is a 3-dimensional representation of a surface terrain with coordinates  $x$ ,  $y$ , and  $z$  ( $x$  and  $y$  are the surface coordinates and  $z$  is the vertical extent). These elevation models are created from

successive overlapping aerial photos and the offset between these images is used as an estimate for the vertical dimension, elevation. The National Elevation Dataset (NED) is an elevation model assembled by the U.S. Geological Survey collected at 1/3 arc-second or 10 meters as part of an initiative to make a global DEM map with the highest spatial resolution available. Global DEMs have also been generated from ASTER data, but the resolution is only 1 arc-second or ~30 m which is significantly less than the NED product and thus are not used in this study. To understand the location of shadows on the surface of the North Coulee, two higher level products were derived from the DEM, slope and hillshade.

**Table 2. List of datasets and derived products used to identify and correct shadowing errors (Yamaguchi et al., 1998; USGS, 2013 & 2018).**

Instrument	Spatial Resolution	Spectral Range	Application
Advanced Spaceborne Thermal Emission and Reflection Radiometer (ASTER)	15 m	VNIR	To understand the visible and thermophysical properties of the surface
	90 m	TIR	
Derived Products			
Surface Temperature	90 m	TIR	For derivation of ATI values and understanding the thermophysical properties
Albedo	15 m	VNIR	For derivation of ATI values and understanding the surface properties
Apparent Thermal Inertia	90 m	Albedo and Temperature	To understand the thermophysical variation
Instrument	Spatial Resolution	Application	
Digital Elevation Model (DEM)	1/3 arc-second 10 m	To understand the topographic variation on the surface	
Derived Products			
Slope	10 m	To quantify the change in elevation between pixels	
Hillshade	10 m	To quantify shadowing that is present at a particular time	

### 2.3.1 Calculating Apparent Thermal Inertia

The main purpose of this study is to understand the effect of shadowing on derived ATI values. ASTER level 2 temperature (AST\_08), level 2 VNIR surface reflectance (AST\_07XT), and level 2 TIR surface radiance (AST\_09T) datasets were used to calculate ATI values (Figure 4). Both atmospheric scattering and emission corrections were already applied to the level 2 ASTER data. To confirm the accuracy of the level 2 temperature data, a version of the Plank equation was solved for temperature, assuming an emissivity of 0.96 based on previous work on emissivity normalization techniques (Ramsey and Fink, 1996), and applied to ASTER TIR radiance data products (L1B). With the confirmation of accuracy, level 2 temperature data were used to calculate the difference in daytime and nighttime temperatures.

Fundamentally cloud-free and chronologically similar ASTER data products were collected on May 31<sup>st</sup>, 2014 at 18:51:43 UTC (11:51:43 local time) and June 1<sup>st</sup>, 2014 at 5:55:29 UTC (May 31<sup>st</sup> 22:55:29 local time; Table 3). It is important that the images are collected on dates as close as possible and on cloud free days to avoid any changes in weather or surface parameters to accurately detect the surface material. High humidity and precipitation will change the diurnal temperature values and decrease the range of the results. This collection technique also captures the same seasonal diurnal response. To be more specific, the diurnal curve of a specific material will vary by season because of the difference in the amount of solar radiation interacting with the surface depending on the tilt of the Earth, which produces the seasonal temperature variation. The maximum temperature reached by a surface will generally be higher during the summer season than in the winter. The ASTER image pairs were collected within 24 hours of each other, so any variation in the surface is negligible and the true diurnal cycle during that season is captured.

Another important aspect of this method is to validate that the data is geographically aligned to the highest degree possible to allow for the accurate calculation of ATI. This is to make sure that the same surface area is covered by a pixel in each of the three datasets. Even though these datasets have been previously georeferenced by the instrument team, slight variations may exist between different collections. To correct for this potential issue, ground control points (GCPs) were used to apply an image to image warp to guarantee that the same area is sampled by a specific pixel in each dataset. Additionally, both images were cropped to the same extent for both mathematical processes. Once the images were geographically aligned and cropped, pixel values in the nighttime temperature and daytime temperature images were applied to calculate the  $\Delta T$  values. The resulting temperature difference, which makes up the denominator the ATI equation, highlights the change in surface temperature over a day for each pixel. To calculate albedo, all three bands of the AST\_07XT Visible and Near Infrared (VNIR) surface reflectance data were averaged for each pixel. It is important to note that the inclusion of SWIR data would have been optimal, but the data have been unavailable since 2008 due to complications with the ASTER instrumentation. However, since the study area is considered compositionally homogenous with mainly rhyolite, the reflectance values in the SWIR would behave similarly and therefore the albedo would have changed uniformly across the domes (Mars and Rowan, 2010). Thus, the errors caused by the absence of SWIR data are minimized at this site. The resulting averaged albedo image was applied to the numerator of the ATI equation  $(1-\alpha)$  to determine the amount of solar radiation absorbed by the surface. In the final step of this calculation, the  $(1-\alpha)$  and  $(\Delta T)$  values were applied to the ATI equation  $(1-\alpha/\Delta T)$  to understand the difference in surface material characteristics present on the surface of the North Coulee (Figure 5).



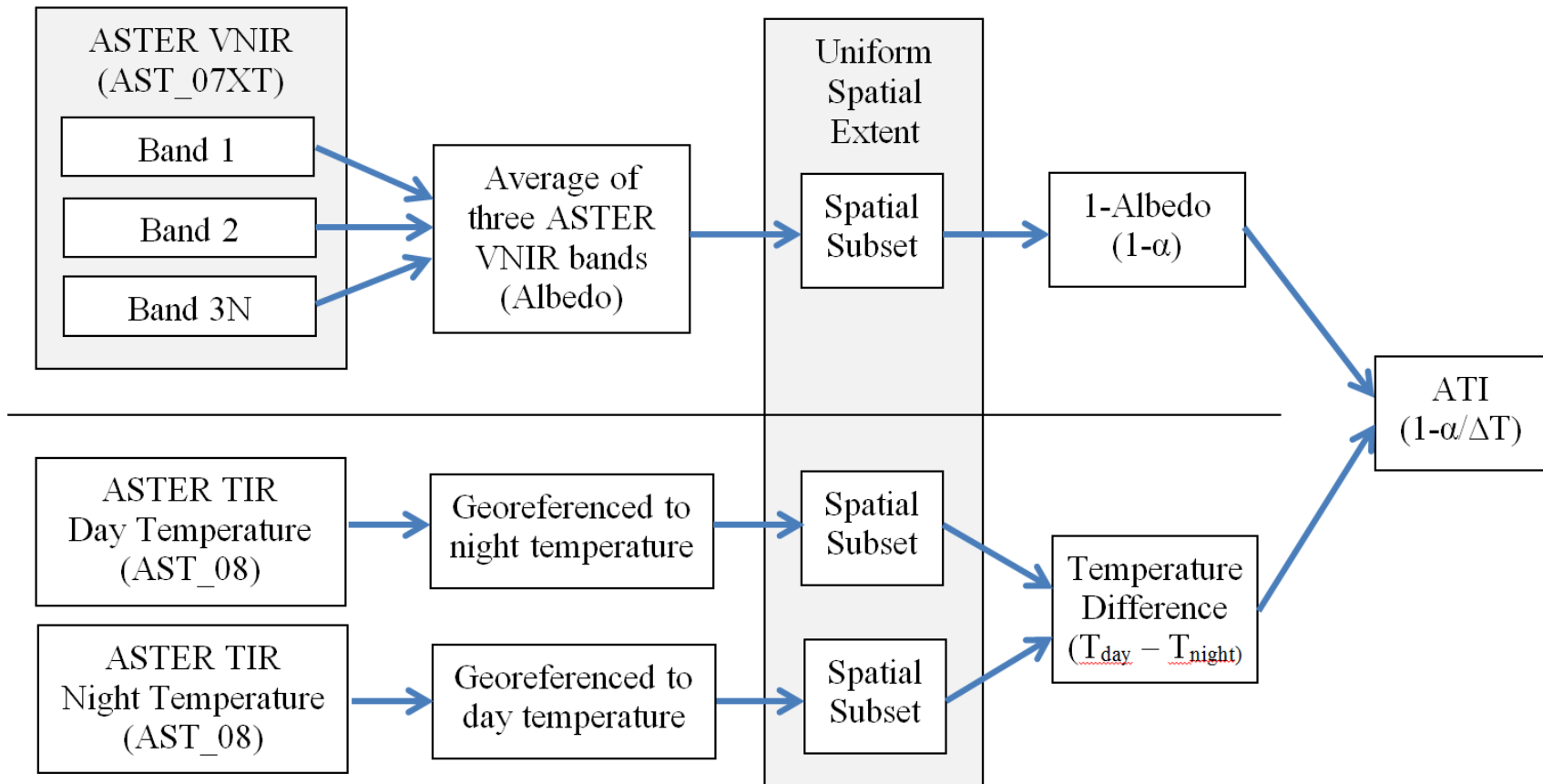
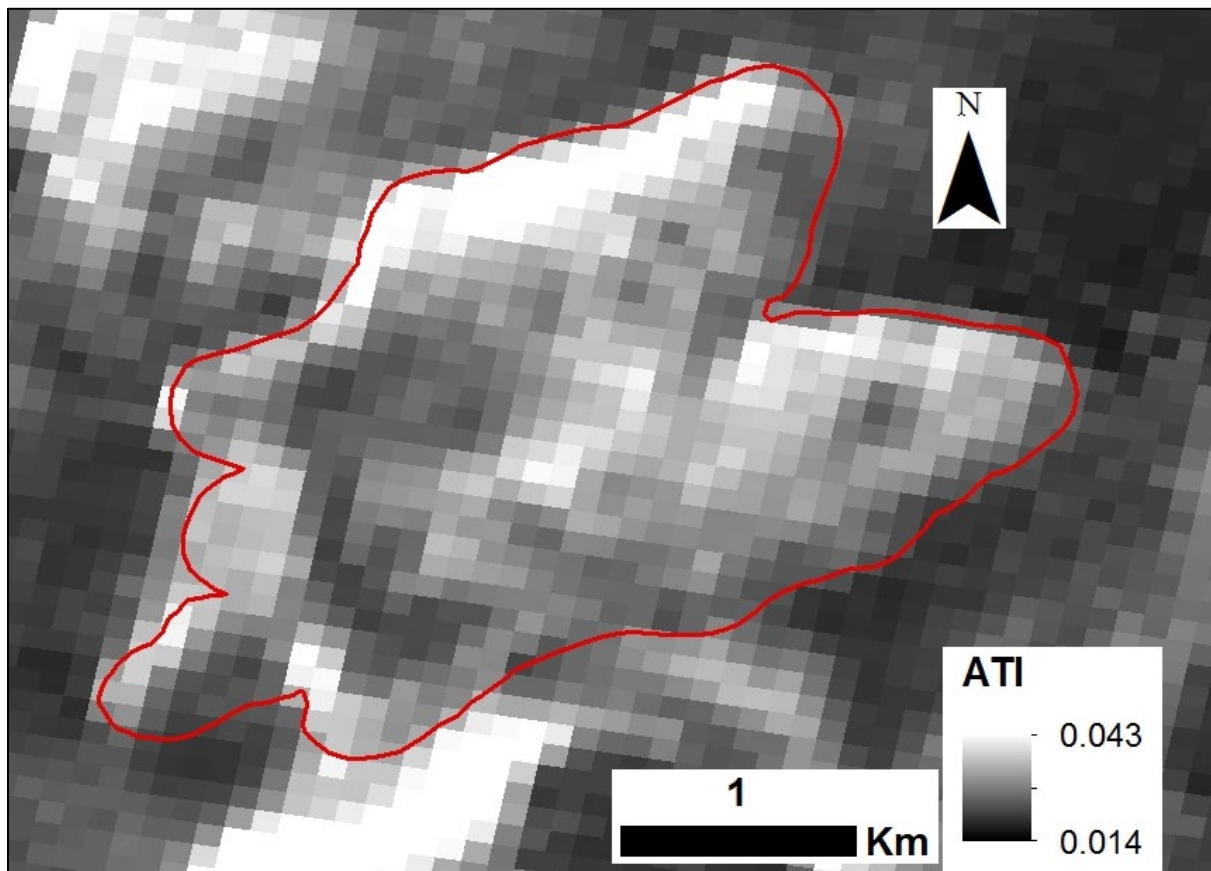


Figure 4. Workflow for calculating apparent thermal inertia (ATI) values from ASTER VNIR and TIR datasets.

**Table 3. ASTER dataset used to calculate ATI.**

Acquisition	Product Name	Day/Night	Scene ID
31-May-2014	Surface Reflectance	Day	AST_07XT_00305312014185143
31-May-2014	Surface Kinetic Temperature	Day	AST_08_00305312014185143
1-June-2014		Night	AST_08_00306012014055529



**Figure 5. ATI calculated from ASTER TIR and VNIR data with red outline of the North Coulee (Yamaguchi et al., 1998). North facing slopes display unusually high ATI value.**

### **2.3.2 Products Derived from Digital Terrain Models: Slope and Hillshade**

To understand the topographic variation on the surface of the North Coulee, two additional products were derived from the DEM data: slope and hillshade topographic models. The slope data represents the maximum change in elevation over a defined distance measured between a point and the neighboring pixels (range of 0 to 90 degrees; Figure 6A). The point of this model is to identify a minimum slope at which shadowing occurs at this particular date and time to better understand large scale effects at the pixel scale. Hillshade is a 3D model that takes into account the sun's position in relation to the study surface to display any cast shadows at a specified time of the day, representing the degree to which solar radiation is occluded from the surface. Solar azimuth and solar elevation are used to define the relative position of the sun when the ASTER images were captured and the DEM was the topographic base unit to define the elevation and slope. Solar azimuth is defined by the position of the sun on the horizon in relation to geographic north (measured clockwise from north ranging from 0 to 360) and the solar elevation is the angle above the horizon (ranging from 0 to 90 degrees). For this study, a solar azimuth of  $135.63^{\circ}$  and solar elevation of  $69.23^{\circ}$  were applied to the shaded relief calculations to produce values that represented the amount of shadowing over the coulee at the ASTER daytime collection time (Figure 6B). To understand how the shadowed areas change throughout the day, the solar azimuth and solar elevation were changed to simulate a full diurnal cycle (Appendix A). Each pixel in the hillshade is assigned a number from 0-500 with 0 being completely shaded from the sun.

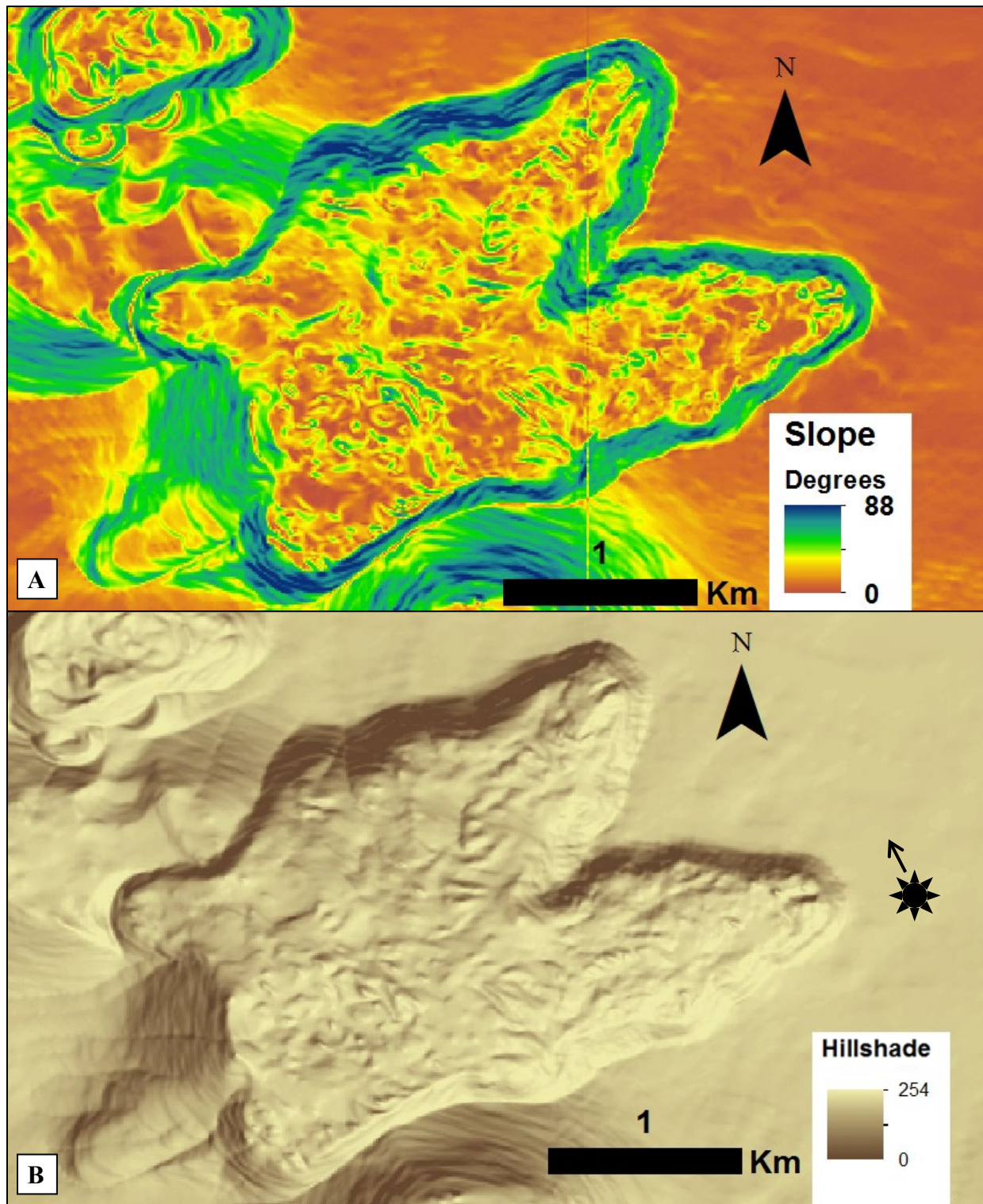


Figure 6. (A) Slope data demonstrating the variation in surface slope on the North Coulee. The steepest slopes are located along the coulee edge and the top displays significant variation. (B) Hillshade image displaying the degree to which an area is affected by shadows with a depiction of the sun direction for context.

### **2.3.3 Identifying Areas Affected by Shadowing Errors**

The derived hillshade data provides the best basis for identifying areas significantly affected by shadows during the ASTER collection time. To establish the basic response for the surface (with the fewest shadows present), an additional hillshade was calculated with a solar elevation of 90° to depict the sun's position straight overhead. These two hillshade models were compared to identify values significantly different in the actual collection parameters by taking the ratio of the 90°/actual solar elevation. Flat and not occluded surfaces were analyzed to establish a minimum value above which shadows are likely to be present; these areas display a value close to 1. Further statistical analysis of areas suspected to have significant shadowing (north-facing slopes) demonstrates that a threshold value of 1.25 in this ratio data represents the minimum value at which significant shadows are present. The pixels identified in the ratio image were transposed on the original hillshade data to define the corresponding maximum threshold value of 175, below which represents shadowed areas (Figure 7).



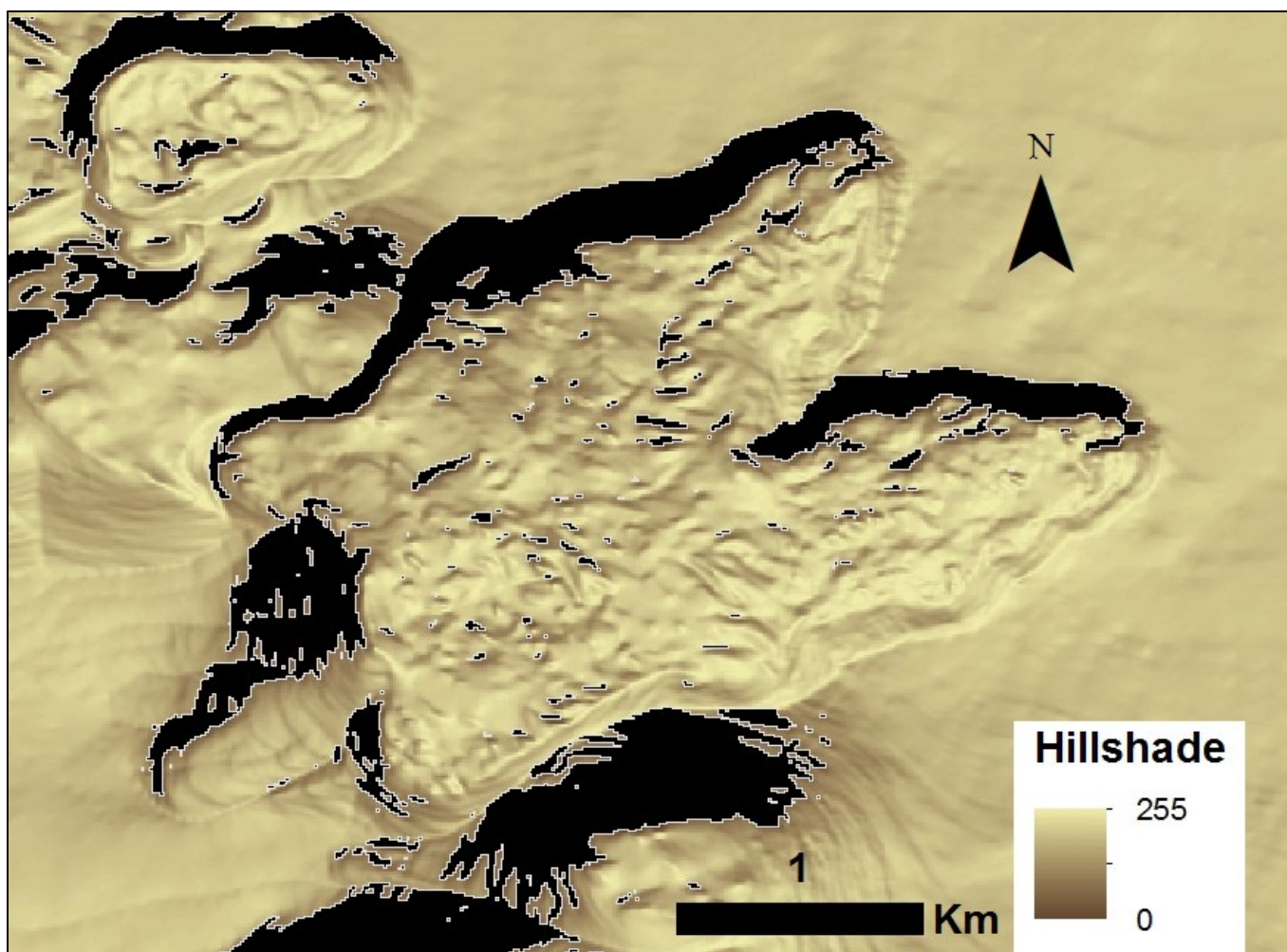


Figure 7. ROIs (black regions) defined by values less than 175 in the hillshade data are used to identify areas with significant shadowing.

Regions of interest (ROIs) were used continuously throughout this shadowing project to identify and correct the shadowing errors. Based on the hillshade ratio analysis, a band threshold ROI was applied to highlight all pixels with a value less than 175 (corresponding with values over 1.25 in the ratio of  $90^\circ$  to actual solar elevation) (Figure 7). To determine which pixels in the TIR and VNIR data included these identified shadowed areas, the ROIs produced from the hillshade calculation were applied to both the daytime temperature and albedo data. This analysis produced a distinct set of ROIs identifying the affected areas at the pixel scale, including pixels that were either fully or partially covered by the hillshade ROIs, for each dataset (Figure 8 and Figure 9). Through this process, the pixels in the temperature and albedo data affected by shadowing at the time of collection were identified.

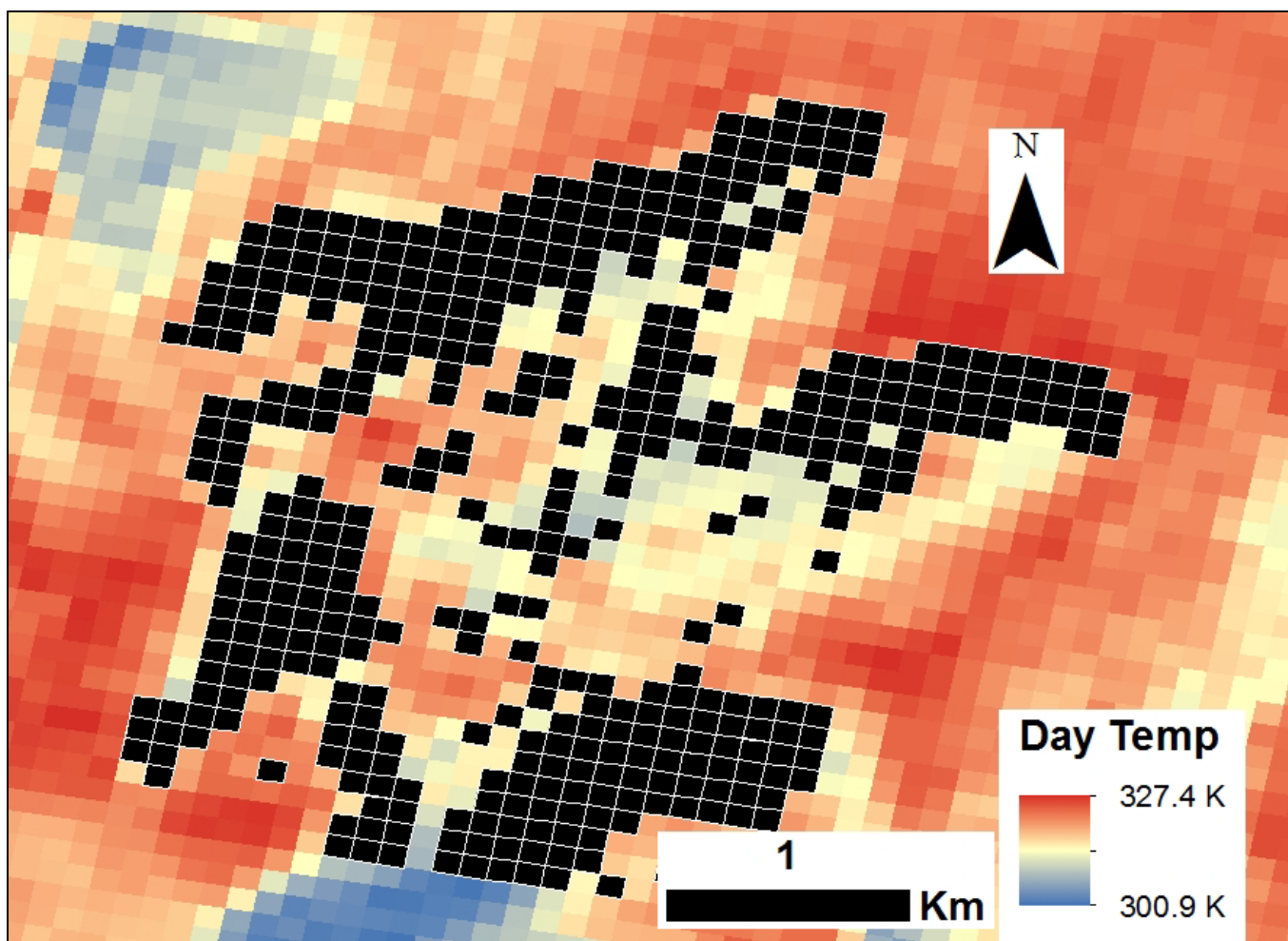


Figure 8. ROIs of pixels significantly affected by shadowing at the spatial resolution of the ASTER TIR temperature data (Yamaguchi et al., 1998). The correction applied to each of the identified pixels is based on the areal percentage of the hillshade ROIs multiplied by the maximum identified correction.



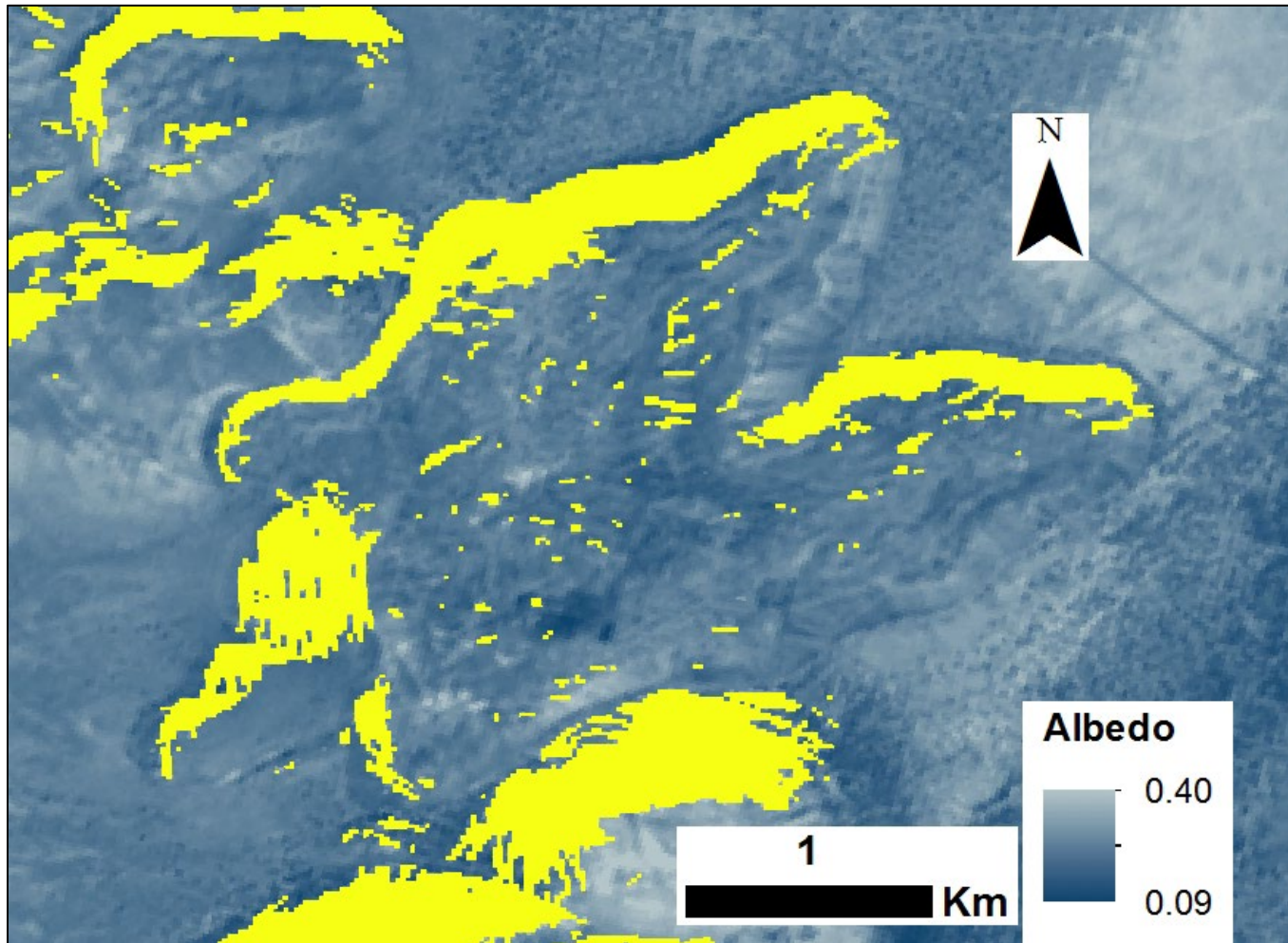


Figure 9. ROIs of pixels significantly affected by shadowing at the spatial resolution of ASTER VNIR data (Yamaguchi et al., 1998). The correction applied to each of the identified pixels is based on the areal percentage of the hillshade ROIs multiplied by the maximum identified correction.

### **2.3.4 Calculating Correction for Shadowing Errors**

Initial investigations to identify potential corrections to TIR and VNIR pixels affected by shadowing focused on the sloped sides of the North Coulee because aerial photographs and images taken in the field demonstrate the structural and morphological similarity between the slopes, confirming that these slopes should display very similar TIR and ATI values (Figure 10). These slopes are dominated with large boulders lodged at the top, smaller rocks, pebbles, and trees in the middle, and moderate sized rocks at the base. Due to this similarity in composition and structure, south facing slopes were used as an endmember base for what values all of the slopes should display. Statistics were calculated, similar to those run to identify the maximum hillshade value, for both the daytime temperature and albedo data on slopes unaltered by shadows (south facing and some east facing) and shadowed north facing slopes. These calculations for the south facing slopes were averaged in order to determine accurate minimum, maximum, and mean values that should be displayed by the sloped areas. These statistics for both daytime temperature and albedo were analyzed and the following factors were determined to be potential maximum adjustments for incorrect pixels; daytime temperature pixels were increased by a maximum value of 5 K and albedo pixels were increased by a maximum value of 0.03. However, not all of the identified temperature and albedo pixels were completely covered by the hillshade ROIs used to identify pixels containing shadows. To address this complication, percentage adjustments for each pixel were calculated for daytime and albedo datasets to produce the most accurate corrections.



**Figure 10. Photograph taken in the field depicting the typical slope material along the sides of the North Coulee including trees, boulders, finer particles and moderate rocks.**

Initial attempts to correct the data involved applying a standard uniform correction to the daytime and albedo datasets (5 K increase to temperature and 0.03 increase to albedo). However, statistical analysis of the harsh contrast between corrected areas and the original data demonstrated that this simple correction was not adequate. Analysis of the daytime temperature and albedo images suggested that the best quantitative correction applies an adjusted correction based on the percentage of each pixel covered by the hillshade ROIs used to define areas significantly covered by shadows. This approach would take into account that not every pixel was completely covered in shadows.

The areal percentages of the hillshade ROIs within each affected ASTER TIR (90 m) or VNIR (15 m) pixel were calculated to identify the degree to which shadowing was present.

Additionally, a pixel-by-pixel analysis was performed comparing each of the highlighted pixels with its nearest neighbors to make sure that it was not falsely included. This analysis produced an extensive look-up table (LUT) with each pixel and the percentage of the pixel area covered by shadows (Figure 8 and Figure 9). To calculate the adjusted correction for each pixel, the proposed maximum correction value (5 K or 0.03) was multiplied by the areal percentage covered by shadow for each pixel. After the completion of these analyses, new daytime temperature and albedo files were produced with the adjusted pixels. To calculate the resulting ATI values, the albedo dataset was spatially resampled to match the pixel size of the ASTER TIR daytime and nighttime temperature data. This is done by averaging the 36 VNIR albedo pixels that cover the same extent as a single TIR temperature pixel so that both datasets have the same spatial resolution. With the correction of the daytime temperatures and albedo values, ATI was completed by applying the three datasets to the equation  $ATI_{sc} = (1 - \alpha_{sc}/\Delta T_{sc})$ . Through this adjusted correction method, the resulting  $ATI_{sc}$  data has thus been corrected for topographic shadowing complications both at the pixel and subpixel scales.

## 2.4 Results

### 2.4.1 Identification of Shadowed Pixels

Pixels with significant shadowing were identified using the DEM, slope, and hillshade datasets, the latter of which proved to be the most useful to identify these features on the surface of the North Coulee. The main areas (at the pixel scale) defined as affected by shadowing for the collection time of the daytime TIR and VNIR data were located on north-facing sloped sides of



the coulee and minor shadowing (on the sub-pixel scale) were identified on the top of the coulee. It is important to note that these identified areas are unique for a specific collection time and date because the direction and length of cast shadows are dependent on the location of the sun. In order to apply the identification technique to other collection datasets, slope and hillshade derived products would have to be calculated with the solar azimuth and elevation for the new date and time. Assessing the correlation between the shadowed pixel locations and the slope model demonstrates that areas with higher slope percentages (greater than  $36^\circ$ ) are significantly more likely to be affected by shadowing at particular times of the day depending on the solar azimuth and solar elevation.

Another important aspect of the study is the validation of orbital and airborne datasets to investigate the surface of hazardous or hard to reach areas that impact local populations. This identification technique demonstrates that the 10 meter (1/3 arc-second) USGS DEM is a sufficient spatial resolution to identify shadowing at both the pixel and subpixel scale of the ASTER TIR data. This study demonstrates the use of a multi-instrument approach with different spatial resolutions has applications for identifying shadows not currently addressed in lower spatial resolution data.

#### **2.4.2 Single Value Correction vs. Adjusted Correction**

Initial application of a single value correction to pixels identified as significantly affected by shadows by the hillshade ROIs demonstrate the faults in this simplistic approach and that the pixels are not equally nor uniformly influenced by the shadows on the surface. The most obvious visual representation of this can be seen along the boundaries between corrected and original pixels that display an unrealistic transition with a sharp jump in value. Even though some pixels

covering the middle of the north-facing slopes display a comparable value to the southern slopes, these disjointed boundaries demonstrate that pixels on the edge of the correction zone are not uniformly covered by shadows. Further investigation of the pixels at the ASTER TIR 90 m spatial resolution show that even along the longest slopes only two or three ASTER pixels cover the area and edge pixels include areas completely exposed to solar radiation (no shadowing). Only roughly 23% of the pixels identified as affected by shadows are completely covered. Thus, the best method of correction should take into account that a majority of the pixels are only partially covered by shadows.

### **2.4.3 Evaluation of Surface Temperature and Albedo Corrections**

The areal percentage method does not change the pixels identified for correction, the value applied to each pixel is based on the areal percentage of the surface that is covered by shadows. This correction applied to the daytime temperature data significantly improves the value of the affected pixels compared to non-affected pixels (Figure 11). Without the correction, the north facing slopes displayed an average value of 305 K and the south facing 320 K (a difference of 15 K). Reviewing ROI analysis across north and south facing slopes, pixels covering north facing slopes now display comparable values (with north facing slopes occasionally showing up to 3 K below expected) and more closely resemble those on unaffected slopes with similar composition and morphology. Albedo values adjusted to counteract the influence of shadows also produced a notably improved image (Figure 12). Pre-correction albedo values average 0.16 for north facing and  $>0.21$  for south facing slopes. Similar to the response identified in the temperature correction data, identified pixels now display similar values to unaffected slopes with north facing slopes at 0.2. However, due to the 15 meter spatial resolution

of the VNIR datasets, the transition between corrected and uncorrected zones is not as seamless compared to the daytime temperature data. This suggests that there is potentially a slightly better correction for the identified pixels in the albedo data. However, because this dataset is spatially resampled to the 90 m resolution of the TIR data, the effects of this variation are minimized and negligible for further analysis.

Quantitative error analysis focused on the north and south facing slopes because these areas were identified as having similar composition and structure, including particle and rock size distributions, from fieldwork. Multiple ROIs on these two slope types were statistically analyzed to identify the average value range that should be displayed by these slope surfaces. This statistical assessment demonstrated that the day temperature values had a range 3 K lower on particular sections of the coulee and the albedo values had a range 0.02 less on sections. Minor variation or potential errors occur predominantly on the correction zone edge or small areas on the flow surface, potentially due to incorrect identification by the hillshade ROIs.

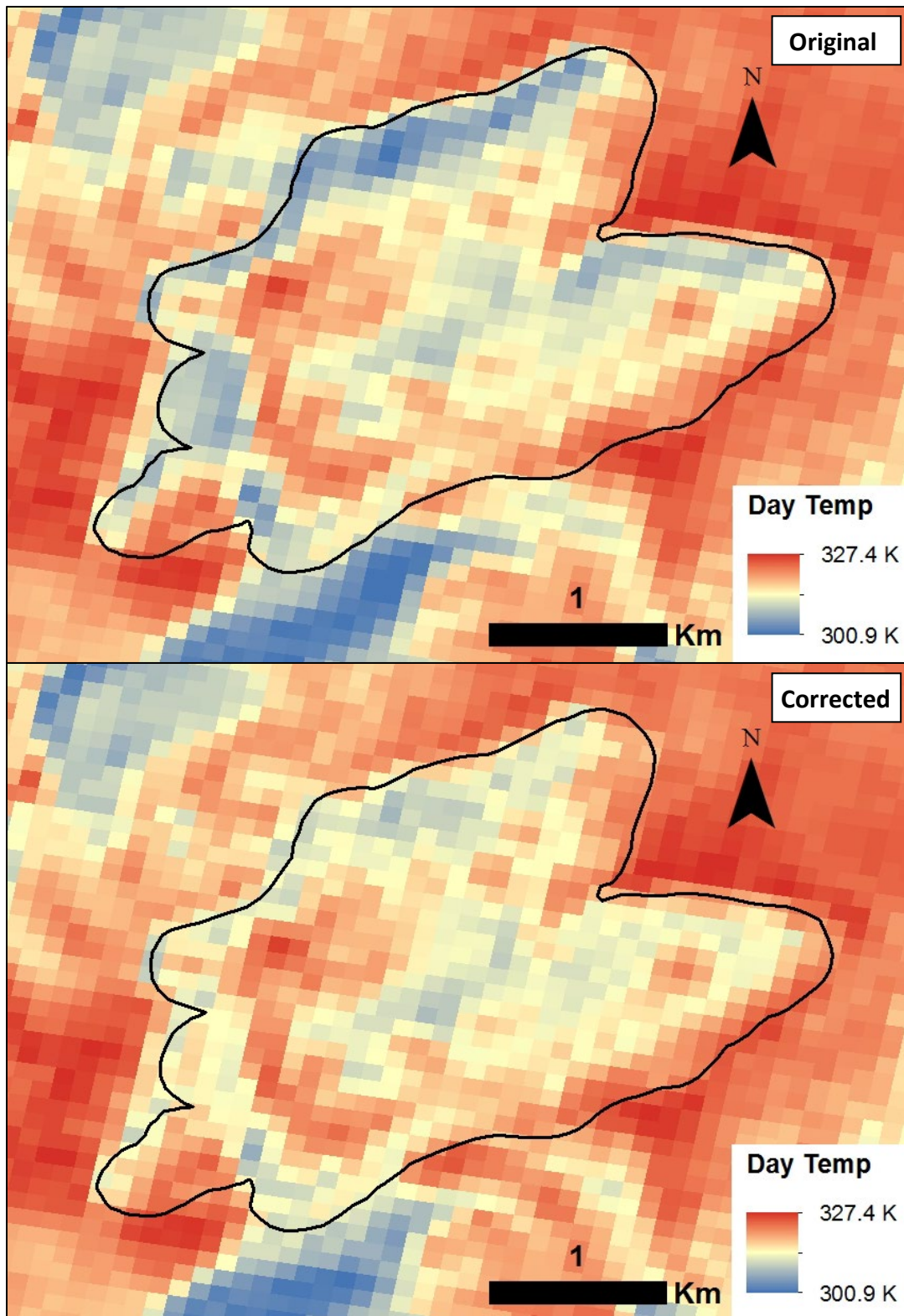


Figure 11. Comparison of the original and corrected daytime temperature data with black outline of the North Coulee demonstrating significant improvement to affected pixels in the corrected data.



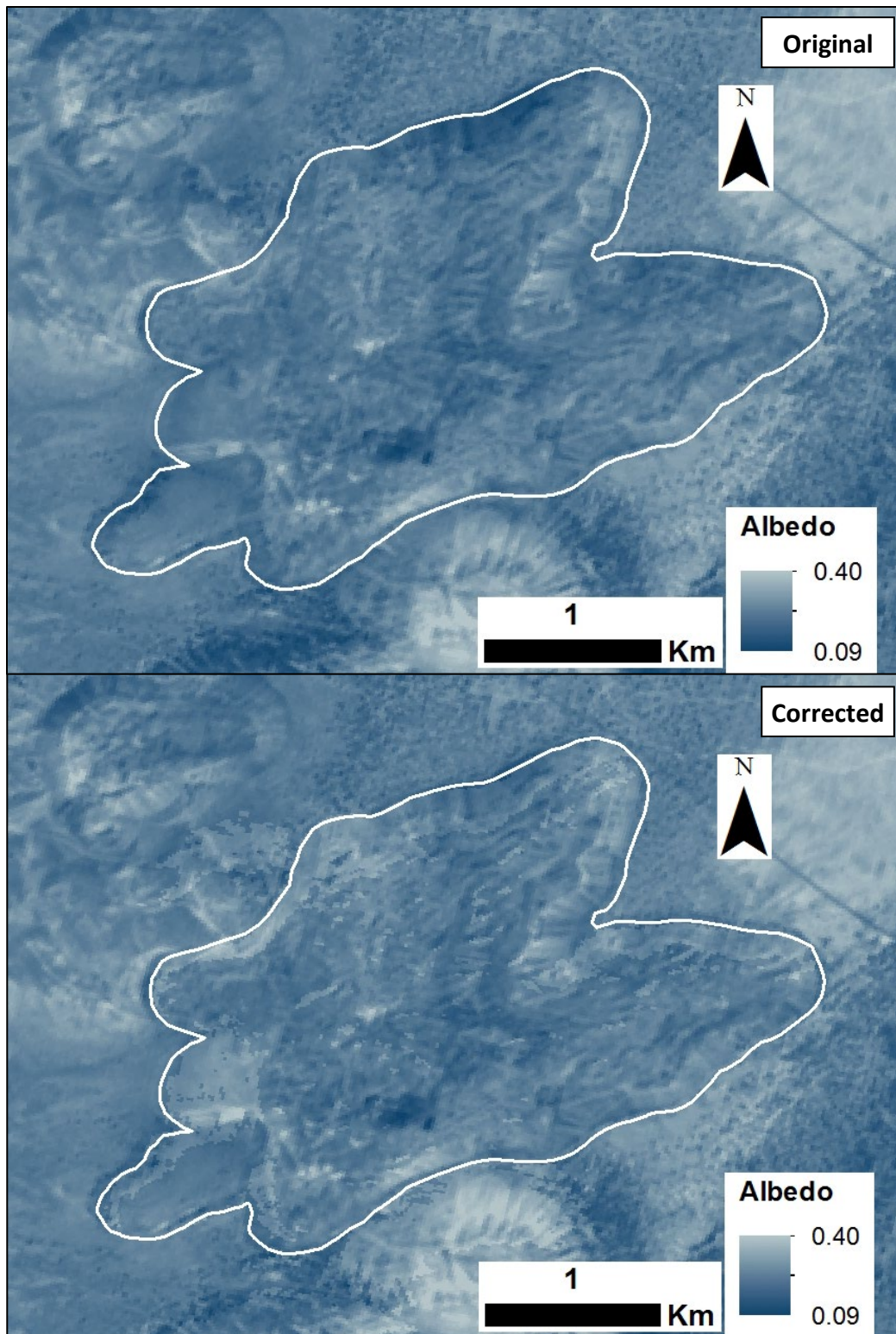


Figure 12. Comparison of the original and corrected albedo data with white outline of the North Coulee demonstrating significant improvement to affected pixels in the corrected data.

#### 2.4.4 ATI Correction Evaluation

Prior to any attempted corrections to the ASTER data for the effect of shadows, obvious locations can be seen where the presence of shadowing affected the calculated value. Of particular focus was the north facing slopes that were the most influenced by shadowing cast by greater than  $36^\circ$  slopes. These slopes displayed the greatest error values when compared to the similar south facing slopes ( $>0.031$  on north slopes vs  $\sim 0.02$  on the south slopes with a difference  $>0.011$ ). New  $ATI_{sc}$  values computed using the corrected daytime temperature and albedo images, produced from the areal percentage method, are significantly improved compared to the originals ( $\sim 0.003$  difference between the average slope values; Figure 13). Northern slopes previously displaying signifying high ATI values (indicative of large rocks) now display similar values to pixels on slopes not influenced by shadowing (more indicative of smaller particle sizes). Comparison of multiple ROIs on both north and south facing slopes demonstrates that these corrections to both day temperature and albedo pixels affected by shadowing are sufficient enough to allow for scientific analysis of the entire flow rather than avoiding significantly shadowed areas.

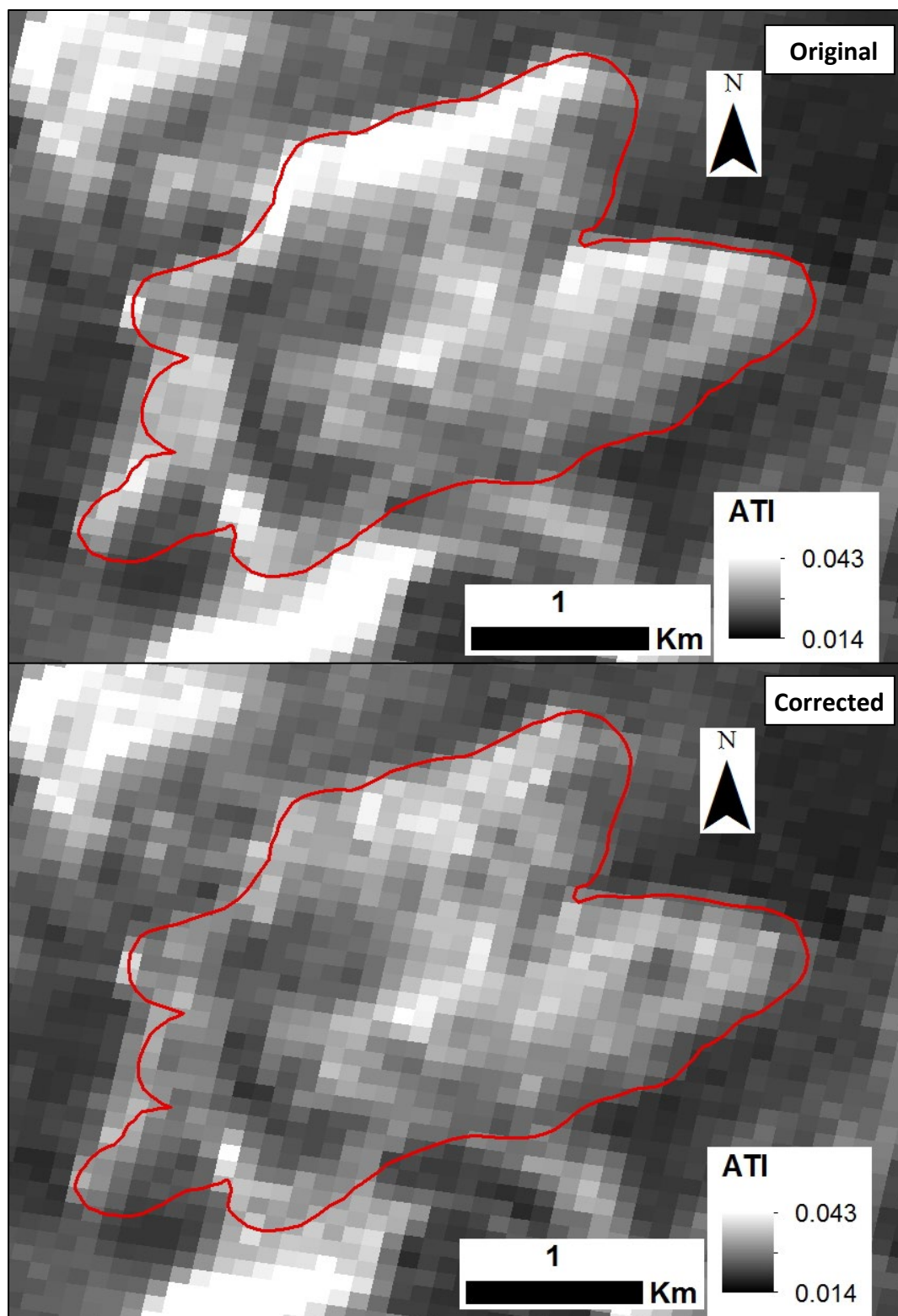


Figure 13. Comparison of the original and corrected ATI data with a red outline showing the extent of the North Coulee. The results demonstrate significant improvement to affected pixels in the corrected data.

## 2.5 Conclusion

The purpose of this study was to accurately identify and quantitatively correct for the effect of shadows of the surface of the North Coulee in the Mono-Inyo craters system. The great diversity in surface deposit sizes ranging from ashy to blocky along with the steep slopes exceeding  $40^\circ$  make this site an ideal location to study the effects of shadowing on ATI values. By producing derived products of slope and hillshade from an NED DEM, a method was identified to determine which areas were significantly affected by shadowing during the collection time of the ASTER data. The precision of this identification is only limited by the spatial resolution of the DEM dataset (10 meters for this study). This study demonstrates that satellite and/or airborne surface elevation datasets have sufficient resolution to identify not only the large at ASTER pixel scale shadowed north facing slopes, but also smaller subpixel shadowing created by comparatively smaller variations on the surface.

Areas on the surface and sides of the North Coulee affected by shadowing at the time of data acquisition for the ASTER daytime data were identified using hillshade models derived from a NED DEM. This was accomplished by calculating the ratio of two hillshade models, one with a  $90^\circ$  solar elevation (sun is overhead) and the other using the actual solar elevation at the time of data collection, to highlighting the deviation from a baseline model of the area. Areas with significantly lower hillshade values compared to the  $90^\circ$  model were easily identified as those affected by shadowing. ROIs were created from the hillshade data and applied to the ASTER TIR and VNIR datasets to determine which pixels were affected by shadowing. With the successful identification of the shadowed pixels on the surface of the North Coulee, this study proceeded to determine a quantitative correction for these pixels. Comparison of the temperature and albedo responses on the north and south facing slopes led to the identification of a maximum

correction of 5 K and 0.03, respectively. Initial attempts to apply these values demonstrated that a simple uniform correction of a single value was not accurate, so a more gradational or adjusted approach was defined because not all pixels were completely covered by shadows. This correction takes into account the areal percentage of a pixel surface that is covered by shadow (defined using the hillshade data) by modifying the correction value based on the percentage.

Application of the areal percentage method significantly improved the affected pixels in the day temperature and albedo datasets as seen in the comparison of transects from the north and south facing slopes. Minor differences can still be seen between the overall statistical trends of the affected and non-affected slopes ranging up to 2 K for the day temperature and 0.02 for the albedo datasets. The error analysis suggests that slight improvements may be possible for this method, but the overall accuracy demonstrates the usefulness of this process to investigate areas previously ignored due to the effects of shadowing. Furthermore, this areal percentage method for identification and correction can be easily applied to ATI values at other locations with restricted vegetation growth.

## **2.6 Acknowledgements**

This research was supported through continuing funding of an original Mars Odyssey Participating Scientist Program project (grant number: NMO710630) and a NASA Earth and Space Science Fellowship (award number: 80NSSC17K0460). ASTER data used in this study are available at Earthdata Search application: <https://search.earthdata.nasa.gov/>.

### **3.0 Assessing Subpixel Surface Roughness and Block Size Distribution to Improve Thermal Inertia Interpretations**

#### **3.1 Introduction**

Bedrocks of lava flows and other volcanic terrains provide information about past volcanic and eolian processes. For example, compositional or vesicularity differences suggest the presence of changing magma conditions and deposition properties, which may, in turn, provide critical information about the evolution of the magma chamber. However, deposition, erosion, and transportation of finer-grained materials can cover or obscure any accurate investigation of these surfaces. The source of these fine materials may have local origin, but it may be difficult to determine, especially for remote or hazardous areas, and thus it cannot usually be assumed to have the same properties as the bedrock. The first step to investigate these bedrocks is to accurately identify the different particle and block sizes present to ultimately determine the location of exposed bedrock. Without this estimation, any compositional or vesicularity analysis may be interpreting the finer-particle material.

Thermal infrared (TIR) remote sensing data are invaluable to the investigation of many inaccessible or hazardous areas such as volcanic features. This type of technique allows for a detailed analysis of the surface thermophysical properties including particle size, composition, and/or vesicularity. However, complex mixed surfaces complicate the accurate derivation of these values because current methods assume uniform material properties at the spatial resolution of the instrument. Thus, a singular value will be assigned or calculated for the entirety of a pixel (i.e. a single particle size), which does not represent a mixed surface materials present (mixed

pixel problem). This complication can be particularly seen, and studied, in areas with homogenous mineralogy where it is apparent that the relationship between specific particle sizes, especially complex surfaces, and thermal inertia values is not well understood. For example, the detection of coarse particles may be obscured by a cover of fines (vertical layering) or a mixture of rock sizes may be misinterpreted as a single unit (with horizontal or checkerboard mixing). Thus, it is critical to improve the identification of different horizontal mixtures of particle sizes on the surface and the presence of vertical layering.

With access to higher spatial and spectral resolution datasets, the use of multiple instrument datasets can provide improved detail about the surface properties and materials. In this study, a multi-instrument approach using both thermal infrared and visible datasets improves the understanding of subpixel mixing and thermal inertia, which will in turn provide unique information about the flow emplacement for older and active flows and domes. Visible near infrared (VNIR) datasets provide a higher spatial resolution of the surface, even allowing for surface property interpretation without detailed field studies. Thermal data from the Advanced Spaceborne Thermal Emission and Reflectance Radiometer (ASTER) is used for comparison with a visible identification to improve the derivation of surface properties with pixels that contain horizontal mixtures of multiple types. This study builds on previous work to understand and quantify the effect of mantled material on underlying igneous rocks. Price et al. (2016) demonstrated that particle size differences could be seen in apparent thermal inertia (ATI) datasets covering the Mono Inyo Crater chain North Coulee by establishing the presence of general endmembers (fine particle size and boulders). This same study site, selected for the homogenous composition and varying particle sizes, is the location of this continued work to improve the relationship between derived ATI values and subpixel particle size variation.

The research improves the understanding of the relationship between ATI values and the subpixel variation on the surface. This work seeks to: 1) determine a method to identify the surface particle or block size distributions on the surface using orbital datasets by identifying distinct surface types, 2) quantitatively define the areal percentages of different particle or block sizes surface types present on the surface within ATI pixels at a lower spatial resolution, and 3) understand any constraints on the particle size variations that will produce the same ATI values.

## **3.2 Background**

### **3.2.1 Geologic Setting of the North Coulee**

The Mono-Inyo Craters system in California contains rhyolite flows that formed around 40,000 years ago and is located on the east-dipping faults on the western edge of the Basin and Range Province (Bailey et al., 1976; Bursik and Sieh, 1989; Hill, 2006). Seismic and magnetotelluric studies of the area suggest that these dome and coulees formed from dikes fed by a north-south elongate magma chamber at ~10 to 20 km depth (Achauer et al., 1986; Peacock et al., 2015). These 28 Mono domes and coulees possess tephra deposits from younger eruptions with thicknesses ranging from non-mantled to heavily mantled with >10 cm depth (Sieh and Bursik, 1986). The particle sizes present on the surface of the North Coulee flow, the location of this study, ranges from ashy to blocky, so the TIR pixels covering this coulee will capture the expanse of spatial mixing and mantling depths. The homogenous rhyolitic mineralogy, with ~75.4-77 wt. % SiO<sub>2</sub>, on the coulee allows for a detailed investigation of the relationship between thermal inertia values and different particle or block size mixtures within a pixel



(Bailey, 1989; Hildreth, 2004). Furthermore, this area maintains a semi-arid climate which constrains the potential complication of climate on the remote sensing data, especially TIR datasets. The surface of the North Coulee represents a range of different surface types that contain particle or block sizes with predominantly uniform endmembers (containing a single particle size) to the presence of vertically layering or horizontally mixing, which represents a majority (Figure 14). To assess the subpixel distribution of particle and block sizes, multispectral data from orbital sensors with spatial resolutions ranging from 1.85 to 90 m/pixel were analyzed, along with samples, GPS, and photogrammetry data acquired during a mapping campaign.



**Figure 14. Field photography illustrating the range of grain sizes present on the surface of the North Coulee, specifically at ‘the bowl’ study area.**

### 3.2.2 WorldView-2

High spatial resolution data collected by WorldView-2, launched by DigitalGlobe, is ideal for a wide range of remote sensing studies. This is the first commercial imaging instrument with the ability to collect data in 8 spectral bands at such a high spatial resolution. With 46 cm resolution panchromatic and 1.85 m resolution multispectral datasets, in-depth image analysis of the study area is possible. However, WorldView-2 data is resampled to 0.5 m (panchromatic) and 2.0 m (multispectral) for standard products. The panchromatic band covers a wavelength range of 0.450-0.800  $\mu\text{m}$  and the 8 multispectral bands located in the VNIR are coastal (0.400-0.450  $\mu\text{m}$ ), blue (0.450-0.510  $\mu\text{m}$ ), green (0.510-0.580  $\mu\text{m}$ ), yellow (0.585-0.625  $\mu\text{m}$ ), red (0.630-0.690  $\mu\text{m}$ ), red edge (0.705-0.745  $\mu\text{m}$ ), Near-IR1 (0.770-0.895  $\mu\text{m}$ ), and Near-IR2 (0.860-1.040  $\mu\text{m}$ ) (DigitalGlobe, 2013). Each of these bands were specifically placed for feature classification, vegetation studies, and bathymetric measurements. The repeat cycle for this instrument is 1.1 days which is ideal for assessing and mapping land cover change over a short period of time. However, since this is a commercial instrument, this is the only dataset used in this study that is not freely accessible to the public and may be a hindrance to exact reproducibility. The WorldView-2 images used in this project were part of an imagery grant courtesy of the DigitalGlobe Foundation.

Numerous vegetation studies have used this data to study the health of specific vegetation types, map the location of particular tree species, and assess biomass (Ozdemir and Karnieli, 2011; Immitzer et al., 2012; Eckert, 2012). While vegetation studies are an obvious use for this dataset given the locations of the bands, WorldView-2 data is useful for many other study types of urban and surface material. Novack et al. (2011) utilized the 8-bands in WorldView-2 to classify different urban materials ranging from ceramic tile roofs to bare soil. This study

demonstrated that this dataset was able to more accurately identify different urban material types compared with QuickBird-2. This dataset has also been used to generate stereo-extracted digital surface models (DSM) (Aguilar et al., 2013). Hobí and Ginzler (2012) demonstrate that the forested areas are the most difficult type of surface to accurately model in DSM even at the high spatial resolution of WorldView-2 data. These studies demonstrate that this dataset has multiple applications ranging from vegetation to topographic studies.

### 3.2.3 Apparent Thermal Inertia and Particle Size

The resistance of a material to heating and cooling over the course of a day can be measured using thermal inertia (TI),  $I = \sqrt{k\rho c}$  with units ( $\text{Jm}^{-2}\text{s}^{-1/2}\text{K}^{-1}$ ), which is calculated directly from the (k) thermal conductivity, ( $\rho$ ) density, and (c) thermal capacity of the material. However, these material properties k,  $\rho$ , and C cannot be derived remotely using orbital datasets. ATI,  $ATI = (1 - \alpha)/\Delta T$ , is utilized as an Earth-based approximation with units of  $\text{tiu}$  (Price, 1997). The components of TI are inferred by measuring the temperature variation during a diurnal period and collecting knowledge of the surface properties during the cycle (Kahle et al., 1976).

The calculation of ATI from VNIR and TIR datasets allows for the investigation of the surface material properties. TI is primarily controlled by the thermal conductivity of the targeted surface, which measures the ability of a material to conduct heat or the rate heat passes through a specific thickness of a substance. Presley and Christensen (1997) demonstrated thermal conductivity is most dependent on particle size and shape of the surface material. Cracknell and Xue (1996) also proposed a linear relationship between changes in particle size, soil density, and soil moisture with TI. Thus, specific relationships between TI values and particle size can be

determined, allowing for an estimation based on the calculated ATI (Hardgrove et al., 2009). For example, smaller particle sizes heat up and cool off quickly over the course of the day, producing a low TI, and larger particle sizes take longer to heat and cool, producing a higher TI value.

### **3.2.4 Sub-pixel Particle Size Mixtures**

The minimum spatial unit of an image is the pixel and the current assumption is that the material properties within a pixel are uniform (i.e. contain homogenous properties). This proposes that an image is covered with pure pixels or those that contain a single material component (Choodarathnakara et al., 2012). Using the current assumption, the derived properties of a pixel, assuming uniformity, will be assigned a single soil moisture estimate, particle size, and/or composition. For some rare areas this assumption may be valid, but this is not likely to be applicable for most complex surfaces. Pixels are more likely to contain a mixed surface of two or more material types, thus the value will be a combination or average of the separate components present. The distribution of pure and mixed pixels within an image is a factor of the spatial resolution of the instrument and of the complexity of the surface morphology. One way to better understand the relationship between mixed pixels and ATI values is to study an area that is predominately affected by a single material property difference (i.e. an area with homogenous composition with varying particle size distributions).

Laboratory studies of thermal conductivity (a component of thermal inertia) have attempted to better understand the effect of different particle sizes within a defined area on TI. Presley and Craddock (2006) compared the thermal conductivity-derived particle size of a sample with the actual size distribution present. The initial studies looked at an area with a range of smaller particle sizes (less than or equal to 125  $\mu\text{m}$ ) and determined that the thermal

conductivity of these samples reflects the larger particles in the sample. For this range of particle sizes, the thermal conductivity will represent the maximum particle size present and any derivation of surface properties from data over this type of surface will assume the sole presence of this maximum size. Conducting similar measurements with the addition of large particle sizes, it was demonstrated that the thermal conductivity of these samples with a large amount of smaller particles sizes, less than or equal to 125  $\mu\text{m}$ , display a lower value than the corresponding value of a larger particle sizes in the sample. Thus, the signatures of these samples are influenced most by significant amounts of the small particle sized material. The complexity of this relationship between thermal conductivity and particle size requires further study.

With continued advances in instrument development with increasingly higher spatial resolution, the accuracy of this assumption has been severely questioned (Choodarathuakara et al., 2012; Gupta et al., 2011; Foschi, 1994). At higher spatial resolution the image may contain more pure pixels, but the presence of mixed pixels is increasingly obvious. Furthermore, in-situ field measurements demonstrate the variation of material properties present within a single pixel, invalidating the uniform assumption. Thus, a technique must be developed to understand the relationship between thermal inertia and different subpixel combinations of particle and rock sizes on the surface.

### **3.2.5 Photogrammetry**

Accurate assessment of topographic features is a critical aspect of geologic research, particularly investigations of changing surface structures. This is limited by the spatial resolution of the dataset and one approach to understanding fine scale topography is the use of photogrammetry techniques. Photogrammetry is the science of calculating particular surface

measurements from at least two photographs (in 2D), the outputs of which can be as simple as defining a distance between two features or as complex as producing terrain maps, drawings or 3D models. Some of the main benefits of photogrammetry techniques are the ability to create high spatial resolution digital terrain models (DTM) or digital elevation models (DEM) without extensive ground surveys and capture advantageous perspectives not attainable on the ground. These surface models allow for more detailed investigation of the surface material and any current alteration processes.

The U. S. Geological Survey (USGS) pioneered the field of photogrammetric methodology with multiple advancements including the panoramic camera, panoramic photoalidade, tri-lens camera, and many more innovations (Thompson, 1958). Digital photography has long been used as a tool for geologist to study the surface and extract topographic information, especially from stereo photography (Birdseye, 1940). With the stereoscopic technique, unique three-dimensional coordinates are estimated from two or more images taken from different viewing angles (Bemis et al., 2014). With the rapid development of technology, this technique can now be applied to large collections of overlapping images to produce a detailed 3D representation of the surface with millions of surface points (Lane et al., 2000; Lowe, 2004; Snavely et al., 2006). Furthermore, the development of laser scanning, both airborne and terrestrial, and soft-copy photogrammetry have greatly improved the spatial extent and resolution of DEMs (Hodge et al., 2009; Notebaert et al., 2009; Lane et al., 2000). Structure from Motion (SfM) expands on the principles of stereo-photogrammetry to include a series of overlapping, offset images collected by a moving sensor around a feature of interest to capture optimal camera positioning (Figure 15; Westoby et al., 2012). The SfM feature-matching algorithms are the most successful with a high degree of overlap between images from a wide

array of positions. For example, this technique has been applied to photographs collected from the internet of historic sites to determine the accuracy of reconstructing buildings from publically available data (Snavely et al., 2007). Even though the final product is limited by a lack of geographic coordinates, this process succeeded in producing a detailed 3D reconstruction of the historic areas.

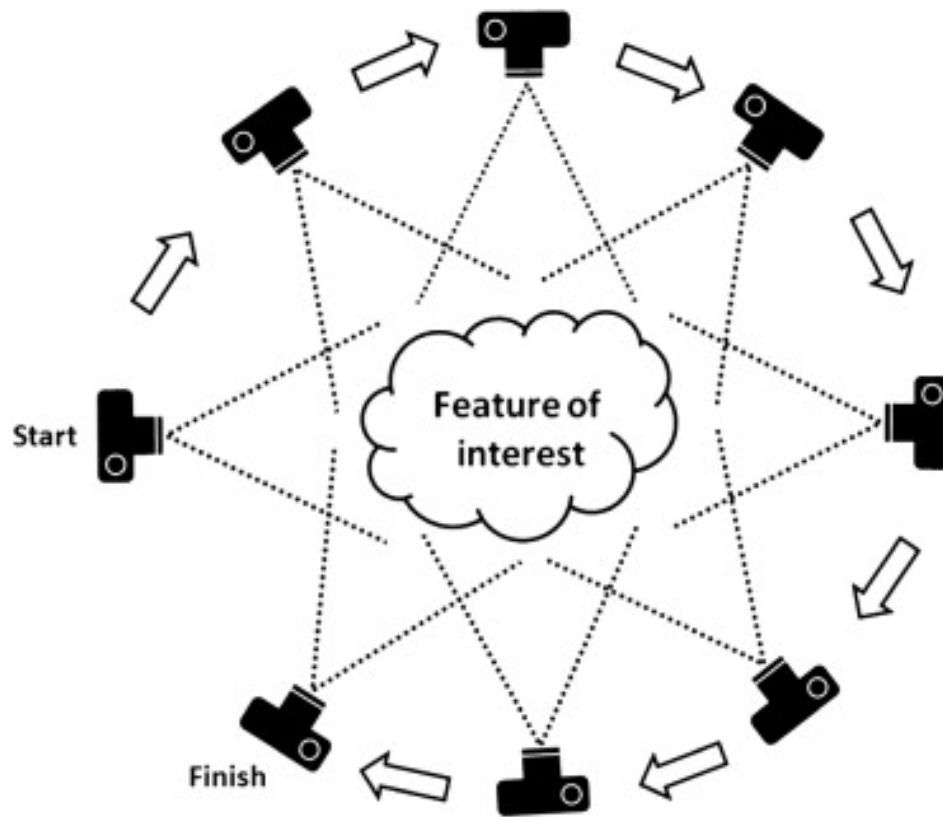


**Figure 15.** Description of the process used in Structure from Motion (SfM) in which multiple, overlapping photographs are used to produce a 3D construction of the surface (Westoby et al., 2012).

### **3.2.5.1 Areal and Terrestrial Techniques**

There are two main forms of data collection for photogrammetry techniques: aerial and terrestrial (or close-range). Aerial photogrammetry is collected by mounting a camera to an aircraft or an unmanned aerial vehicle (UAV) and collecting multiple overlapping photos along a flightpath. One main benefit of areal photogrammetry using balloons, kites, and UAVs is the improved overhead viewing angles that provide unique camera positioning not possible on the ground (Smith et al., 2009; Niethammer et al., 2012; Lorenz and Scheidt, 2014). This technique provides improved line of sight, particularly on surfaces with complex morphologies, and the ability to more remotely acquire data over a large surface area. UAVs or airborne photogrammetry can remotely map areas that are too hazardous to navigate for detailed investigation, but can be limited by weather conditions, particularly high winds and clouds, and significant financial cost to operate (Westoby et al., 2012).

Alternatively, terrestrial photogrammetry is conducted by using a camera in hand or mounted on a pole to collect photographs of a target at multiple angles. To create the highest resolution 3D rendering product, a complete coverage both vertically and around the target is ideal. Numerous applications of this terrestrial technique have focused on creating fine-scale reconstructions of the surface for geological studies. Close range photogrammetry has been used to investigate the soil erosion due to rainfall and overland flow, and investigate the change in river channel morphology over multiple data collections (Heng and Chandler, 2010; Chandler et al., 2002; Lane, 2003). Additional geologic studies include rock slope modeling and discontinuity mapping (Sturznegger and Stead, 2009; Haneberg, 2008; Krosley et al., 2006). Another benefit of utilizing terrestrial digital photogrammetry is the comparatively lower cost of single lens reflex (SLR) cameras used to generate a high spatial resolution DTM, providing



better access to this technique for geological research. However, this technique is more subject to complications by line of sight losses and has a more limited areal extent (Westoby et al., 2012). These photogrammetry techniques proved significantly higher spatial resolution models of the surface than is obtainable with current remote sensing instruments.

### **3.2.6 Roughness Calculations**

A complication of detailed surface studies is how to quantify the surface roughness remotely without direct physical measurements of the particle sizes. One method to measure this value calculates the distance from the actual surface to a best fit plain roughly defining the surface slope (Figure 16). The greater the value difference, the 'rougher' the surface. The calculated roughness factor is highly dependent on the scale used to define the best fitting plane to the surface (whether the plane is defined over an area of 0.02 m or 2 m). A surface may appear smooth when a large area is used to define the plane or rough when utilizing a small area because the detail on the surface appears rough at this scale. Numerous studies have attempted to quantify roughness including calculating the difference between slopes at different scales (Rosenburg et al., 2011), the minimum and maximum elevation difference (Pelletier et al., 2009), the root mean squared of elevation difference (Morris et al., 2008), or the standard deviation between elevations (Mundt et al., 2006). Thus, it is important to select the appropriate scale and approach depending on the purpose of the study. The main limitation of this method is the spatial resolution and errors of the dataset including the absence of data or outlying values (Campbell et al., 2003). Shepard et al., (2001) also demonstrated that anisotropic features are not sufficiently sampled nor represented in roughness profiles.

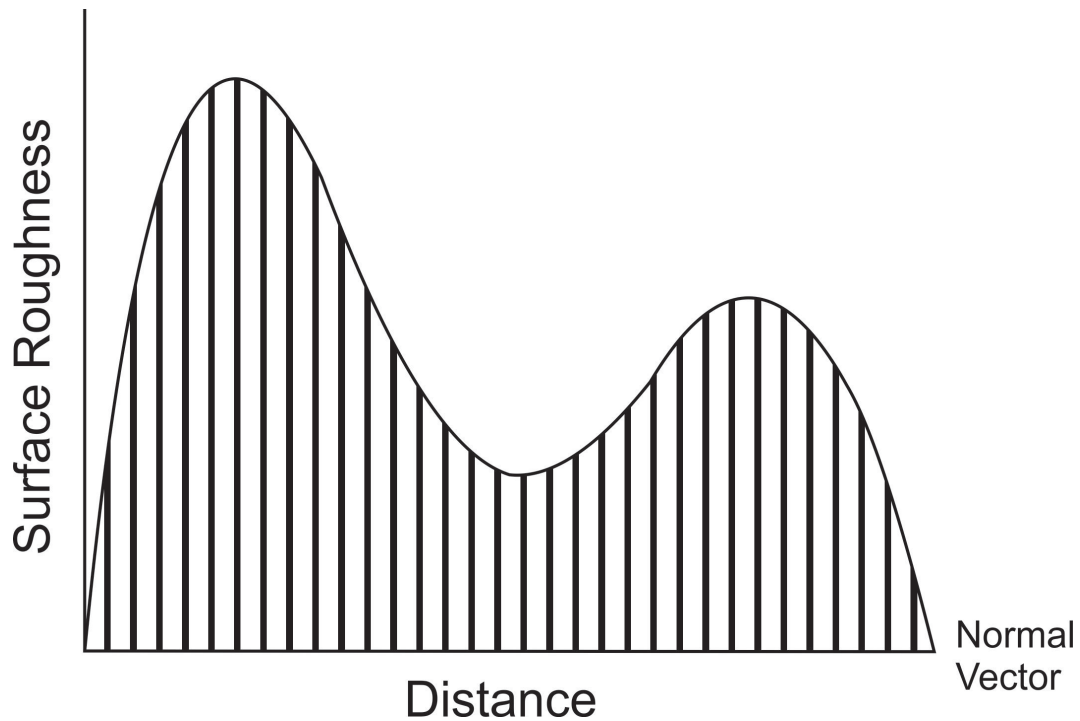


**Figure 16. Vertical profile of a simple surface demonstrating the calculation of surface roughness normalized to a slope.**

Surface roughness measurements are very useful for morphologic classifications. Whelley et al. (2014) used defined patterns in roughness textures calculated from LIDAR data to differentiate morphologic units in the Mouth St. Helens Pumice Plain. Another study applied a roughness factor to characterize alluvial fan depositions and identified a trend between this surface texture and age (Frankel and Dolan, 2007). Sankey et al. (2010) utilized this measurement to understand the relationship between eolian erosion and deposition, demonstrating that changes in surface roughness correlated with greater changes in erosion rather than deposition. Surface roughness calculations also have volcanology applications as these values can be used to identify the type of flow texture, which has direct implications for the flow emplacement processes. Morris et al. (2007) applied roughness statistics on DEMs to determine the ability of lower resolution datasets to identify variations in flow surface roughness. These

studies demonstrate the versatility of the roughness factor calculation and the potential uses to better understand the surface morphology, especially to determine the particle or block sizes present.

### **3.3 Methods**

The goals of this study are to better constrain the relationship between ATI and subpixel particle and block size distributions and determine the spatial resolution necessary to accurately identify the locations of mixed size distributions. The multi-instrument, multi-spectral approach in this study utilizes both VNIR and TIR datasets (Figure 17). VNIR data, with progressively higher spatial resolutions, were used to visually inspect and identify the surface roughness and particle and block size distributions at different spatial resolutions. TIR and VNIR data from ASTER were used to calculate the ATI values over the North Coulee.

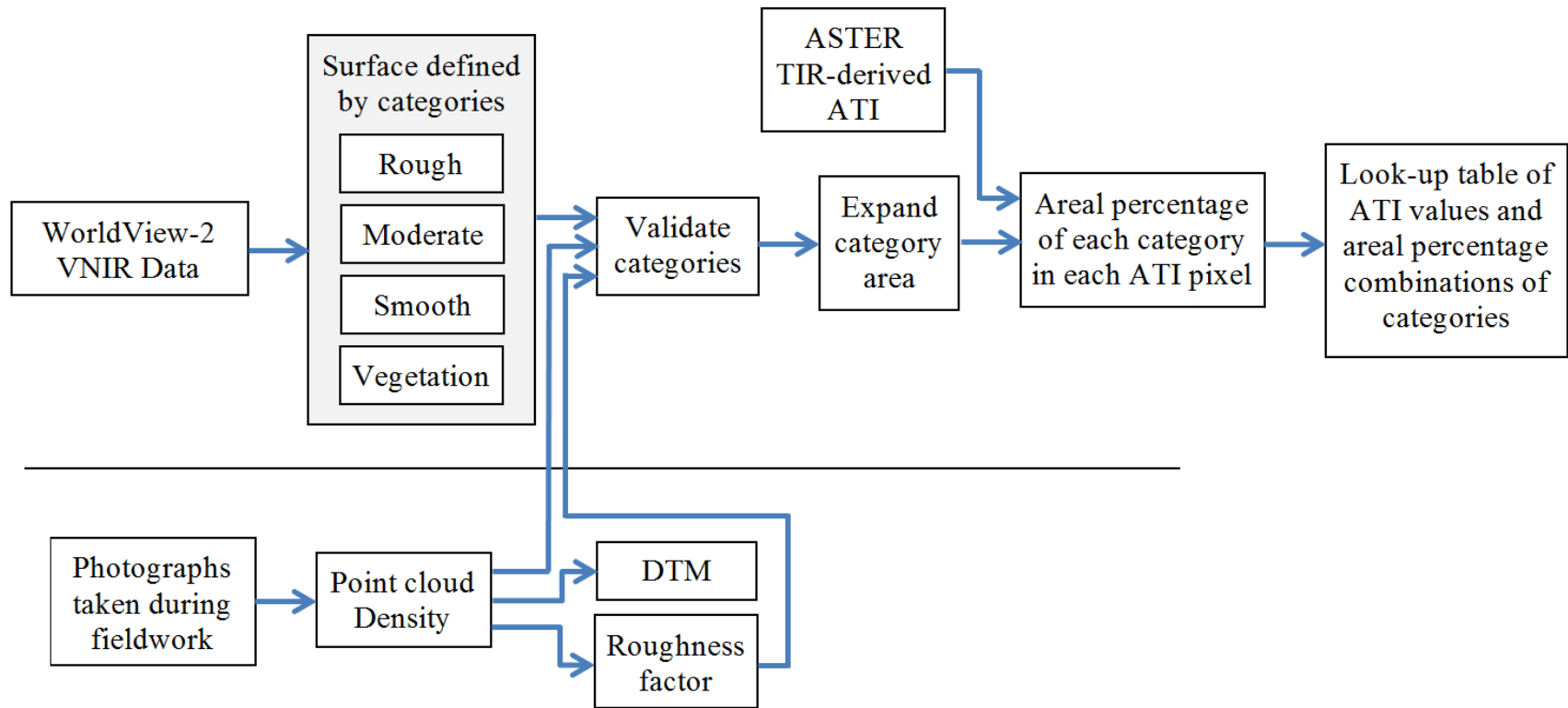


Figure 17. Flowchart of the methods used to better understand the relationship between particle and block size distributions within a pixel (mixed pixels) and ATI values.

### 3.3.1 Datasets

Utilizing a multi-instrument, multi-spectral approach, data were analyzed from the following orbital sensors at the closest dates possible to the fieldwork campaign: ASTER (15 m VNIR, 90 m TIR) and WorldView-2 (0.50 m panchromatic, 2 m multispectral) instruments (Table 4; Yamaguchi, 1998; DigitalGlobe, 2013). ASTER has three bands in the visible and near infrared (VNIR) ranging from 0.52 to 0.86  $\mu\text{m}$ ; six bands in the shortwave infrared (SWIR) ranging from 1.60 to 2.43  $\mu\text{m}$ ; and five bands in the thermal infrared (TIR) ranging from 8.125 to 11.65  $\mu\text{m}$ . WorldView-2 collects data at a higher spatial resolution of 0.5 m for the panchromatic broadband ranging from 0.450-0.800  $\mu\text{m}$  and 2 m for the 8 band multispectral ranging from 0.4-1.040  $\mu\text{m}$ .

To limit any changes in surface properties over time, all data were collected in the shortest time window possible (within a 2 month period between ASTER and WorldView-2 collection). To calculate ATI, ASTER level 2 temperature (AST\_08), level 2 VNIR surface reflectance (AST\_07XT), and level 2 TIR surface radiance (AST\_09T) data were obtained to calculate ATI values (Kahle, 1987). To produce the best calculation, the ASTER data were collected within 24 hours.

**Table 4. Dataset descriptions of instrument spatial resolution and spectral range with study applications (Yamaguchi et al., 1998; DigitalGlobe, 2013).**

Instrument	Spatial Resolution	Spectral Range	Application
Orbital Datasets			
Advanced Spaceborne Thermal Emission and Reflection Radiometer (ASTER)	15 m VNIR 90 m TIR	VNIR/TIR	Derive Apparent Thermal Inertia (ATI)
WorldView-2 (DigitalGlobe)	50 cm Panchromatic 1.85 m Multispectral	VNIR	Visible analysis of surface particle size distribution
Field Campaign Datasets			
Point cloud Density Rendering	5 cm		Visible and quantitative analysis of surface particle size distribution
Trimble XRS Global Position System (GPS)			Identify the location of control points and specific features
Thermal Imaging Camera (FLIR)		TIR	Derive the thermal properties of the surface
Sample			Identify the composition of surface materials

### **3.3.2 Field Campaign**

A field campaign was completed on the North Coulee site in July 23-30, 2014 with the main goal to identify the variation of particle and block sizes on the surface in order to ultimately better understand the relationship between ATI values and mixed pixels. The past presence of the US Pumice Corporation on this coulee provided limited access to the top surface. Due to the extensive size and areas that are rather inaccessible on foot, sampling sites were limited to the edges of the coulee surface and side slope investigations. Three main study smaller areas analyzed in greater detail include two slope areas, ‘the bowl’ (the study site for the photogrammetry validation project), and a large fine-grained pumice deposit on the western edge (Figure 18). These areas were selected to investigate a pure pixel with a single type endmember, specifically the pumice deposit, and various mixed pixels with different particle and block sizes.



**Figure 18. Photographs of the sampling areas investigated during the field campaign: (A) coulee slope, (B) 'the Bowl', and (C) fine grained deposit.**







To achieve the study goals, a variety of data were collected for image validation and further laboratory analysis including from a global position system (GPS), a thermal imaging camera (FLIR), photographs, and samples to assess the roughness and particle and block size distribution on the surface. To assess the particle size of the mantling deposits and confirm the composition of the surface, samples of the mantling and underlying sediments were collected along with four larger rocks. At each of the study sites, the mantling depth was estimated with particular care taken to identify the range of particle sizes present. Particle size boundaries were geolocated using GPS with a spatial accuracy within 30-50 cm. Photographs taken during the field campaign were processed using photogrammetry techniques to produce high resolution point clouds, each containing four GPS georeferenced points. These data were used to better understand the relationship between ATI and mixed pixels.

### **3.3.3 Categories: Particle Sizes and Vegetation**

To identify the particle and block sizes present on the surface using orbital datasets, four categories were defined based on qualitative analysis of WorldView-2 VIS data (Table 5, Figure 19). Three of these categories are based on the particle and block sizes of material on the surface (rough, smooth, and moderate) and the fourth defined the locations of vegetation. The goal of this classification was to identify the mixtures in particle and block sizes present on the surface which would ultimately have significantly different ATI values. The coarse category represents the location of the largest block sizes on the North Coulee, consisting of large blocks or boulders based on the Wentworth scale (1992) and are defined in the VIS data as areas that are poorly sorted with significant amounts of shadowing present. The moderate category represents the intermediate material roughly cobble size (~200 mm) and are identified based on the presence of

intermediate sorting and minor shadowing. Smooth regions represent sand or fine particles ranging in size from granules to below and are identified by the highly sorted feature with a lack of shadowing. Vegetation, in the form of large trees, was identified because it will mask the characteristics of the surface material and potentially complicate the derived signature. The described criteria were applied to WorldView-2 to identify location and distribution of these categories. Unique shapefiles were created to identify the areal coverage of each category on the surface of the North Coulee. To validate this classification technique, a subsection of the surface at 'the bowl' was initially used for comparison with the higher spatial resolution photogrammetry data.

**Table 5. Description of the four category types, three based on particle and block sizes and the fourth on vegetation, used to define surface characteristics.**

Category	Particle Size	Visible Image	Example from WorldView-2
Coarse	Large blocks	Poorly sorted, Shadowing	
Moderate	Moderate sized rocks	Intermediate sorting, Minor shadowing	
Smooth	Sand/fine particles	Highly sorted	
Vegetation	Trees	Individual green features	

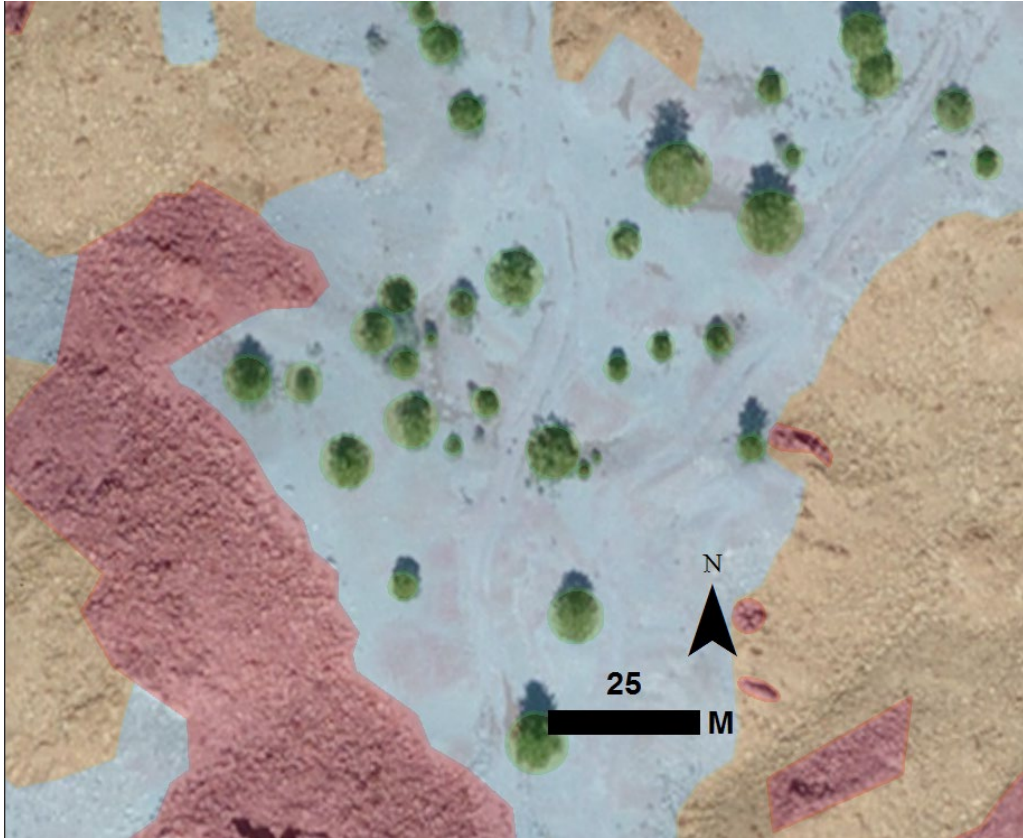
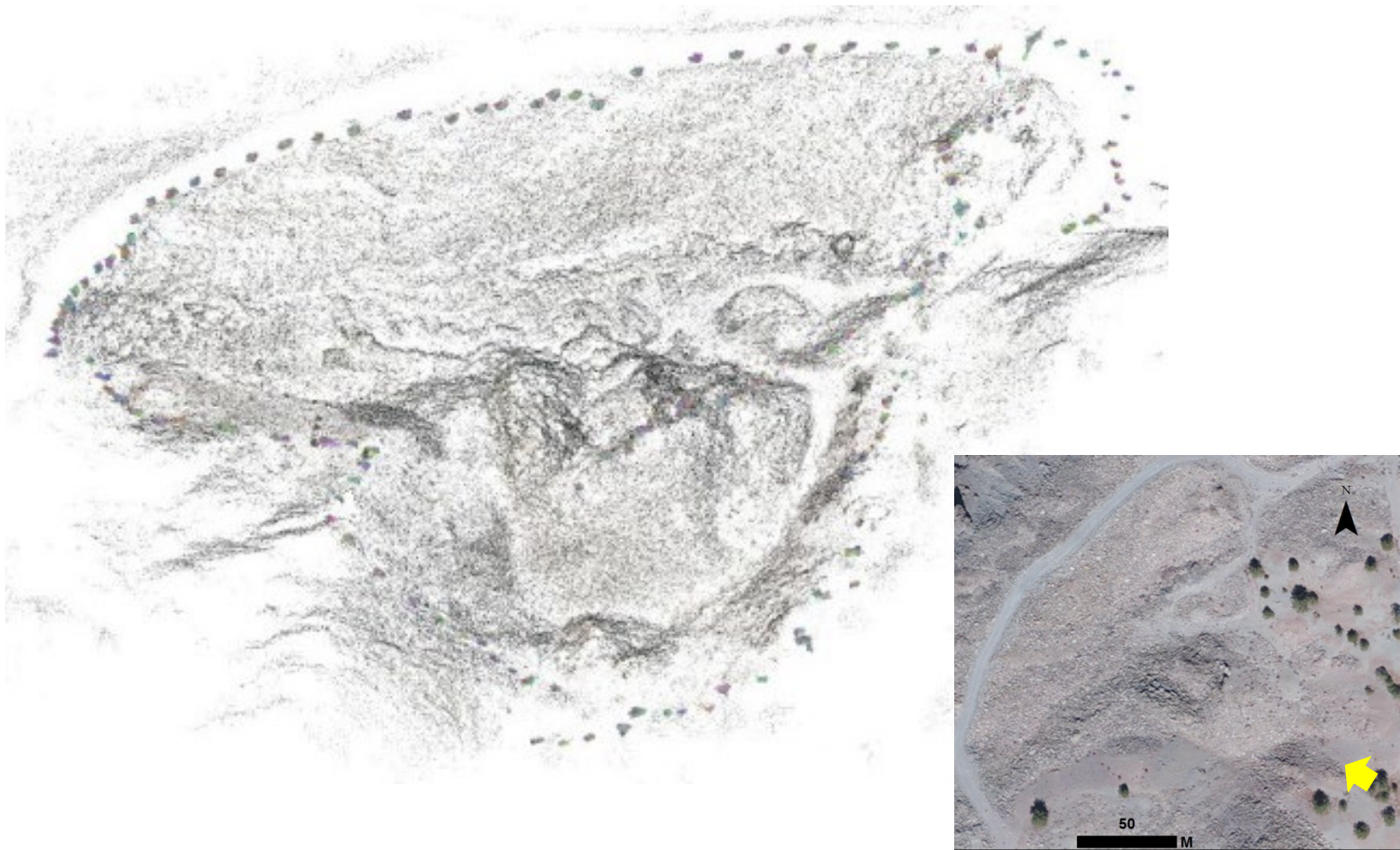


Figure 19. Examples of the four category types overlain on WorldView-2 data to demonstrate the variation seen on the surface (DigitalGlobe, 2013).

### **3.3.4 Photogrammetry Dataset and Category Assessment**

To validate the four categories, Structure from Motion was used on over 12000 images collected during the field campaign to produce derived point cloud products of specific locations on the coulee surface. One such site was labelled ‘the bowl’ (for the distinct topographic shape of a depressed area), which was selected for the significant variation in particle and block sizes present and the coverage by multiple ASTER ATI pixels (Figure 20). Photogrammetry processing produced a 3D density point cloud and DTM at a 5 cm spatial resolution with geolocation information, providing the most surface detail of all the datasets in this study. The 3D density point cloud provided the equivalent to a mesh model of the surface to be used both qualitatively and quantitatively. The first application of this data was to qualitatively assess the accuracy of the defined category zones on this test site. Using the point cloud and photographs from the field campaign, the boundary areas between the categories were defined at this higher spatial resolution. The categories defined using WorldView-2 data were overlain on the density point cloud to visually identify any errors or inconsistencies. After the accuracy of the classification method was determined, the higher spatial resolution data were used as further training to accurately identify the categories in the WorldView-2 data.



**Figure 20. 3D rendering of the point cloud from photographs taken during the field with dots representing the location of image captures. WorldView-2 image of the northeast corner of the North Coulee with yellow arrow demonstrating the perspective of the 3D point cloud rendering (DigitalGlobe, 2013).**

### **3.3.5 Roughness Calculations from Photogrammetry Dataset**

Another method to quantitatively validate the uniqueness of each category utilizes the density point cloud to calculate a roughness factor of the surface at each point. This roughness value is determined by defining the distance between each point and the best fit plane to the surface representing the general slope in a define area. Using this method, the regional slope is removed from this calculation to create a factor to solely capture the particle or block size present. Thus, this is based on the user defined kernel size that determines the area by which the best fitting planes is calculated. To select the best kernel size for this study, the range of particle and block sizes present in ‘the bowl’ were evaluated to insure that the largest size would be captured in the roughness factor. Ultimately, a kernel size of 2 m was selected as the best representation of the surface roughness to capture the variation in surface material. The resulting scalar values correlate roughly to the size of the surface material because larger objects will produce a greater distance between a point on the surface of the object and the best fitting plane, thus producing higher roughness values. Alternatively, small particles such as sand will have a small distance between points on the grain surface and the best fitting plane. To determine the uniqueness of each category and thus validate the method, the correlation between the roughness values and each category type were defined.

### **3.3.6 Categories and ATI**

With the validation of the categories defined using WorldView-2 data, the classification of the surface was expanded on the top surface of the North Coulee to cover as much range as

possible of different particle and block size distributions within a mixed pixel. The goal of this classification was to capture the full range of possible pixel representations ranging from a pure pixel with a single category endmember to a variety of mixed pixel combinations with different distributions of the categories. With the completion of the classification, the areal percentages of each category were calculated for 201 ATI pixels covering the coulee (i.e. the percentage of the ATI area that was covered by a particular category) to produce an extensive look-up table (LUT). This LUT was used to quantitatively assess the relationship between ATI values and subpixel particle and block size distributions represented by the three categories and identify any linear or non-linear trends between increases in ATI values and varying category distributions.

### **3.4 Results**

#### **3.4.1 Category Evaluation**

Comparison of the categories defined at the resolutions of the WorldView-2 and density point cloud data suggests the orbital data provide comparable results with only minor variation along the boundary zones, predominately between moderate and rough categories, and less than 10% difference in the entire study area of ‘the bowl’ (Figure 21). This indicates that using this method the WorldView-2 data is adequate to assess surface particle and block size distributions. Initial assessment of the ATI values in and around ‘the bowl’ area and the corresponding areal percentages of the categories further demonstrate the applicability of this method.

Interpretation of the moderate ATI value of pixel 1 (Figure 21D) suggests that the pixel area should contain larger particle or block sizes compared to pixel 2. The breakdown of the



areal distribution of the categories suggests that the pixel is dominated by the moderate particle size at ~53% with ~24% coarse and also ~23% finer material. This analysis provides critical information about the subpixel particle size distributions that would produce a particular ATI. Higher ATI values may either contain a uniform covering of medium size rocks or distinct regions of large blocks and finer particles. The neighboring pixel 2 (Figure 21D) with a lower ATI value suggests this area should contain smaller particle sizes. Analysis of the category distribution shows over 76% of the area is identified as fine with a 10% presence of vegetation within the pixel boundaries. However, the small percent of moderate (11%) and coarse (4%) material will slightly elevate the ATI value over that of a uniform fine grained area (pure pixel). Thus, this initial analysis demonstrates that the categories represent the particle and block size distributions and a continued in-depth quantitative assessment of these category distributions is necessary.

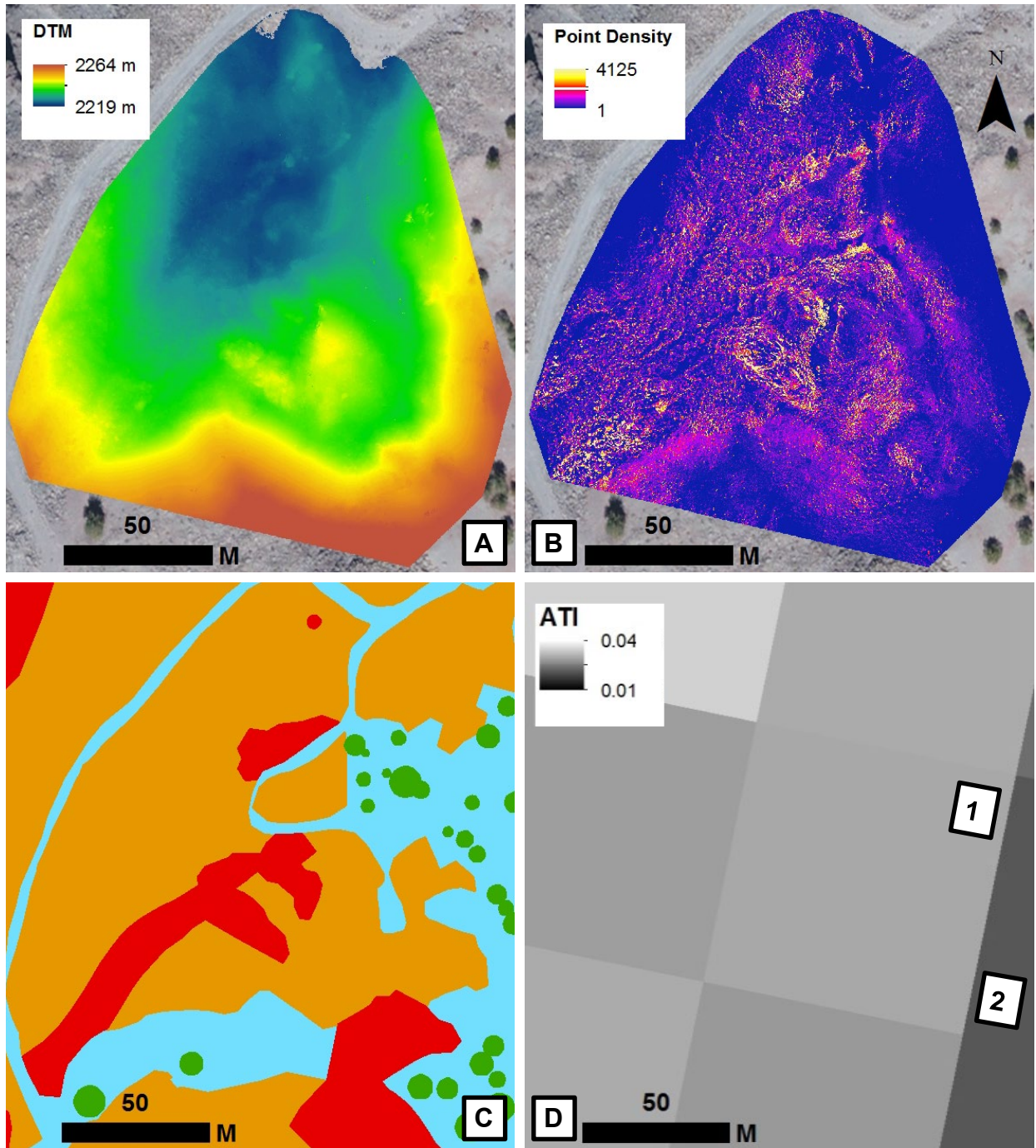


Figure 21. Northeast lobe of the North Coulee study site. (A) DTM, created from the point cloud data, to interpret local topographic slopes. (B) Point cloud density for visual interpretation of surface particle and block size distribution (5 cm). (C) Category shapefiles defined from WorldView-2 data to determine the accuracy of particle size identification (DigitalGlobe, 2013). Categories: red = coarse, orange = moderate, blue = fine, and green = vegetation. (D) ATI data with identified pixels 1 and 2 labeled for discussion.

### 3.4.2 Roughness Calculation of Categories

Comparison of multiple kernel sizes (the area used to define the best fitting plane) demonstrates that a kernel size of 2 m produces a roughness at the scale of the study (Appendix B). Kernel sizes greater than 2 m highlighted the topography rather than the particle and block sizes present. Those lower than 2 m lost the block size features and eventually were at such a fine scale that a majority of the surface displayed as rough. The ideal kernel size identifies the particle size scale from fine (sand and smaller) to large rocks or boulders. Using the photogrammetry density point cloud and DTM, a range of values were defined for each category representing the maximum roughness factor for a feature of that category at a particular sampling size (Table 6). The roughness calculations demonstrate a stark difference between the categories present on the surface of the North Coulee, validating the uniqueness of each class (Figure 22). Roughness factor limits demonstrate the variation between the categories is statistically significant from each other. The variance between the moderate and coarse categories is smaller than that between the smooth and moderate categories, demonstrating a closer similarity between former categories. Areas defined as smooth show the smallest range in roughness values demonstrating the almost uniformity of the surface in regards to vertical variation and suggesting that these areas have relatively even horizontal distribution with a lack of buildup in a singular area. With the results suggesting that these categories represent distinct groupings of particle or block sizes, the ground truth photogrammetry data provides the information to extend the classification on the surface of the North Coulee.

**Table 6. Category descriptions and maximum calculated roughness range from the photogrammetry dataset.**

Category	Particle Size	Visible Image	Maximum Roughness Range
Coarse	Large blocks	Poorly sorted, Shadowing	0.7560-0.8108
Moderate	Moderate sized rocks	Intermediate sorting, Minor shadowing	0.5450-0.6810
Smooth	Sand/fine particles	Highly sorted	0.1270-0.1550
Vegetation	Trees	Individual green features	

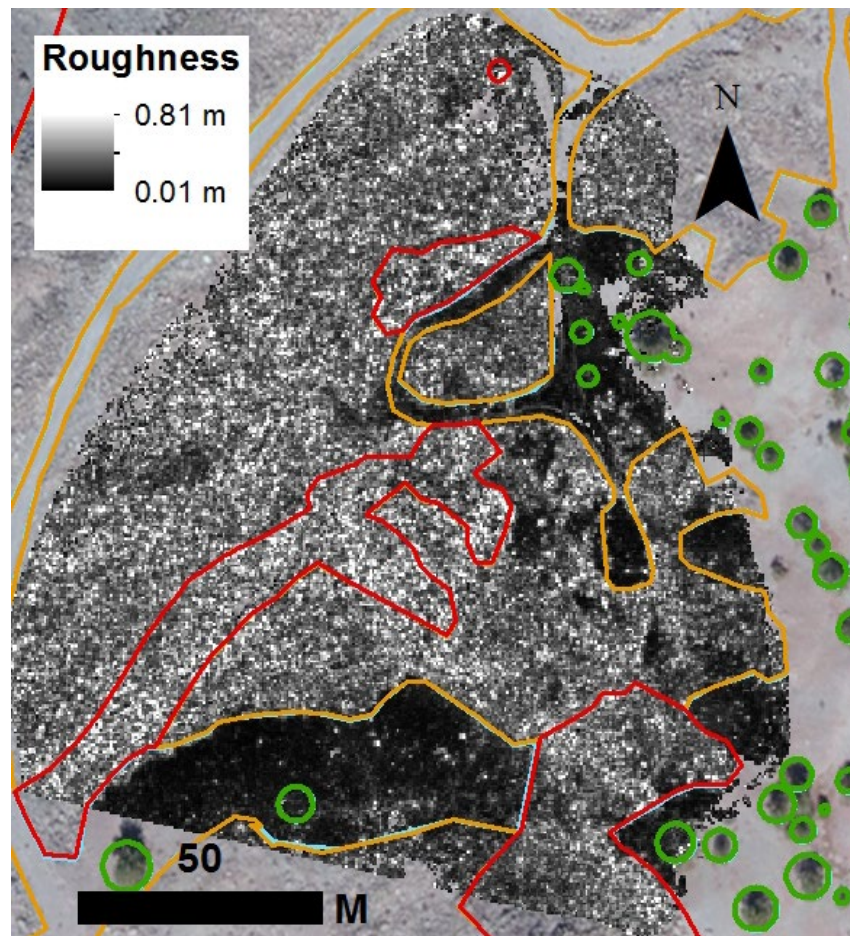


**Figure 22. Roughness calculation from the density point cloud with a kernel size of 2 m demonstrating the variation present in ‘the bowl’ study area.**

### **3.4.3 Location Distribution**

Analysis of the expanded region demonstrates a significant trend in the location of the three particle and block size categories (Figure 23). Sand and finer particles dominate the western and south western sections of the North Coulee surface and moderate and coarse categories are found predominantly along the middle of the coulee surface extending to the eastern portion. One explanation for this localized distribution of particle sizes suggests the effect of wind deposits and weathering. In the Mono Craters region, the winds predominately originate from the West direction over the Sierra Nevada mountain range. These winds deposit finer particles on the windward side of the elevated coulee due to the significant change in topography. This buildup of material may also have initially formed from winds during the eruption of younger vents depositing fine material. The coarse category makes up the smallest population on surface of the North Coulee and predominately surrounded by moderate material. Furthermore, vegetation almost exclusively is found among the smooth category. This is expected since vegetation will grow in loose material such as sand or finer particles.



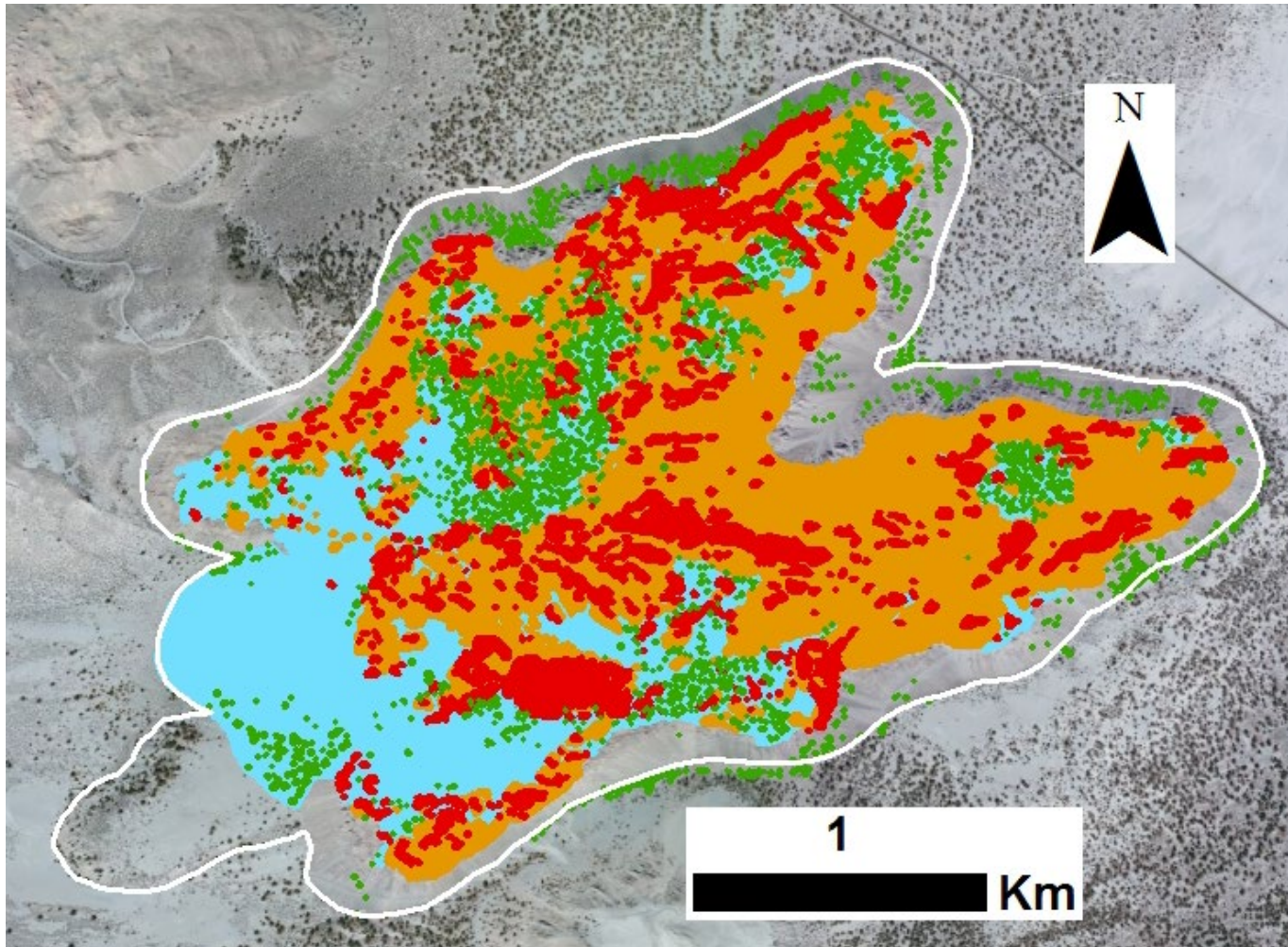


Figure 23. Category distributions (red=coarse, orange=moderate, blue=smooth, and green=trees) on WorldView-2 data with white outline of the North Coulee boundaries (DigitalGlobe, 2013). This study focused on the top of the coulee to avoid any complications from significant slopes.

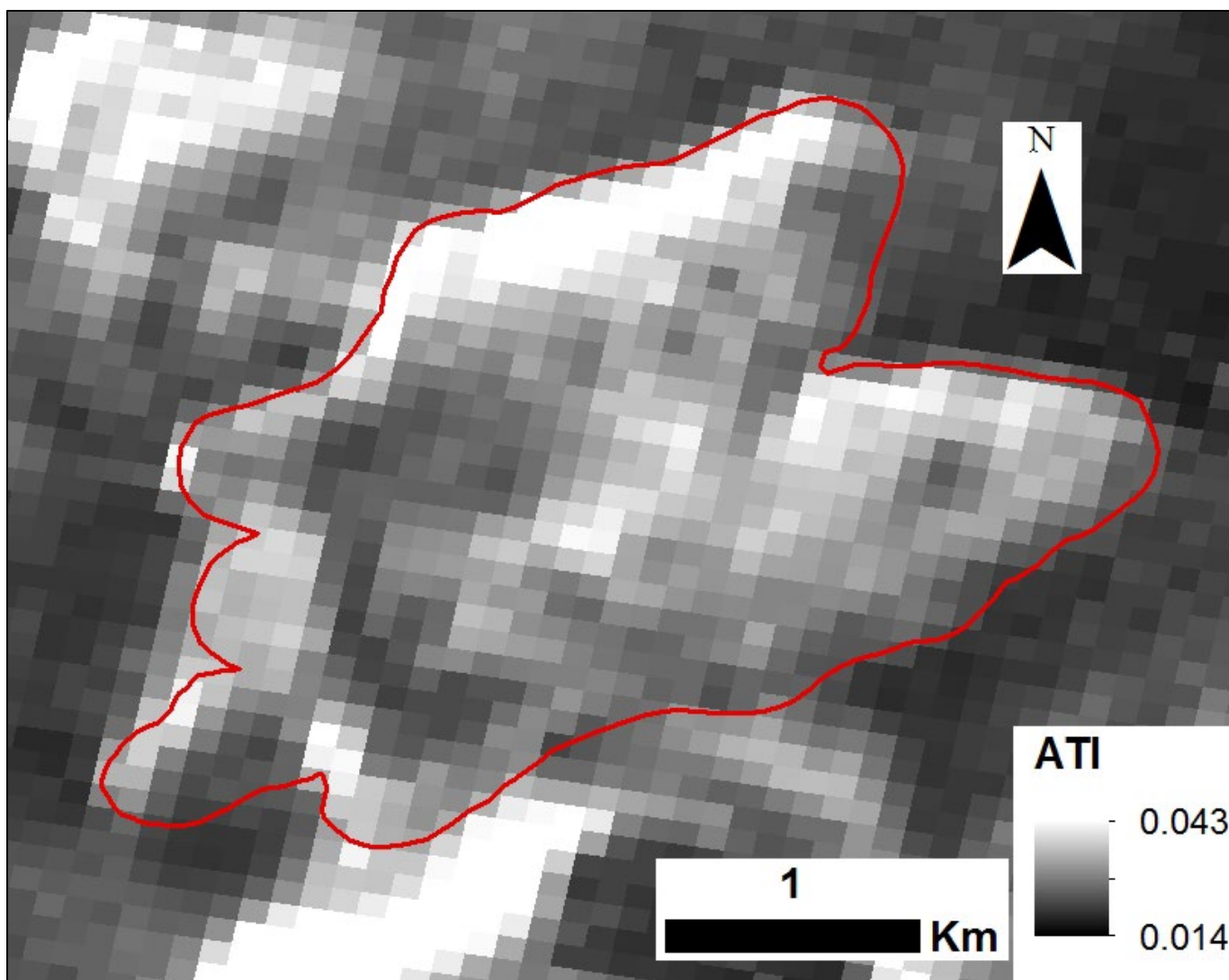


Figure 24. Calculated ATI values from ASTER visible and thermal infrared data displaying the variability in the study area. The red outline displays the boundaries of the North Coulee.

#### **3.4.4 Category Distributions and ATI**

Defining the areal percentages of each category within the ATI pixels provided a thorough analysis of possible particle and block size combinations that would produce the same ATI value (Figure 23 and Figure 24). With the investigation of over 201 ATI pixels with a range of values from 0.019 to 0.031, North Coulee surface was classified in this work to sample a variety of particle and block size combinations including pure pixels covering a single category. It is critical to identify multiple pure pixels to act as endmembers for understanding the variety of mixed pixels. By capturing areas completely covered by a single type of particle size category, the extreme minimum and maximum sections of the ATI range can be accurately assessed and the properties of each category can be better understood. Specific trends were discernable in the look-up table (LUT) comparing the particle sizes present and the ATI value.



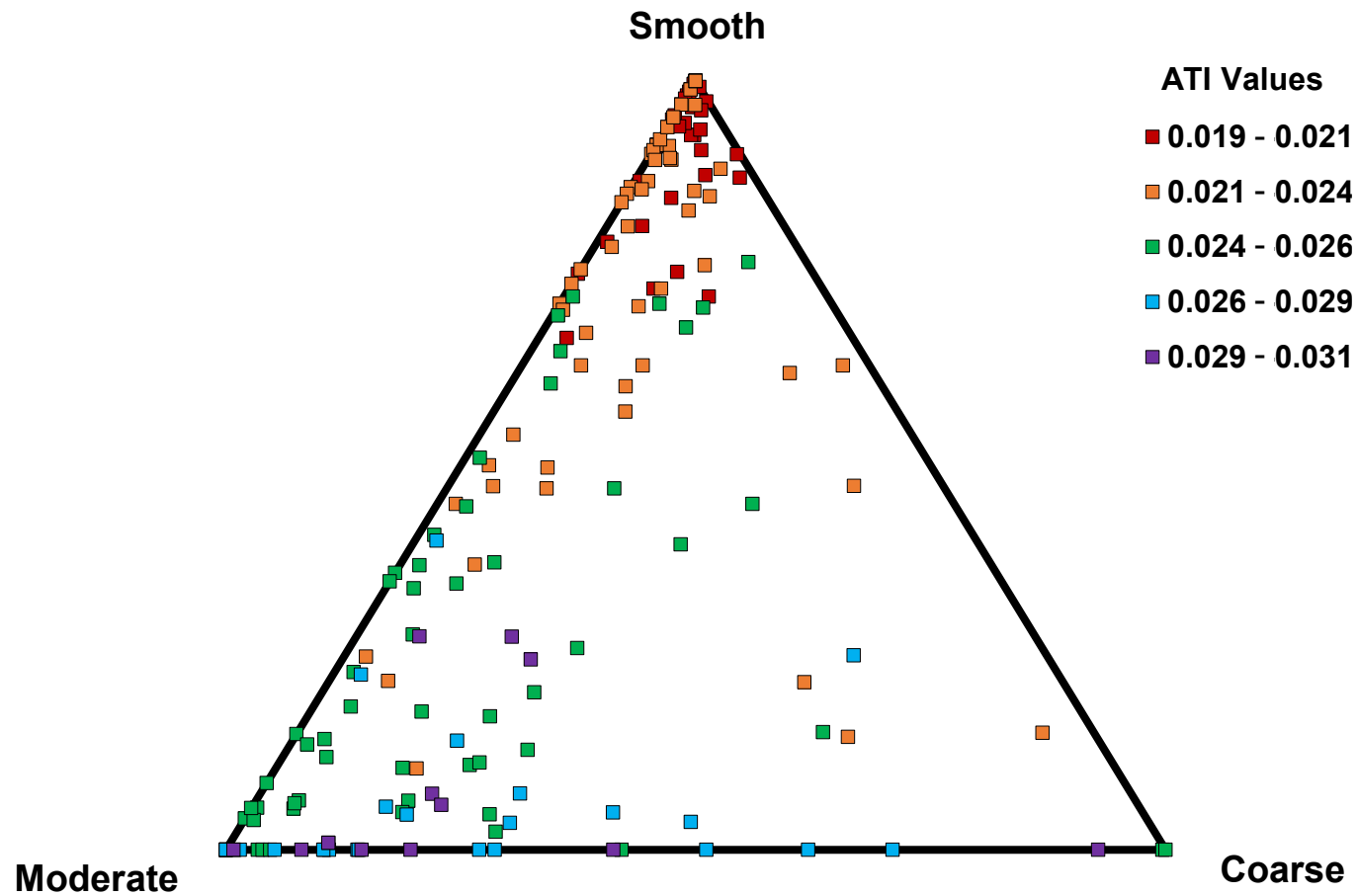


Figure 25. Ternary plot of the three particle size categories demonstrating the relationship between mixed pixels and ATI values on the surface of the North Coulee. The sample interval for the ATI values is determined by five equal divisions.

### **3.4.5 Improved Relationship between ATI and Mixed Surface Properties**

The analysis of the areal percentages of each category within a pixel and the corresponding ATI value proves critical information to improve the understanding of how subpixel particle and block size mixtures, aka mixed pixels, affect the ATI value (Figure 25). Initial assessment demonstrating that, as expected, those pure pixels covered solely by the smooth category displayed the lowest ATI values (0.019-0.022 tiu). Lower ATI pixels up to roughly 0.025 tiu also possess a significant amount of vegetation (up to 12%), the presence of which increases the ATI relative to a completely fine surface. The higher range of ATI values on the flow surface of the North Coulee range from 0.025 to 0.031 tiu and is dominated by moderate and rough particle sizes. The surfaces of the highest ATI values (maximum of 0.032 tiu) are actually dominated by moderate particle sizes and pure pixels covered singularly by the coarse category did not consistently display the highest ATI values. This suggests that at the particle size of the moderate category, the rocks create an inverse size grading in which the largest objects are on the top that create empty pockets allowing finer particles to settle beneath. Thus, the ATI values likely display the accurate response of the moderate particle size rather than a mixture of moderate and fine particle sizes. The lower than expected ATI value (~0.025 tiu) for the two pure pixels containing the coarse category suggests that these pixels do not solely represent the signature of the large block material. Even though the areas covered by pixels display the criteria to qualitative classify them as coarse using WorldView-2 data, multiple large boulders would be present which likely contain exposed fine or moderate material collected between them. This would ultimately create a mixed pixel response that would increase the daytime temperature sampled by the ASTER dataset and decrease the calculated ATI value.

Overall, pixels with a lower ATI value that occur toward the bottom of the ternary plot (Figure 25) represent surfaces with high amounts of vertical layering by finer particles and the higher ATI values for this study area are dominated by higher concentrations of moderate sizes. Analysis of the mixed pixels and corresponding ATI values demonstrate that different combinations of the three categories can produce very similar ATI values. However, specific trends can be seen within the data. Mixed pixels with over ~70% areal percent of fine particles are dominated by the signature of the fine category (0.019-0.02 tiu) even where moderate and coarse materials are present. The moderate range of 0.024-0.026 tiu specifically demonstrates that different combinations of the categories can produce similar ATI values, however, these combinations mainly occur with changes in the moderate and fine category distributions. ATI values higher than 0.0266 tiu predominately occur with fine category percentages of 20% or less and at least ~30% presence of the moderate category. ATI values in this higher range (0.027-0.031 tiu) also display different areal percentage combinations of moderate and coarse categories for the same ATI value. The moderate and coarse areal combinations can vary by up to 12% and still produce the same ATI value. This analysis demonstrates that the current assumption of uniform material properties at the pixel scale causes inaccurate estimates for the derivation of large particle sizes from ATI values. Furthermore, without additional information about the surface for mixed pixels with ATI values in the middle of the spectrum, it is difficult to accurately assess the surface properties because in this range various combinations of different particle and block sizes can produce the same value. This further suggests that within this range, none of the particle or block sizes are dominating the calculated value.

### 3.5 Conclusions

The current assumption of uniform properties at the pixel scale (i.e. a pure pixel with only a single class) causes significant error in deriving particle size from remote thermal datasets. In reality, the surface usually contains a mixture of particle sizes (i.e. mixed pixel) that would produce an average ATI value of each material present. The goal of this project is to better understand and constrain the relationship between ATI values and mixed pixels with subpixel particle size variations. An additional component of this project included determining whether or not different particle sizes are identifiable in satellite VIS data. Multiple datasets were used to accomplish this task including ASTER, WorldView-2, and photogrammetry derived point cloud and DTM. ASTER data were used to calculate the ATI over the study area and WorldView-2 and the photogrammetry datasets were used to define the particle size distribution on the surface of the North Coulee.

To interpret the distribution of different particle sizes on the surface of the coulee using satellite data, four categories were identified at the WorldView-2 spatial resolution: three particle size classes fine, moderate, and coarse and a vegetation class. These classes were defined visually based on identifiable features in WorldView-2 data such as the presence of shadowing and degree of sorting. Comparison of the density point cloud data (at a resolution of 5 cm), created using photogrammetry techniques, with the category distributions based on WorldView-2 data (at 2 m resolution) demonstrated that the spatial resolution of the satellite data was sufficient to identify particle size differences. A roughness factor calculated from the density point cloud data statistically validates the uniqueness of each class as the categories display a distinct difference between each other.

Analysis of the distribution of categories on the surface of the coulee (for both pure and mixed pixels) and the ATI values reveals distinct correlations between the datasets. Fine particles dominate the lower portion of the ATI range for this study site and the presence of vegetation slightly increases the ATI value. Pixels identified as predominately moderate in particle size correspond to the highest ATI values and those covered by coarse material display an intermediate ATI value. This suggests that pixels covering the coarse areas do not solely represent the signature of the large block material and the areas between multiple large boulders likely contain exposed fine or moderate material that would lower the ATI value. In areas dominated by moderate particle sizes, the rocks rest in such a way on the surface to create an inverse size grading that allows for smaller particles to settle beneath in empty pockets. Thus, the ATI values for pure moderate pixels are likely to display the accurate response for this particle size. This analysis demonstrates that, with the current assumption of uniform material properties at the pixel scale, boulders and other large block sizes will be completely missed in estimations of particle size from ATI values alone. Additionally, the intermediate values of ATI are the most affected by the mixed pixel problem where different combinations of particle and block sizes will produce similar values. Within this region additional datasets are required, such as the WorldView-2 data, to accurately differentiate the presence of particle and block sizes on the surface.

### **3.6 Acknowledgements**

This research was supported through continuing funding of an original Mars Odyssey Participating Scientist Program project (grant number: NMO710630) and a NASA Earth and

Space Science Fellowship (award number: 80NSSC17K0460). All WorldView-2 data was supplied by the DigitalGlobe Foundation through an imagery grant. ASTER data used in this study are available at Earthdata Search application: <https://search.earthdata.nasa.gov/>.

## **4.0 The Unusual Thermophysical and Surface Properties of the Daedalia Planum Lava Flows**

### **4.1 Introduction**

Mantling of the Martian surface by dust and sand hinders remote spectral investigations of surface properties, particularly in the dusty Tharsis region (Malin et al., 2007). Therefore, it is vital to identify the degree of eolian mantling that may obscure a study site in order to perform an accurate analysis of surface processes or bedrock spectral signature(s). One approach to this is using thermal infrared (IR) data to investigate the degree and distribution of the mantling material before focusing on the composition of the underlying rocks. Thermal properties are used to identify particle size based on the grain-size dependence of thermal conductivity (Presley and Christensen, 1997). Modeled thermal conductivity measurements under Martian conditions suggest that low thermal inertia (TI) regions, such as those seen at Daedalia Planum, may not be due solely to an optically thick layer of dust (Mellon et al., 2014).

Recent studies have focused on using high spatial resolution image data to investigate geomorphological surface features in Daedalia Planum (Warner and Gregg, 2003; Ramsey et al., 2015; Crown et al., 2015; Crown and Ramsey, 2017). The likely basaltic extrusive volcanism in this region (Warner and Gregg, 2003, Lang et al., 2009) shows flow morphologies similar to those of terrestrial pahoehoe and a'a flows with complex overlapping relationships (Crown and Ramsey, 2017). Age estimates using crater counts demonstrate that this region has numerous young lava flows (Berman and Crown, 2019). Furthermore, analyses of apparent surface emissivity and temperature collected by both the Thermal Emission Spectrometer (TES) and the

Thermal Emission Imaging System (THEMIS) led Bandfield (2009) to conclude that this region has some of the highest RMS surface roughness on the planet, further suggesting a relatively young age. However, there has been limited work using thermal IR datasets due to the perceived degree of dust cover. Ruff and Christensen (2002) derived a dust cover index (DCI) for Daedalia Planum ranging from  $\sim 0.97$  near the southern boundary to  $\sim 0.94$  in the north, approaching the higher elevations of Arsia Mons, whereas the TES-derived visible albedo spans a range from 0.22 - 0.28, both considered moderate to high for dust cover (Christensen et al., 2001).

Despite the DCI and albedo, the most interesting thermal IR data of this region are the unusual thermophysical properties of individual flows. At the higher spatial scales of THEMIS, it is clear that it is not a uniformly dusty region. Neighboring lava flows display thermal diurnal responses that are distinct from one another, which led Ramsey and Crown (2010) to initially investigate this region for the possibility of using thermal IR spectral analysis. THEMIS decorrelation stretch (DCS) data and spectral analysis of small portions of individual flows (e.g., levee versus channel, rough flow versus smooth flow) revealed subtle spectral and thermophysical differences, leading to the conclusion that the region has a complex interplay between surface roughness, albedo, mantling, and the underlying lava composition. However, the specific relationship(s) between these components remained unresolved.

The initial methods and observations (e.g., decorrelation stretch and surface temperature) of those prior TIR studies helped to define the thermal properties of some of these flows and provided the groundwork for this study. These approaches were examined in greater detail and at a higher level of qualitative analysis that combined new approaches to determine the cause of the observed thermophysical differences between the flows. The small-scale thermophysical variations appeared to be caused by eolian infilling of lava flows in Daedalia Planum (bounding



coordinates: longitude 120.4-127.5° W; latitude 22.0-26.8° S). Here, we develop a classification approach to identify areas that consist of different mixtures of large lava outcrops, sand, and dust. We show that these flows may have localized regions of minimal to no dust cover with a checkerboard (linear mixture) style of rock plus sand/dust.

## **4.2 Background**

### **4.2.1 Geologic Setting**

Arsia Mons (~120° W and 9° S), the southernmost of the three Tharsis shield volcanoes, is aligned along the Tharsis rise and has a prominent summit caldera (Crumpler et al., 1996; Head et al., 1998a; Head et al., 1998b; Mouginis-Mark, 2002). It is approximately 20 km high and 450 km in diameter. It has produced some of the youngest and most profuse lava flows on Mars (Garry et al., 2018; Crown et al., 2015; Crumpler et al., 1996; Lang et al., 2009). Large flow fields originate from the NE and SW flanks; these postdate and surround the main shield (Scott and Zimbelman, 1995; Bleacher et al., 2007; Garry et al., 2014). The SW flow field extends from the base of Arsia Mons and forms Daedalia Planum, a sparsely-cratered lava plain within the Memnonia and Phoenicus Lucas quadrangles of Mars (Figure 26). Prior spectral investigations focused primarily on the southern portion of the region because of the lower TES-derived visible albedo and DCI of Ruff and Christensen (2002). For example, analysis of Visible and Infrared Mineralogical Mapping Spectrometer (OMEGA) spectral data revealed the presence of two classes of tholeiitic basalts in the SW portion of Daedalia Planum with varying abundances of Ca-pyroxene (Giacomini et al., 2012; Lang et al., 2009). Giacomini et al. (2009,

2012) used Mars Orbiter Laser Altimeter (MOLA) and THEMIS image mosaics to develop a unit map and identify inflation features based on surface texture similarities and stratigraphic relationships. However, some of the most recent flows are located in the NE portion of the Arsia Mons SW flow field, which is the focus of this study. These have estimated ages of only a few 100 Ma (Crown et al., 2015; Berman and Crown, 2019). Crown et al. (2015, 2010) has completed detailed mapping of the flow boundaries and superposition relationships documenting intricate flow patterns and complex overlapping and interfingering relationships.

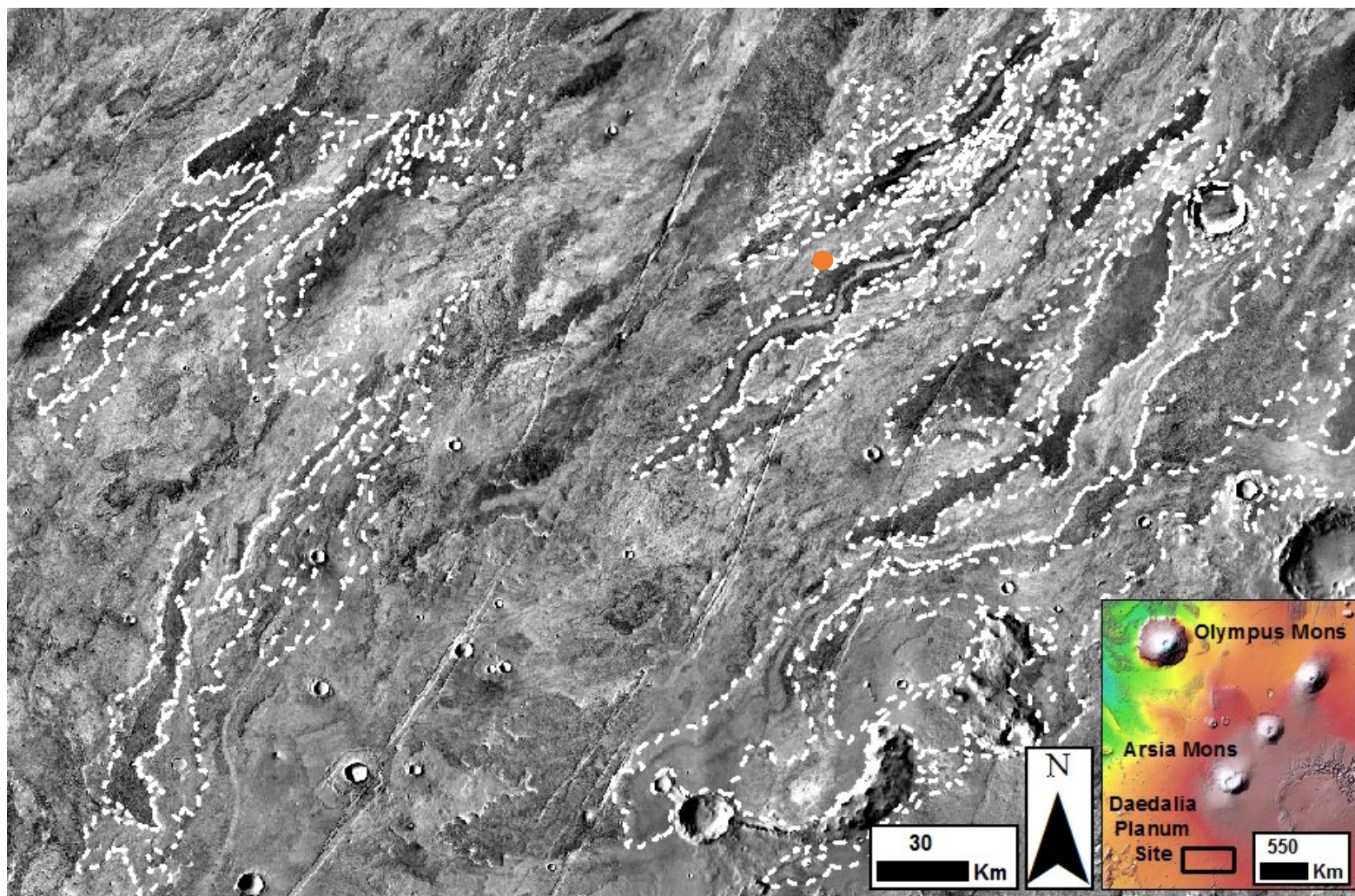


Figure 26. THEMIS daytime thermal IR brightness temperature mosaic by Edwards et al. (2011) with lava flow margins (white, dashed) by Crown et al. (2015). The orange dot signifies the center location of Figure 27a-c. The MOLA color inset for regional context shows the study area denoted with the black rectangle. Bounding coordinates: longitude 120.4-127.5° W and latitude 22.0-26.8° S.

#### 4.2.2 Thermophysical Response and Thermal Inertia

Thermal IR remote sensing is a powerful tool to investigate surface geology, providing data on the mineralogy, temperature, and thermophysical properties. Two main methods by which the surface particle size distributions can be estimated using thermal IR data are analyzing the diurnal temperature response or modeling the thermal inertia (TI).

Surface temperature at the time of data acquisition is derived directly from thermal IR data. The temperature of the surface measured over the course of a day comprises the diurnal curve, which provides unique information about the material properties (e.g., particle size distribution, the presence of water, ice and/or cemented crusts). In general, for material with the same composition, smaller grain sizes will reach the highest maximum daytime temperature and have the fastest cooling rate over the diurnal cycle compared to larger particle sizes, or rocky surfaces, will have a lower maximum daytime temperature and the smallest diurnal change. Thus, the temperature from multiple collection times can be used to constrain the distribution of particle sizes or thermophysical units on the surface (Kieffer, 2013).

TI represents the resistance of a material to changes in temperature over the diurnal cycle and is used to derive specific surface properties such as block and particle size distribution, moisture content, and degree of cementation (Pratt and Ellyett, 1979; Hardgrove et al., 2009). Thermal inertia ( $I = \sqrt{k\rho c}$ ) is calculated directly from the thermal conductivity ( $k$ ), thermal capacity ( $c$ ), and bulk density ( $\rho$ ) of the material, in units of  $\text{J m}^{-2} \text{K}^{-1} \text{s}^{-0.5}$ . Prior studies show that the variation in TI is dominated by thermal conductivity and, under Mars atmospheric conditions, particle size is the most influential factor in conductivity measurements (Neugebauer et al., 1971; Jakosky, 1986; Presley and Christensen, 1997, Kieffer et al., 1972, Fergason et al.,

2006). Therefore, for material with the same composition, small grain sizes, such as dust, have low thermal inertia values, sand size grains have intermediate values, and larger sizes, or rocky surfaces, have the highest values. All TI data presented here are derived from Mars Odyssey THEMIS nighttime temperature data (Fergason et al., 2006).

#### **4.2.3 Dust Cover**

The primary complication of using thermal IR data for the study of the lava flow fields in Daedalia Planum is the presence of varying levels of surface dust. Even though some sand or dust deposits may have a local origin and therefore preserve the compositional signature of the source bedrock, it is difficult to determine the source using orbital data alone (Edgett and Lancaster., 1993; Johnson et al., 2002). Typically, Martian dust is spectrally bland and globally homogenized. Results by Johnson et al. (2002) demonstrate that thin coatings of dust 10-20  $\mu\text{m}$  thick significantly reduce the spectral contrast of the underlying bedrock and increasingly thicker coatings intensify this contrast reduction until no spectral information of the bedrock is detectable. Prior laboratory studies also show that for different mixtures of a material with various grain sizes, the fine particles will dominate the thermal conductivity and therefore affect the TI values to a greater degree (Mellon et al., 2014). Because the diurnal brightness temperature response of bedrock is significantly influenced by a thin coating of dust (Putzig and Mellon, 2007), identifying the amount and location of that dust is beneficial to determine areas of exposed (or minimally mantled) lava flow surfaces. Mars Orbiter Camera (MOC) analysis of wind streaks in Daedalia Planum by Edgett and Malin (2000) show the presence of a thin cover of fine-grained sand in some areas rather than an extensively thick dust deposit. This suggests that the mantling by dust may not be uniform spatially. Therefore, it should be possible to

identify the general distribution and possible locations of minimal to no dust cover on the flow surfaces, sites that ultimately could be targets of subsequent spectral/compositional analysis.

#### **4.2.4 Mixed Surfaces**

Although TI is a valuable tool, various complex surfaces and instrument limitations arise, which can hinder thermophysical studies (Fergason et al., 2006). For example, analysis must take into account compositional and particle size mixing (horizontal/checkerboard mixing) and/or mantling (vertical layering) at scales below the spatial resolution (pixel size) of the instrument. With limited in situ observations (especially at sites similar to this study location), the material properties within a single pixel (e.g., ~100m for THEMIS, Christensen et al., 2004) are commonly assumed to be uniform. This assumption, coupled with the dust cover previously defined by TES data, lead to the consideration that Daedalia Planum is too dusty for thermal IR spectral studies. However, these data are composites of complex mixtures of surficial units with possible horizontal mixing and vertical layering, some with drastically different thermal responses such as dust and bedrock.

Certain lower thermal inertia areas may be explained by small-scale horizontal mixtures and/or vertical layering of coarse and fine grained material. Therefore, previous spectral analysis at the 3 km spatial scale of TES could very well overestimate the amount of dust and overlook any small-scale surface variability. At the higher spatial resolution of THEMIS, the ability to detect these smaller-scale variations becomes possible. Additionally, recent studies have begun to examine subpixel temperature variations on pit craters and sinuous rilles on Arsia Mons (e.g., Lopez et al., 2012). If larger/blockier portions of these lava flows rise above the low-lying regions filled with sand, a horizontal (linear) mixing scenario arises. Furthermore, if these lava

blocks have minimal dust coverage, the data will represent a linear mixing scenario between lava outcrops and sand with minor/variable scales of vertical layering on certain flows. Here, we examine THEMIS-derived thermal properties in detail to identify possible locations of these rocky surfaces.

#### **4.2.5 Previous Work**

Crown and Ramsey (2017) examined the rugged and smooth flow types in the northeast Daedalia Planum flow field to determine the applicability of IR data for compositional analysis. Using a combination of image processing techniques and geomorphic analysis, subtle spectral variations were identified (Ramsey and Crown, 2010; Crown and Ramsey, 2017). With nearly complete coverage by CTX images, these data were used by Crown and Ramsey (2017) to classify the flows into two categories, smooth or rough. Flows with a smooth surface morphology are defined as having lower albedo, being less defined and similar in morphology to terrestrial pahoehoe flows. Conversely, rugged flows (similar to a'a morphology) have a higher albedo with an irregular surface morphology containing flow ridges, prominent channels, and levees. These flows display locally high standing, bright, rugged outcrops of lava with transverse eolian ridges and sand visible in the adjacent low-lying regions. Nearly half of the area of these flows was identified as having the rough surface morphology.

The work by Ramsey and Crown (2010) and later Crown and Ramsey (2017) also identified the presence of unusual thermophysical variability. They concluded that the thermal emission from these flow surfaces was the result of a complex interplay between surface roughness, albedo, dust mantling, and the underlying lava composition. However, the specific relationship between these components remained unresolved. With this preliminary information

and the geologic mapping completed by Crown et al. (2015), this study uses multiple datasets and more detailed thermal IR analysis to determine the thermophysical variability at the individual flow scale.

## **4.3 Methods**

### **4.3.1 Datasets**

An integral part of the project is using multiple spatial and spectral resolution datasets: 1) Mars Reconnaissance Orbiter ConTeXt Camera (CTX) and High Resolution Imaging Science Experiment (HiRISE) images, 2) Mars Odyssey Thermal Emission Imaging System (THEMIS) IR and TI images, and 3) Mars Global Surveyor Thermal Emission Spectrometer (TES) data (Table 7; Figure 27). The benefits and limitations of each relate to the spatial/spectral resolution and/or the areal coverage. HiRISE data, with the highest spatial resolution, provide the most detail but with limited coverage. These data are used for specific detailed observations of surface morphology, with CTX data providing complete coverage at a slightly lower spatial resolution. THEMIS data have a lower spatial resolution than the visible instruments, but span the visible and thermal infrared regions, providing both compositional and surface morphology information.



**Table 7. Summary description of datasets, including any instrument limitations, used to conduct this study. (<sup>a</sup>Malin et al., 2007; <sup>b</sup>McEwen et al., 2007; <sup>c</sup>Christensen et al., 2004; <sup>d</sup>Ferguson et al., 2006; <sup>e</sup>Ruff and Christensen, 2002).**

Dataset		Resolution (m/Pixel)	Spectra (μm)	# of Stamps	Usage
MRO ConTeXT Camera (CTX) <sup>a</sup>	VIS	6	0.5-0.8	184	Identify lava flow boundaries and surface morphology
MRO High Resolution Imaging Science Experiment (HiRISE) <sup>b</sup>	VIS	0.30	0.4-1	40	
Mars Odyssey Thermal Emission Imaging System (THEMIS) <sup>c</sup>	VIS	18	0.425-0.86	8	Identify variation in albedo
	TIR	100	6.78-14.88	121	Identify thermophysical variation in the lava flow field
THEMIS derived Thermal Inertia (TI) <sup>d</sup>	TIR	100		70	Identify particle size on surface
Thermal Emission Spectrometer (TES) Dust Cover Index (DCI) <sup>e</sup>	TIR	3000	6-50 (TES)	Map	Measures the presence of spectrally-obscuring surface dust

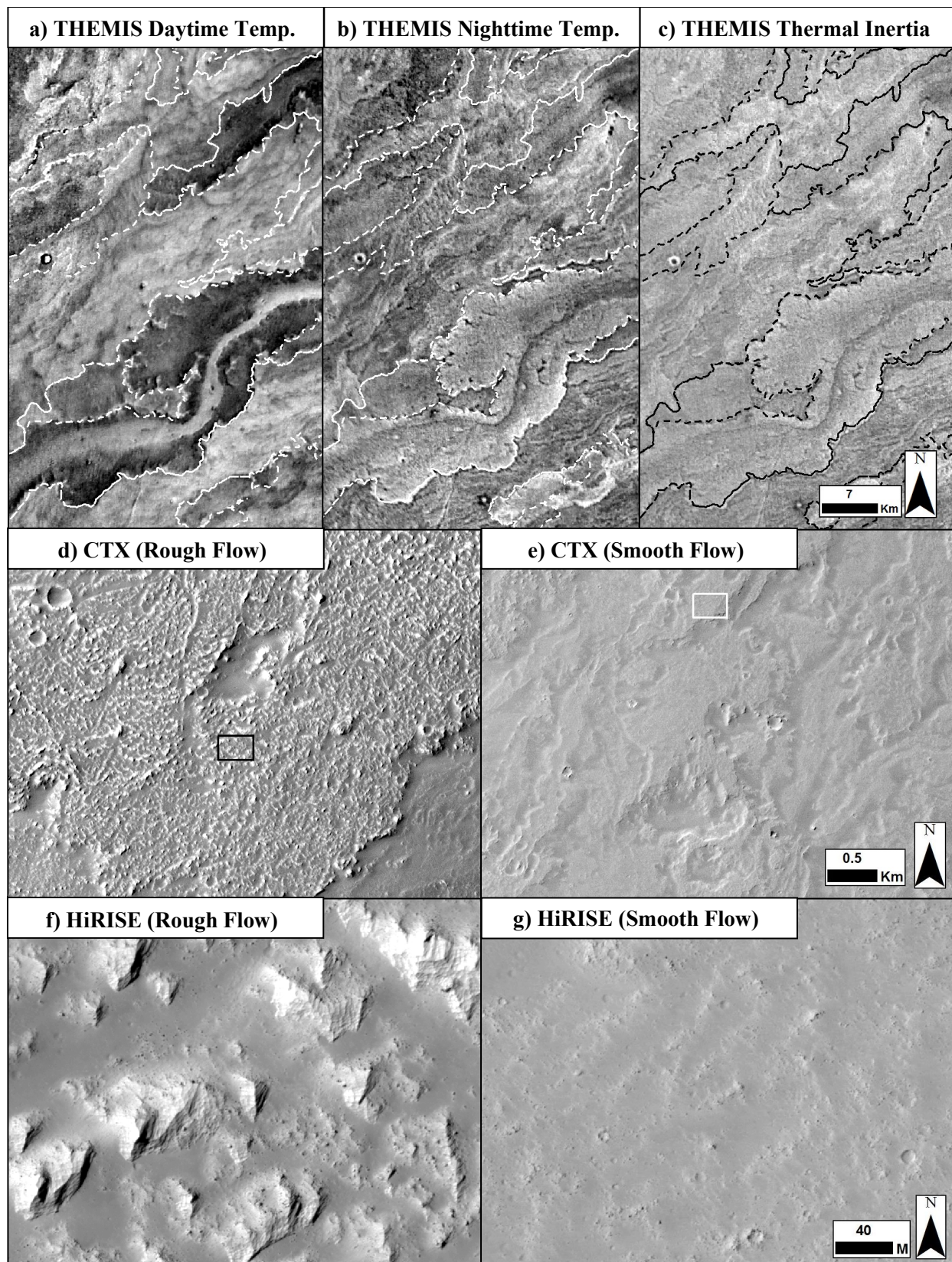


**Figure 27. The lava flows in Daedalia Planum shown at various spatial scales: (a) daytime brightness temperature mosaic (Edwards et al., 2011) with the flow boundaries (white, dashed) of Crown et al. (2015), (b) nighttime brightness temperature mosaic (Edwards et al., 2011), and (c) thermal inertia (Ferguson et al., 2006) showing the thermophysical variations (the center of this region is shown as the yellow dot in Figure 26). CTX images of representative (d) rough (P01\_001590\_1567) and (e) smooth (P18\_008038\_1544) surface morphologies (black and white boxes respectively indicate the areas shown in (f) and (g)). Representative HiRISE images showing the (f) rough (ESP\_036731\_1570) and (g) smooth (ESP\_036586\_1560) morphologies.**

#### **4.3.2 Decorrelation Stretch**

To determine if thermophysical variations in the thermal IR data are due to compositional differences between the flows versus mantling of optically-thick dust, a decorrelation stretch (DCS) of the THEMIS data is performed using the standard band combinations (6-4-2, 8-7-5, 9-6-4), following the methodology of Hamilton et al. (2007) (Figure 28). If the flow surfaces contained different compositions, distinct color patterns would appear in these band combinations specifically correlating to surface features.



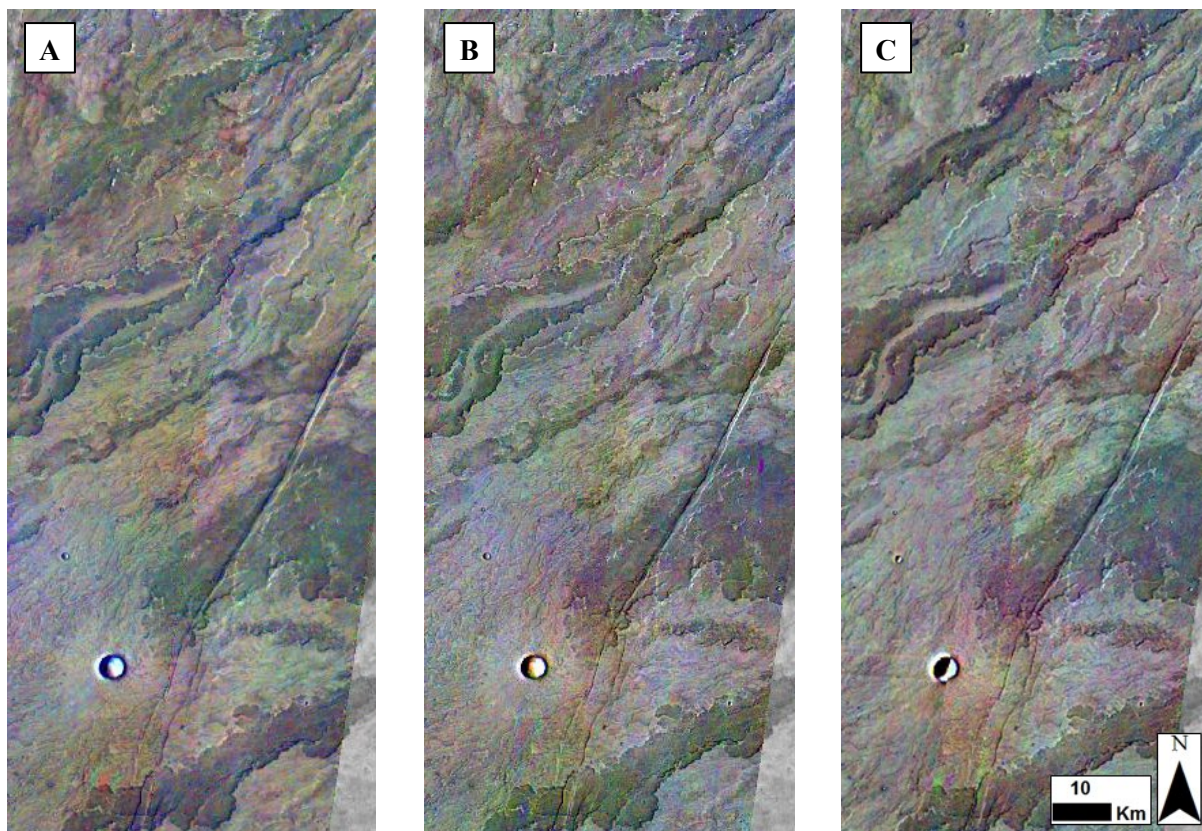


**Figure 28.** THEMIS IR decorrelation stretch (DCS) of a mosaic of stamps I52299002, I51737003, and I50713002 using bands (a) 6-4-2, (b) 8-7-5, and (c) 9-6-4. The minor color variations (and the consistency of color between the images) indicates that significant compositional variability is likely not present.

### 4.3.3 Geomorphologic Analysis

To examine the observed thermophysical diversity in this region, 43 lava flows ranging in length from ~6 to 170 km are analyzed (Figure 28a-c). These well-defined flows include both the smooth (11 flows) and rough (32 flows) surface morphologies of Crown and Ramsey (2017). CTX and HiRISE data are used to investigate the detailed flow morphology, boundaries, and surface roughness. Only small portions of 20 flows are analyzed at HiRISE resolution due to the limited coverage. CTX data serve as the primary source to examine all the flows for the surface

morphology, identify the degree of visible mantling (noting any obvious portions of the flows that appear minimally-mantled or not mantled) and estimate the potential of horizontal mixing. For this study, three main surface units are defined (dust, sand, and lava outcrop) with the assumption that Daedalia Planum is dominantly basaltic (Giacomini et al., 2012; Lang et al., 2009). Following definitions established by Putzig and Mellon (2007), these units are chosen based on natural layering systems found in terrestrial analogs and Mars observations. The degree of vertical layering is estimated by identifying the coverage of locally high standing, high albedo, rugged outcrops of lava, transverse eolian ridges, and sand.

#### **4.3.4 Thermophysical Analysis**

To understand the thermophysical variation across the flow field, specific limitations are placed on the THEMIS IR data search (Simurda et al., 2016). THEMIS daytime and nighttime IR data are selected based on the following criteria: (1) all IR bands (1-10) are acquired, (2) data are collected between 15:00-18:00 (day) and 2:00-6:00 (night) local time, and (3) surface temperatures between 225-350 K are present in the daytime data. Selecting for all the IR bands allows discrimination based on possible compositional variations. The chosen local time captures the peak variation in thermophysical responses, which improves differentiation between fine-grained material and rock. Specifically, these time periods capture the greatest thermal difference between the rock, sand, and dust. The daytime data temperature requirement minimizes noise to ensure the maximum discrimination in the thermophysical response. Data that meet all constraints are then atmospherically corrected using the approach of Bandfield et al. (2004), spatially registered and processed to radiance and brightness temperature values (Christensen et al., 2004). Data are assessed for quality and any oversaturation or instrument anomalies are

removed. The projected brightness temperature (PBT) data are used in this study to assess the daytime and nighttime thermophysical variation within the flow field (see Figure 2a-c) and for direct comparison to TI values derived from THEMIS IR nighttime data (Christensen et al., 2001; Fergason et al., 2006). All THEMIS data are cropped to the study area boundaries.

#### **4.3.5 Regions of Interest**

More than 1250 regions of interest (ROIs), each with an area of 500m x 500m (25 THEMIS pixels), are defined to avoid sampling bias within individual flows and to quantify the variability of TI and brightness temperature within and between individual flows (Figure 29). Using both CTX and HiRISE data, each ROI is carefully placed at 3-4 km intervals apart and contains a single lava flow surface, either rough or smooth. All flow edges, levees/channels, and impact craters on the flows are avoided as they may have different surface properties. Flow edges will contain shadowing throughout the day, for example, that limits the maximum temperature reached by the surface material, resulting in an inaccurate representation of the thermal response. Additionally, depending on the observation time and solar incidence angle, shadowed flow edges have a lower albedo in visible data. During flow emplacement, channels, where present, would have continued to feed erupted material down flow. Thus, material on the non-channelized portion of the flow and adjacent material in the levees and channels will have different emplacement times and conditions. Furthermore, shadows may also affect the thermal response of the levees and channels. Craters and any significant ejecta could have a different thermal signature compared with the target material, either exposing deeper material or scattering surface material.

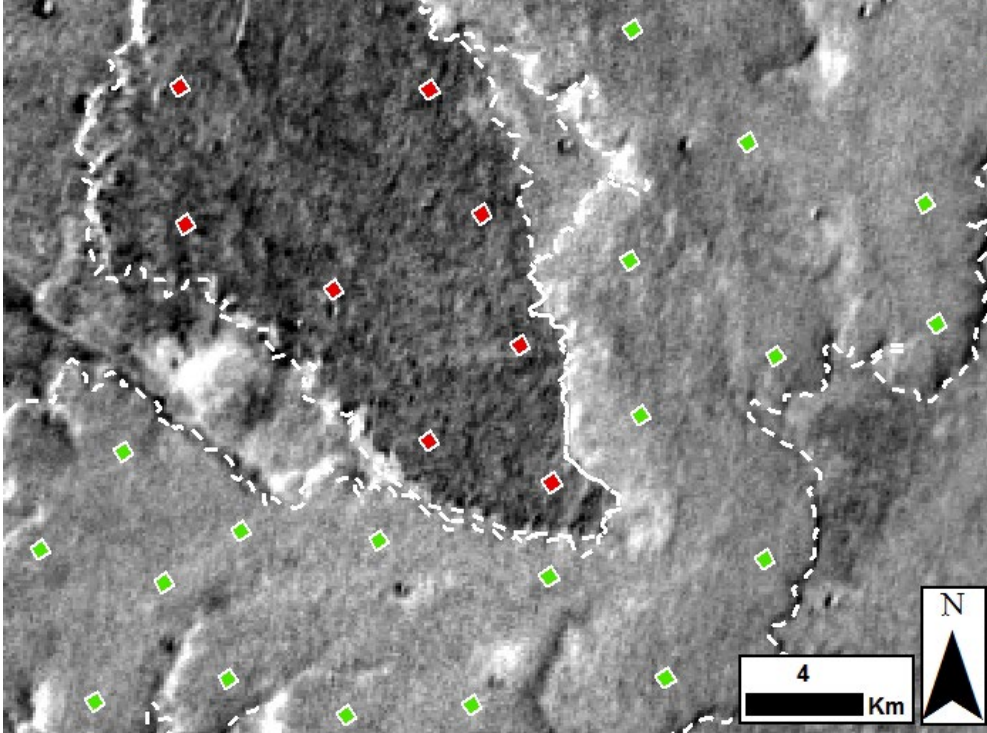


**Figure 29. Representative ROI distribution (category colors defined in Table 8) overlain on the daytime brightness temperature mosaic (from Edwards et al., 2011) with flow boundaries in white (dashed) by Crown et al. (2015). Location within the study area designated by the white arrow in Figure 31.**

A complete statistical analysis of the THEMIS temperature and TI data sampled by the ROIs within the study area is performed, including the mean and standard deviation. A look-up table contains the variation between the pixels in each ROI and the variation between flows. Analysis of Variance (ANOVA), a statistical test used to determine the degree of variation between identified groups (Sheskin, 2011), is also conducted on these data. This allows for an assessment of the variance between the flows and the determination of whether multiple thermophysical responses are present. In order to compare the responses between flows, two simple calculations are performed for the temperature and TI data: (1) the average of each ROI mean for an individual flow and (2) the difference between the average for each individual flow

and that of the average for the THEMIS stamp within the study area boundaries. The goal is to determine the response of each flow in comparison to the flow field.

#### **4.3.6 Defined Categories**

The results of the statistical analysis defined four flow categories based on daytime and nighttime THEMIS IR brightness temperature data relative to the study area mean. These classes depict the diurnal temperature response differences between the flows and show the potential variation in surface materials. To define these categories, the average values of all the ROIs for each flow is compared with the average value of the study area to determine whether the response was high or low. The four categories (labeled A-D) are identified based whether the flow displayed a high or low (i.e., warm or cold) daytime and nighttime temperature response (Table 8; Appendix C). The difference between each ROI mean and the flow area mean ( $\Delta T$  and  $\Delta TI$ ) is also calculated to compare the variation between the stamps and identify any changes along the flow length. Finally, the THEMIS defined category, brightness temperature values, TI values, surface texture, and flow morphology (as defined by Crown et al., 2015) are compared for each flow. This allows us to identify the correlation between the thermophysical response and surface features.



**Table 8.** The thermophysical response of the four flow categories based on daytime and nighttime brightness temperature differences. The assigned color of each category correlates to Figures 4 and 6.

<b>Category</b>	<b>IR Daytime Temperature</b>	<b>IR Nighttime Temperature</b>	<b>Thermal Inertia</b>
<b>A</b>	High	High	
<b>B</b>	High	Low	Low
<b>C</b>	Low	High	High
<b>D</b>	Low	Low	

#### 4.4 Results

In agreement with the previous work, no major compositional differences are easily identified in the DCS products (Figure 28). Because a major compositional difference is not apparent and the age estimates from crater counts reveal a relatively small range in ages (Berman and Crown, 2019), the variation in thermophysical response is most likely due to material properties of the surface, specifically the distribution of dust, sand, lava outcrops coupled with albedo. If the area was completely covered with an optically thick layer of dust, the brightness temperature and TI should vary based only on local topography, which creates shadowing and limits the maximum surface temperature. In this scenario, the greatest variation should only occur on the flow margins, which is not the case. In fact, neighboring flows demonstrate easily seen variations (Figure 27a-c).

#### 4.4.1 Thermal Inertia of the Flow Field

Generally, for material with the same composition, the finer grain sizes will have very low thermal inertia units (tiu) of  $\sim 56$ , whereas sand will have intermediate values ( $\sim 223$  tiu), and larger rocks, or rocky surfaces, will have values as high as  $\sim 2500$  tiu (Putzig and Mellon, 2007). If the surface properties are uniform at the pixel scale, the THEMIS derived brightness temperatures are expected to have a greater variation over a day for low TI materials (e.g., high daytime and a low nighttime brightness temperatures). High TI surfaces would display a low daytime and high nighttime brightness temperature with a more limited variation in temperature over a day. However, the TI in Daedalia Planum does not change dramatically and displays a more subdued variation, ranging from 170 to 332 tiu with a maximum  $\Delta TI \sim 55$  tiu. These TI values are indicative of intermediate particle sizes, which likely means that the dust cover is heterogeneous and less than the optical thickness. Moreover, CTX and HiRISE images show distinct surface variations and the presence of horizontal mixing and vertical layering scenarios. The TI values on this flow field may not represent the true complexity of the surface, however. The limited range of values may be the result of using only THEMIS nighttime data to derive TI values, which would not depict the full extent of the thermal response. In fact, even though the flows display moderate TI values, there are numerous combinations of vertical layering and horizontal mixing of dust, sand, and lava that could produce these values. Therefore, understanding the thermal response over the diurnal cycle may reveal more nuanced differences requiring further analysis.

#### **4.4.2 Unique Diurnal Signatures of the Flow Field**

To assess the diurnal responses of the flows, the  $\Delta T$  variation was first investigated. This analysis showed that different diurnal responses do exist between flows with four unique types of responses. The maximum variation in  $\Delta T$  of individual flows is  $\sim 5$  K, with some being less than the THEMIS uncertainty of 2 K. These changes in temperature show that the variance between flows is not due to instrument noise and that, in general, the flow field is not completely covered by dust. It is more probable that the data are detecting different proportions of lava outcrop and eolian infilling of sand, all of which are mantled to some degree by dust. This suggests that flow surfaces with low daytime and high nighttime brightness temperatures that also have a high TI should have the greatest exposure of lava outcrops.

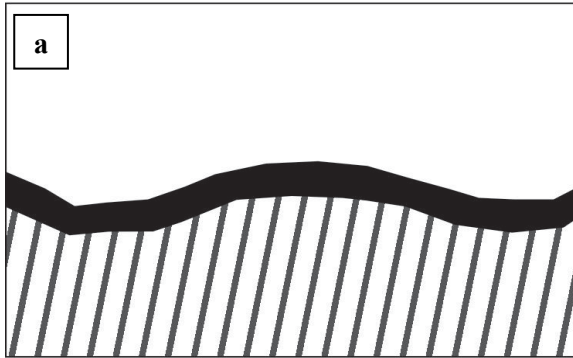
#### **4.4.3 Thermal Response of Categories B and C Flows**

Two dominant trends in THEMIS brightness temperature data are present (Table 8), representing the likely thermophysical endmembers of this flow field. Category B flows, with high daytime and low nighttime brightness temperatures, display a lower TI value and are therefore presumed to be surfaces with the greatest amount of dust coverage. Category B flows show the greatest variation in temperature over the diurnal cycle and the highest heating and cooling rates, all indicative of a finer particle size dominated surface. Whereas category C flows, with the inverse temperature relationship, have higher TI values and the least variation over the diurnal cycle with the lowest heating and cooling rates. These are indicative of a surface with comparatively greater amount of higher thermal inertia material. The ability to separate the flows into these categories demonstrates that the areal percentages of lava outcrops and sand in low-

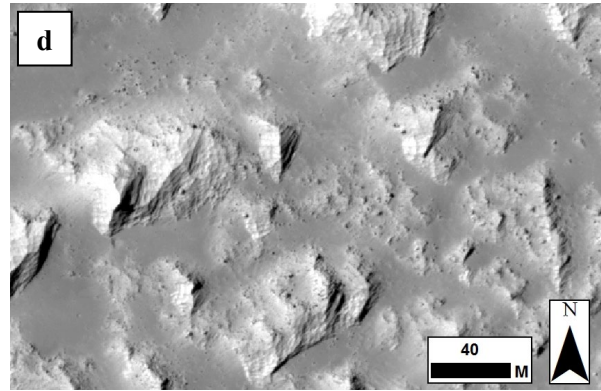
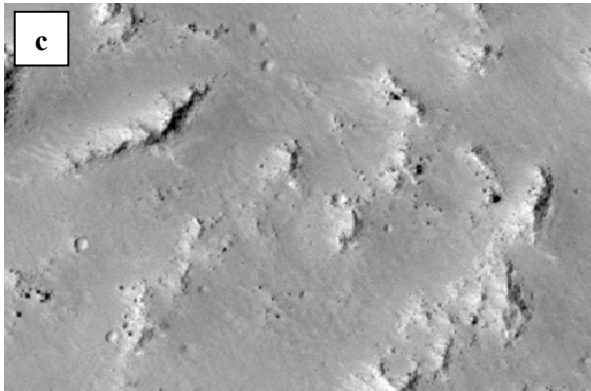
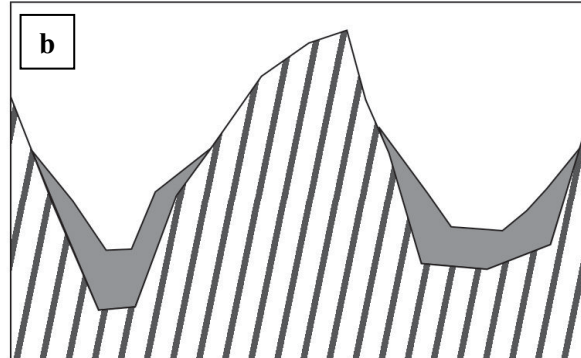
lying areas are significantly different on some of the flows. For example, a pixel on a category B flow would be dominated by sand, minor amounts of rocky outcrops and covered with appreciable dust (Figure 30c). A pixel on a category C flow will have a higher areal distribution of lava outcrops than sand in low-lying regions and quite possibly less dust (Figure 30d).

# Simple Scenarios

## Vertical Layering

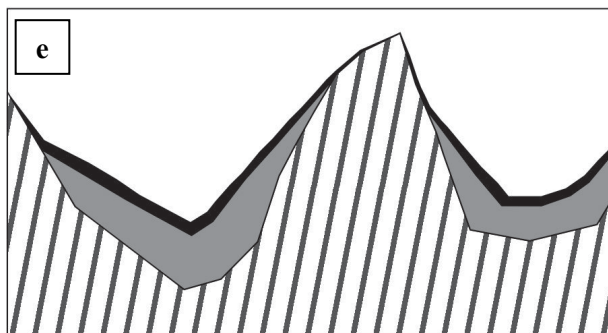


## Horizontal Mixing

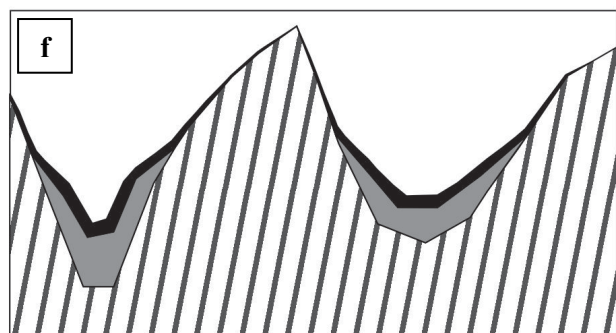


# Complex Mixing and Layering Scenarios

## Category B



## Category C



■ Dust    ■ Sand    ▨ Lava Outcrop

**Figure 30. Possible idealized configurations (a, b, e, f) of surficial deposits covering lava outcrops in the Daedalia Planum study site. Simple configurations are shown of (a) a vertically layered system with dust uniformly covering the lava flow, and (b) a horizontally mixed system with sand deposited in low-lying regions and the lava flow surface free of dust. HiRISE images displayed at the same scale showing rough flow surfaces that correspond to (c) category B (ESP\_046450\_1535) and (d) category C (ESP\_041940\_1570) thermophysical responses. More complex scenarios showing both horizontal mixing and vertical layering with sand deposited in low-lying regions for (e) category B rough flows with a greater areal coverage of sand and/dust and (f) category C rough flows with the greatest abundance of exposed lava outcrops.**

#### **4.4.4 Thermal Response of Categories A and D Flows**

The two remaining categories, A and D, likely represent a more specific distribution of horizontal mixing and vertical layering scenarios (Table 8; Figure 31). Eleven flows have unchanging daytime and nighttime temperature response relative to the flow field (either staying comparatively low or high throughout the diurnal cycle). This thermophysical response is likely due to the presence of very specific amounts of horizontal mixing and vertical layering of dust, sand, and lava outcrops on the surface. Of these eleven flows, only one falls into A with a consistently higher brightness temperature throughout the diurnal cycle, however within the THEMIS instrument error. This category was not further examined because of limited statistics. Category D flows have consistently lower brightness temperatures throughout the day. These flows display a daytime temperature response of a complex surface containing a high areal percentage of larger block sizes (lava outcrops) compared to the flow field to limit the maximum daytime temperature, but with enough finer particles (either dust or sand) to lower the surface temperature at night. This suggests that there is a comparatively higher percentage of lava outcrops than sand and dust, but less than those surfaces with a category C response.



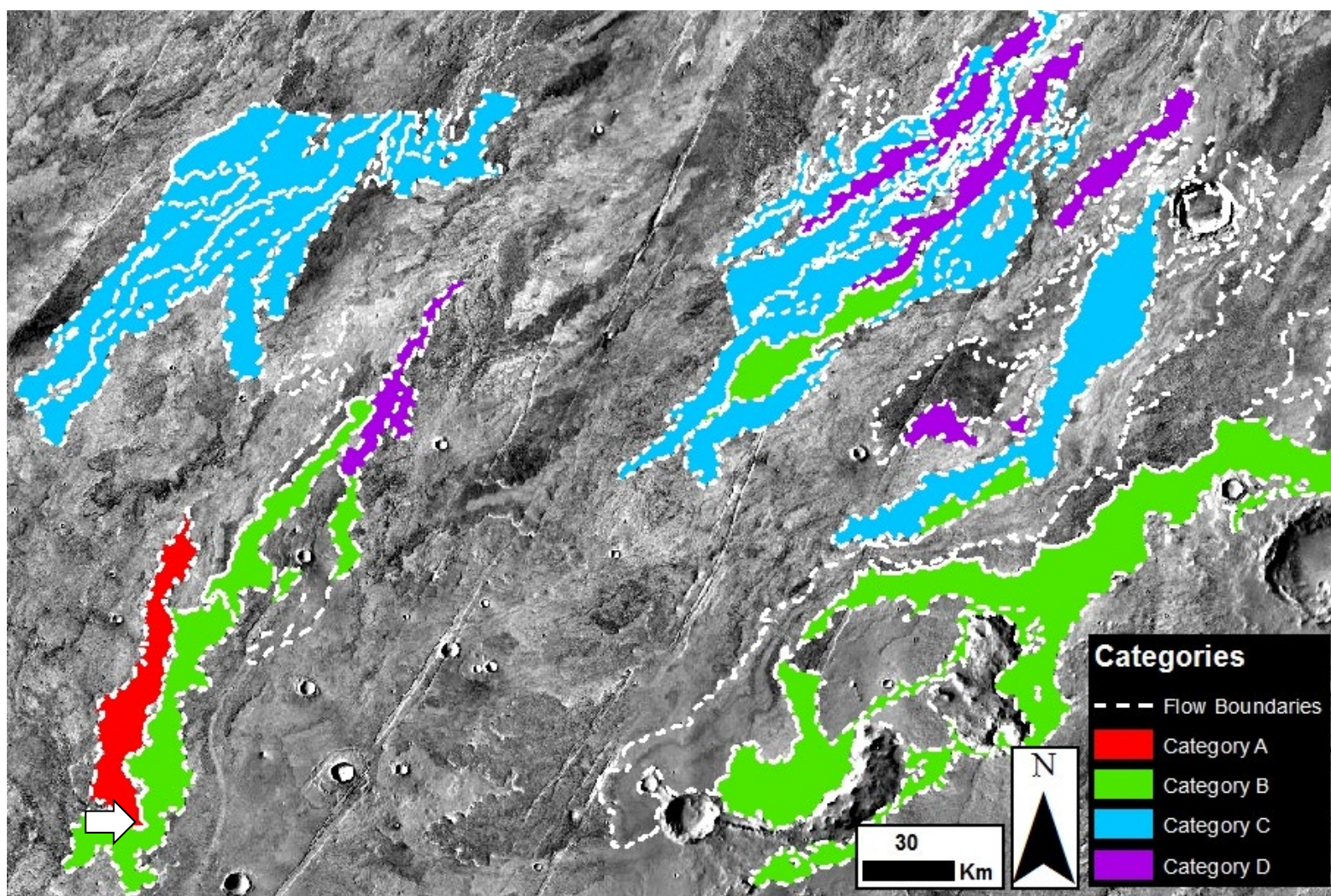


Figure 31. THEMIS nighttime brightness temperature mosaic (from Edwards et al., 2011) of the Daedalia Planum study area showing the categorized flows (bounding coordinates: longitude 120.4-127.5° W and latitude 22.0-26.8° S). The Crown et al. (2015) flow boundaries are shown with white dashed lines and the flow colors correspond to the thermophysical response categories (Table 8). The white arrow marks the location of Figure 29.

#### 4.4.5 Latitude Distribution

The distribution of flow categories also hints at a possible latitude dependence (Figure 31). Category A and B flows predominantly appear in the southern half of the study area, whereas category C and D flows occur in the northern half. The TES-derived DCI only changes slightly between 0.95 to 0.97 within the study area and the general elevation changes from ~4400 m in the northeast to ~2750 m in the southwest. Even though there is a significant elevation change over the study area, the maximum elevation change within a given THEMIS stamp is only 850 m over a distance of ~310,000 m producing local slopes below 0.5 degrees. Thus, elevation differences between flows are not statistically significant to affect the categorization of the flows or cause this possible latitude dependence. Recalling the previous discussion of the relationship between TI and brightness temperature responses, the latitude distribution may suggest that flows further north have a higher concentration of exposed lava outcrops. This is further supported by the presence of the single category A flow in the more southern region and category D flows in the northern portion. This distribution may suggest the presence of slightly different eolian surface processes occurring from north to south, perhaps affected by the larger Arsia Mons topography.



**Table 9. Statistical summary of the correlation between surface morphology and thermophysical response. Smooth flows predominantly display a category B or C response with inverse day and night delta brightness temperatures ( $\pm\Delta T$ ; see section 4.3.5 for explanation) in relation to the flow field as a whole, whereas rough flows principally have category C or D responses.**

Category	IR Day Temp.	IR Night Temp.	Total # of Flows	Total % of Flows	# of Smooth Flows	and % of Smooth Flows	# of Rough Flows	and % of Rough Flows
A	High	High	1	2.3%	0	0.0%	1	3.1%
B	High	Low	7	16.3%	4	36.4%	3	9.4%
C	Low	High	25	58.1%	6	54.5%	19	59.4%
D	Low	Low	10	23.3%	1	9. %	9	28.1%

#### 4.4.6 Correlation Between Thermal Response and Surface Morphology

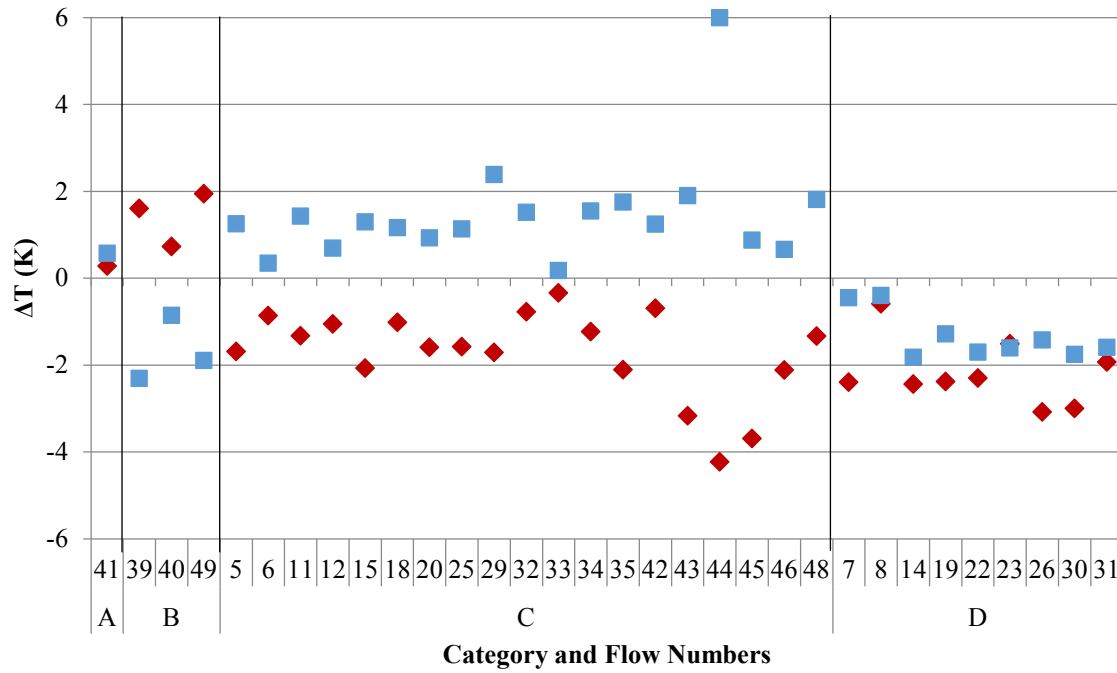
The correlation between the four thermophysical categories and the rough/smooth surface morphology demonstrates that flow surface structure likely influences the distribution of dust, sand and lava outcrops (Table 9; Figure 32a-b). A slight majority (58%) of all flows, both rough and smooth, have a category C thermal signature. This suggests that enough lava outcrops are exposed and/or minimally mantled to produce a limited diurnal temperature response. Lava flows outcrops with limited sand/dust mantling would display lower daytime and higher nighttime brightness temperatures, whereas flows covered with a thick layer of dust would display a classic high daytime and low nighttime temperature diurnal cycle. Smooth elongated flows are dominantly either category B or C (combined over 90%) with a greater percentage of the smooth flows being category B compared to that of rough flows. This suggests that these flows are more likely to have greater amounts of dust and/or sand (Table 9). A percentage of the smooth flows do demonstrate a thermophysical response more indicative of a higher lava outcrop concentration (category C). However, the interpretation of their surfaces in the high resolution

data is more problematic with far less surface diversity than the rough flows. It may be the case where the mixing of dust and underlying rock is simply below the scale of even HiRISE data (Figure 27f-g).

Over 87% of rough surface flows are either category C or D, with lower daytime brightness temperatures (Table 8). Of these flows, over 59% are category C (low daytime and high nighttime brightness temperatures) with slightly higher thermal inertia values (Figure 32a). Based on CTX and HiRISE analysis of these surfaces, category C rough lava flows are the most likely to resemble a'a flows and contain a significant amount of exposed lava outcrops (Figure 30f). The visible data also show eolian forms such as ripples in the low-lying areas (Figure 27f). One possible explanation for why rough flows display thermal signatures indicative of higher concentration of lava outcrops centers on the wind interaction with the different surface morphologies. As seen in HiRISE data (Figure 27f), the lava outcrops on rough flows are visibly higher and have ventifact-appearing facets. These outcrops, therefore, may be eroding preferentially, creating localized areas preferentially swept clean of dust. The smooth flows lack large surface topography that would promote this process, thus allowing dust to accumulate.

a

## Rough Surfaces



b

## Smooth Surfaces

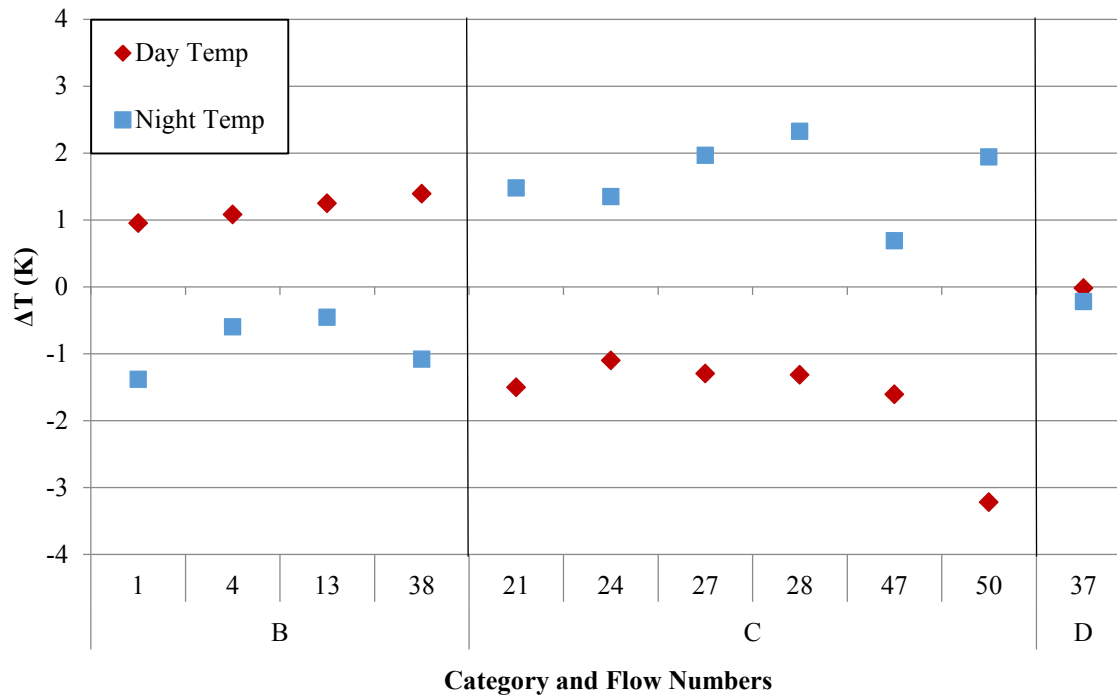


**Figure 32. Delta brightness temperature ( $\Delta T$ ) values shown for each flow, grouped by flow category and surface morphology. These delta values were computed by calculating the difference between the average value for the THEMIS stamp and average value for each flow in order to compare values between stamps with different observation parameters (see section 4.3.5 for explanation; Christensen et al., 2004). Data were further separated between (a) rough and (b) smooth surface morphologies.**

Thus, the results of this visible and thermophysical study provide clues about the non-uniform subpixel surface characteristics of the Daedalia Planum flow field southwest of Aria Mons by identifying flows with a greater amount of exposed lava outcrops (Category C) or finer-grained sand sized particles (Category B) comparatively. The thermophysical variation between these flows is linked foremost to the overprinting of different areal proportions of dust, sand, and lava outcrops, which appear to be related to (if not driven by) the flow morphology (rough vs. smooth). The confirmation of a greater amount of exposed lava on certain flows, detectable from orbital visible and IR datasets is important for future studies aimed at unraveling this subpixel mixing and more importantly, focused on compositional and volcanological analyses.

## **4.5 Conclusions**

The surface thermophysical properties and flow morphology reveal that individual flows in Daedalia Planum respond differently to diurnal heating, suggesting that the area is not completely (or uniformly) mantled by dust as previously assumed. Interestingly, this diversity in post-emplacement eolian activity is not simply a function of age (Crown et al., 2015; Berman and Crown, 2019). Decorrelation and the limited spectral analysis of the thermal IR data suggest that there is no significant compositional difference that would cause these thermophysical

variations, nor does assuming that this is a dusty region on Mars. In order to further examine and quantify this variability, the diurnal temperature and TI responses of individual flows were evaluated in relation to the mean of the study area. The goal was to determine the cause of the unusual thermophysical variability seen in this region. The conclusion, described below, is that it is a complex relationship between the flow surface morphology and the vertical layering and/or horizontal mixing of dust, sand, and lava outcrops. Certain flows and areas within flows appear to have significantly higher amounts of lava outcrops, which will be targeted for further investigation.

Most flows demonstrate an expected inverse diurnal temperature response resulting in two distinct diurnal curves (Table 9). Flows with a higher daytime and lower nighttime temperature (category B) have lower TI values indicating that these surfaces have the largest range of temperature variability over a day and have faster rates of heating and cooling. These flows either have a higher concentration of sand on the surface with a minor presence of lava outcrops and dust or a significantly thicker dust coverage compared to neighboring flows. With the inverse diurnal temperature response, category C flows with higher TI values have the most limited range of diurnal temperature variation and the slowest rate of heating and cooling. These flows contain a visibly greater areal distribution of lava outcrops with sand in low-lying regions and some level of nonhomogeneous dust coverage. Ripples are also seen in the low-lying regions of these rough flows in HiRISE images. Analysis of surface morphology in both visible and thermal infrared data demonstrates that rough flows with a category C response contain the highest concentration of identifiable lava outcrops.

The subpixel surface horizontal mixing and vertical layering of thermophysical units is detected in higher spatial resolution orbital thermal IR datasets and may be seen in other regions

on Mars with similar eolian mantling. This work successfully quantified the small-scale thermophysical properties of individual lava flows in Daedalia Planum, developed an approach to understand the thermophysical units responsible, and identified the surfaces with the greatest amount of exposed lava outcrops. This was completed in an area previously overlooked for any thermal IR analysis because of the TES-derived albedo and a dust cover index values. Importantly, a likely significant areal percentage of lava outcrops are present on the surface of some of these flows suggesting the presence of particular eolian surface process that interacts with the surface topography of the rough flows, keeping them relatively dust free. Work is ongoing to quantify the areal percentages of the thermophysical units and complete a more detailed spectral analysis of the flow areas with more outcrops present. Those results could constrain any down-flow spectral changes or differences between flows, which would lead to a better understanding of the compositional and rheological properties of individual flow emplacement in this complex and interesting flow field on Mars.

#### **4.6 Acknowledgements**

This research was supported through continuing funding of an original Mars Odyssey Participating Scientist Program project (NMO710630) to the second author, as well as a recent NASA Earth and Space Science Fellowship awarded to the first author (80NSSC17K0460). All data discussed in this paper are available in the cited references. THEMIS data are publicly available at the ASU Mars Image Explorer (<https://viewer.mars.asu.edu>) and CTX and HiRISE data are publically available from the NASA Planetary Data System (<https://pds.nasa.gov>). The author would also like to acknowledge the seminal work of the late Josh Bandfield on both the

THEMIS data calibration and modeling of RMS surface roughness on Mars. His planetary intellect and insights will be missed.

## **5.0 Quantifying the Vertical Layering and Horizontal Mixing of Dust, Sand, and Lava Outcrops on Lava Flow Surfaces in Daedalia Planum, Mars**

### **5.1 Introduction**

Analyses of lava flows in Daedalia Planum, Mars using THEMIS infrared (IR) data suggest minor compositional variability may be detectable despite the high-albedo and high-dust cover index in the region (Ramsey et al., 2016). However, to investigate these potential compositional variations, the spectral and thermophysical signatures of the possible exposed lava outcrops must be separated from the signature(s) of dust and sand covering the flows. Thermal infrared data can be used to derive the particle sizes on the surface due to the high dependence of thermal conductivity on this material property, but the individual components of complex surfaces with both horizontal mixing and vertical layering are difficult to separate. Modeled thermal conductivity measurements under Martian conditions suggest that low thermal inertia (TI) regions, such as Daedalia Planum, may be explained by a mixture of coarse plus fine-grained material (Presley et al., 1997; Mellon et al., 2014). For lava flows, such a mixture could therefore consist of larger lava outcrops with sand in low-lying regions and potentially an optically thin, spatially heterogeneous layer of dust. With the collection of higher spatial and spectral resolution data, these complex surfaces can begin to be investigated in greater detail.

With the analysis of thermophysical properties of these lava flows in the previous chapter, those with a rough surface and low daytime and high nighttime temperature response were determined to be the most likely to have the highest percentage of identifiable lava outcrops. If the actual amount of identifiable lava outcrops on the surface can be identified as



well as the amount of any vertical layering from dust or horizontal mixing with sand, these specific areas can be targeted for further compositional analysis. Recent studies have attempted to identify the layer of dust on the surface on Mars, but these models utilize a low spatial resolution instrument (TES at 3 Km) and do not take into account any horizontal mixing with the pooling of sand in low-lying areas of the flow surface (Putzig and Mellon, 2007; Ruff and Christensen, 2002). These flow surfaces can now be targeted using modeling and remote sensing methods to quantify the amount of dust, sand, and lava outcrops in form of both horizontal mixing and vertical layering.

This research seeks to apply aspects of those prior studies coupled with new analysis approaches to determine the areal percentages of dust, sand, and lava outcrops on the surface of the lava flows in Daedalia Planum, Mars. Furthermore, this study hypothesizes that these flows may have localized regions of minimal dust and mixtures of rock plus sand that can be identified in the thermal IR data. This work seeks to: 1) identify a method by which the diurnal temperatures and thermal inertia of complex surfaces of dust, sand, and lava outcrops can be modeled, 2) identify the presence of layered and horizontal mixing scenarios, and 3) quantify the presence of dust, sand, and lava outcrops exposed on the surface of the lava flows.

## **5.2 Background**

### **5.2.1 Geologic Setting: Daedalia Planum**

The previous chapter (section 4.2.1) provides a thorough background of Daedalia Planum and the lava flows within this region. Daedalia Planum contains one of the main flow aprons, of

predominantly basaltic composition, originating from the SW flank of Arsia Mons (Crumpler et al., 1996; Lang et al., 2009; Edwards et al., 2011). The study area was selected for its coverage by multiple datasets, extensive lava flow fields, containing some of the youngest lava flows on Mars, and previous flow field mapping (Crown and Ramsey, 2016). Recent thermal investigations of this area revealed unique thermal variation between the flows that are not caused by composition or age differences. Neighboring lava flows display thermal diurnal responses that are distinct from each other and vary across the flow field.

The extent of the TI and brightness temperature variations suggests the presence of different roughness distributions or linear mixing of mantling and lava outcrops. If only a thick dust covering was present, any variation in the TIR data would be the result of shadowing effects based on sloped topography, which limits the peak temperature reached by fine material. Over 53% of rough flows have low day and high night brightness temperatures (Table 8, category C), producing higher TI values. These flows are the most likely to have horizontal mixing with larger outcrops rising above low-lying regions filled with sand and possibly the presence of a thin layer or absence of dust. This result is supported by the presence of ripples in these regions of the rough surfaces as seen in HiRISE images. Thus, the modeling of areal percentages of the different particle sizes will focus on these rough flows in Daedalia Planum.

Initial analysis of Daedalia Planum using a thermal model at a TES spatial resolution (3000 m) by Putzig and Mellon (2007) suggested that the surface best matches a mixture of rock and dust with a 4 mm thickness. However, analysis of HiRISE data over these flows shows significant variation on the surface and the presence of ripples indicative of accumulations of sand, suggesting that the dust cover on this flow field is not uniform. The use of a thermal model with higher spatial resolution THEMIS data (100 m) could identify surface mixtures at a finer

scale and potentially the amount of horizontal mixing and vertical layering. A more recent model can be adapted for a wider range of compositions and surface morphologies.

### **5.2.2 Thermal Conductivity Dominating Thermal Inertia ~ Particle Size Implications**

Thermal inertia is derived from the thermal conductivity, thermal capacity, and density of a material. A full description of the use of thermal inertia on Mars can be found in the previous chapter (section 4.2.2). Previous laboratory studies under Martian atmospheric conditions investigating these variables demonstrate the dominance of thermal conductivity in the calculation of thermal inertia on Mars (Neugebauer et al., 1971; Presley and Christensen, 1997). During these studies, thermal capacity and density of geological material varied by a factor of ~3 and thermal conductivity by 3-4 orders of magnitude. Furthermore, particle size is a defining factor of a material's thermal conductivity, which reduces with decreasing particle size due to the increase in the number of grain to grain contacts within a predefined unit (Jakosky, 1986; Presley and Christensen, 1997). These studies resolved that thermal inertia on Mars is strongly controlled by the particle size of the material and therefore can be used to interpret the effective particle size of a target surface.

Presley and Christensen (1997) further defined the relationship between thermal conductivity and particle size by studying homogenous spheres with varying diameters under Martian atmospheric conditions. This relationship was eventually described by the equation  $k = (CP^{0.6})d^{(-0.11 \log P/K)}$  where  $k$  is the thermal conductivity,  $d$  is the particle size in  $\mu\text{m}$ ,  $P$  is the atmospheric pressure in torr, and  $C$  and  $K$  are constants 0.0015 and  $8.1 \times 10^4$  torr (Presley and Christensen, 1997). This equation can be applied to the thermal inertia equation to derive the effective particle size from a specific thermal inertia value. With this detailed study on this

relationship, thermal inertia was proven an effective tool to constrain the particle and block sizes on the surface of Mars. However, one main complication with deriving this surface property is the presence of subpixel horizontal mixing and vertical layering of different particle sizes. The interpretation of high (bedrock) or low (dust) thermal inertia is relatively straight forward because at these values a single type of material property is dominating the signature, but moderate thermal inertia values can be explained by different combinations of particle sizes on a horizontally mixed surface (Fergason et al., 2006).

### **5.2.3 Skin Depth**

An important factor to consider regarding the potential properties derived from thermal inertia is the thermal skin depth, which is the measure of the depth to which thermal energy penetrates into the surface material for either a diurnal or seasonal cycle. Seasonal and diurnal skin depths identify the depth at which the temperature is  $1/e$  ( $\sim 0.37\%$ ) of the surface value measure temporally in relation to a season or day. Thus, in order for the bedrock layer material to be detected in orbital datasets, the thickness of the dust covering the lava outcrops must be less than the skin depth. However, the temperature and thermal response of a layered surface will differ from that of a homogeneous surface. This is due to the difference in balance of heat conduction and the heat storage between the different layers over the course of a day (Mellon and Putzig, 2007).

#### **5.2.4 Complications for Thermal Inertia: Presence of Vertical Layering**

Thermal inertia represents the thermal properties of the upper few centimeters of the surface. Therefore, it is critical to understand any layering of different materials that are present on the surface. Originally, many models assumed uniform material properties, both vertically and horizontally, at the pixel resolution of the dataset. Christensen et al. (2001) suggested that the derived temperature of a surface was the composite mixture of the component temperatures calculated at the resolution of the instrument. Even though this assumption is valid for investigating features larger than the spatial resolution of the dataset, this is not accurate for complex surfaces. With increasingly higher spatial resolution instruments available for more detailed studies, the complexity of a surface with both mixing and layering can be investigated.

The presence of dust deposits over the lava flow fields in Daedalia Planum complicate the interpretation of thermal IR data. A vertically layered system will display a thermal signature composed of a combination of the individual components dependent on the thickness of the upper layer in relation to the skin depth. For lava outcrops, with a high thermal inertia value, covered by a layer of dust, with a low value, the top layer will depress or mask the signature of the underlying outcrops increasingly with greater dust thickness. Specific visible signatures on the surface in this region suggest that assuming a continuously thick layer may oversimplify the surface. Wind streaks in Daedalia Planum identified by Edgett and Malin (2000) suggests that the mantling may not be uniform spatially and possibly not uniform over time. Thus, a thermal model must be used with the ability to quantify the amount of dust covering the flow surfaces and ultimately the presence of any horizontal mixing.

In Daedalia Planum, there is likely to be a thin layer of dust (low thermal inertia material) over the lava outcrops (high thermal inertia material) and the upper layer of dust will insulate the

lava outcrop from any extremes in surface temperature. Alternatively, the lava outcrops would draw away and store heat from the dust, which may shift the peak daytime temperature later in the day. During the evening, the stored heat in the lower layer will rise to the surface (Mellon and Putzig, 2007). Thus, it is critical to quantify the presence of any vertical layering on the flow surfaces in Daedalia Planum with dust as a predominant covering material and determine if this layering is thin enough to discern the signature of the lower material. Numerical thermal models have been developed that use the relationship between surface temperature and physical properties of the surface materials to determine the presence of either horizontal mixing or vertical layering on the surface of Mars (Putzig et al., 2013; Kieffer, 2013).

#### **5.2.5 Thermal Numerical Models: Horizontal Mixing and Vertical Layering**

To address complex surface structures with horizontal mixing and vertical layering, thermal models were developed applying the modified thermal inertia equation developed by Presley and Christensen (1997) to reverse model the diurnal curve using the properties for a specified particle or block size input. The modified layering thermal model derived by Mellon et al. (2004) is an effective method to compute the brightness temperature and thermal inertia of a surface with layered materials. To investigate variations in thermal inertia across Mars, Putzig and Mellon (2007) used TES data to numerically model two-component diurnal and seasonal temperature curves using fixed values of albedo, thermal inertia, density, and heat capacity for a set of idealized surface material (with increasing particle size of dust, sand, and rock). Analysis of Daedalia Planum using this model at a TES spatial resolution suggested that the surface contained both rock and dust, with a 4mm thickness of the latter.

#### **5.2.5.1 MARSTHERM: A Horizontal Mixing Thermal Model**

Putzig et al. (2013) developed the MARSTHERM web-based analysis tool, a thermal numerical model of the near-surface and atmosphere of Mars. Through this online tool, users input the thermophysical parameters of the target area, including thermal inertia, dust opacity, albedo, etc., along with the collection parameters, location, local slope angle, and solar azimuth, to calculate the diurnal and seasonal surface temperatures. An advantage of this surface thermal model is the ability to incorporate two-component horizontal mixing, with different particle sizes or material properties, to produce diurnal and seasonal temperature curves complex surfaces. This tool is based on a standard subsurface thermal model for Mars, a radiative transfer through atmospheric dust and CO<sub>2</sub> to quantify the boundary condition of the surface (Haberle and Jakosky, 1991; Putzig et al., 2013). This heterogeneity modeling provides critical details for the thermophysical study of the Mars surface, but is limited by an inability to incorporate complex layered systems. Thus, MARSTHERM is mainly useful for surfaces with mixtures of two individual uniform materials.

#### **5.2.5.2 KRC: A Vertical Layering Thermal Model**

The KRC thermal numerical model calculates the surface temperature given certain input parameters to produce diurnal and seasonal temperature curves (Kieffer, 2013). Location parameters can be determined directly from an instrument dataset or by the user. The advantage of the KRC model is the ability to account for the vertical layering of different materials and sloped surfaces. Users can define a multilayered system controlling the composition, layer thickness, thermal inertia, and particle size properties (i.e. porosity), all of which will affect the resulting diurnal and seasonal curve. The ability to control the thickness of the upper layer provides critical information to understand a variety of layered systems and define the sensitivity

of the model to the properties of each layer. An additional benefit is the ability to specify the slope (a topographic parameter) which takes into account the orientation of the sun, surface, and receiving satellite at the time of data acquisition to account for the effects of this feature.

Every parameter in the KRC model can be changed, allowing for extensive user control and the ability to model infinite variations of a layered surface. Using these input parameters, a virtual surface is modeled to calculate the diurnal and seasonal surface temperatures by solving the heat diffusion equation. The upper boundary condition takes into account periodic insolation through the atmosphere (that is dusty) and radiative transfer with the atmosphere in the infrared (Kieffer, 2013). However, this model lacks the ability to horizontally mix either single or layered systems, which is likely present on complex surfaces. Of specific interest for this study is the ability to manipulate the multilayer parameters to identify the surface properties on the lava flows in Daedalia Planum.

The KRC model has been extensively used to study the Martian surface for Mars missions containing a thermal infrared sensor and landing site selections (Christensen et al., 2005b; Golombek et al., 2005; Arvidson et al., 2008). This model is also used for standard data reduction processing for the THEMIS datasets and to estimate the surface temperature for the blackbody emission corrections for the Compact Reconnaissance Imaging Spectrometer for Mars (CRISM) (Christensen et al., 2003 & 2005a; Titus et al., 2003; Martin, 2004).

### **5.3 Methods**

This study builds on the previous chapter, the unusual thermophysical and surface properties of the Daedalia Planum lava flows, from which a four category classification system



was established to identify the thermal response of the lava flows and determine the location of potentially exposed lava outcrops on the surface. Through this work, rough category C flows with a low daytime and high nighttime brightness temperature response were identified as the best candidates for further investigation of lava outcrops with sand in low lying regions and nonhomogeneous dust coverage. Because the purpose of this project is to quantify the presence of lava outcrops on the surface, the following work focused only those flows identified previously as having the highest potential presence of lava outcrops.

### **5.3.1 Datasets**

Using a multi-instrument and multispectral approach, datasets with different spatial and spectral resolutions were used to derive information about the surface properties: 1) Mars Reconnaissance Orbiter ConTeXt Camera (CTX) and High Resolution Imaging Science Experiment (HiRISE) images and 2) Mars Odyssey Thermal Emission Imaging System (THEMIS) TIR and TI images (Table 10). Visible datasets, at different spatial resolutions, were used to identify the lava flow boundaries, characterize the surface textures, and define the areal percentage of potential exposed lava outcrops. Thermal data collected by THEMIS were used in the previous chapter to quantify the thermophysical variation on the surface and identify areas with potentially exposed lava outcrops. Thermal inertia values for Mars are derived from THEMIS nighttime data using a thermal model and an extensive look-up table with the albedo, elevation,  $L_s$ , latitude, and local time of day (Fergason et al., 2006). The variation in the thermal datasets was used to quantify the diurnal temperature response for these flow surfaces.

**Table 10. Applications of visible and thermal infrared datasets to investigate the lava flows in Daedalia Planum (<sup>a</sup>Malin et al., 2007; <sup>b</sup>McEwen et al., 2007; <sup>c</sup>Christensen et al., 2004; <sup>d</sup>Ferguson et al., 2006; <sup>e</sup>Ruff and Christensen, 2002).**

<b>Identify Lava Flow Boundaries and Characterize Surface Textures</b>		
<b>Instrument</b>	<b>Acronym</b>	<b>Spatial Resolution (m)</b>
MRO ConTeXt Camera <sup>a</sup>	CTX	6
MRO High Resolution Imaging Science Experiment <sup>b</sup>	HiRISE	0.3
<b>Quantify Thermophysical Properties</b>		
<b>Instrument</b>	<b>Acronym</b>	<b>Spatial Resolution (m)</b>
Thermal Emission Imaging System IR Brightness Temperature Day and Night <sup>c</sup>	THEMIS	100
THEMIS Derived Thermal Inertia <sup>d</sup>	TI	100
Thermal Emission Spectrometer Dust Cover Index <sup>e</sup>	TES DCI	3000

### 5.3.2 A Dual Method Approach to Interpreting Thermal Inertia

A dual method approach using both direct remote sensing TIR techniques and reverse thermal modeling with individual components is used to quantify the amount of horizontal mixing and vertical layering present on the surface. Thermal inertia and day/night brightness temperature values were collected from the THEMIS data for a remote sensing approach and the reverse modeling used ideal components based on the constraints identified from orbital data (Figure 33). For the remote sensing approach, the statistics on the THEMIS data were already collected in the previous chapter in which ROIs were used to sample the daytime and nighttime brightness temperatures along with thermal inertia for the lava flows in Daedalia Planum (section

4.3.5). In this study, these results will be compared to the thermal model results to define the amount of dust, sand, and lava outcrops on the surface. The thermal modeling approach focuses on predicting the diurnal and seasonal surface temperatures of a surface based on the collection parameters and user defined vertical layering and horizontal mixing of ideal components. Specific input parameters (day, time and solar alignment) were derived directly from the THEMIS stamps. To accurately model the potential particle size combinations present on the surface, three idealized surface components were defined, all having a basaltic composition but with different particle sizes (dust, sand, and rock). These ideal components were based on previous studies demonstrating that these flows are basaltic in composition (Crumpler et al., 1996; Lang et al., 2009; Edward et al., 2011). Following the method defined by Putzig and Mellon (2007), fixed values of albedo, TI, density, and heat capacity were defined for each particle or block size (Table 11). The last variable to define is the thickness of any upper layer or the areal percentage of each component in regards to horizontal mixing.

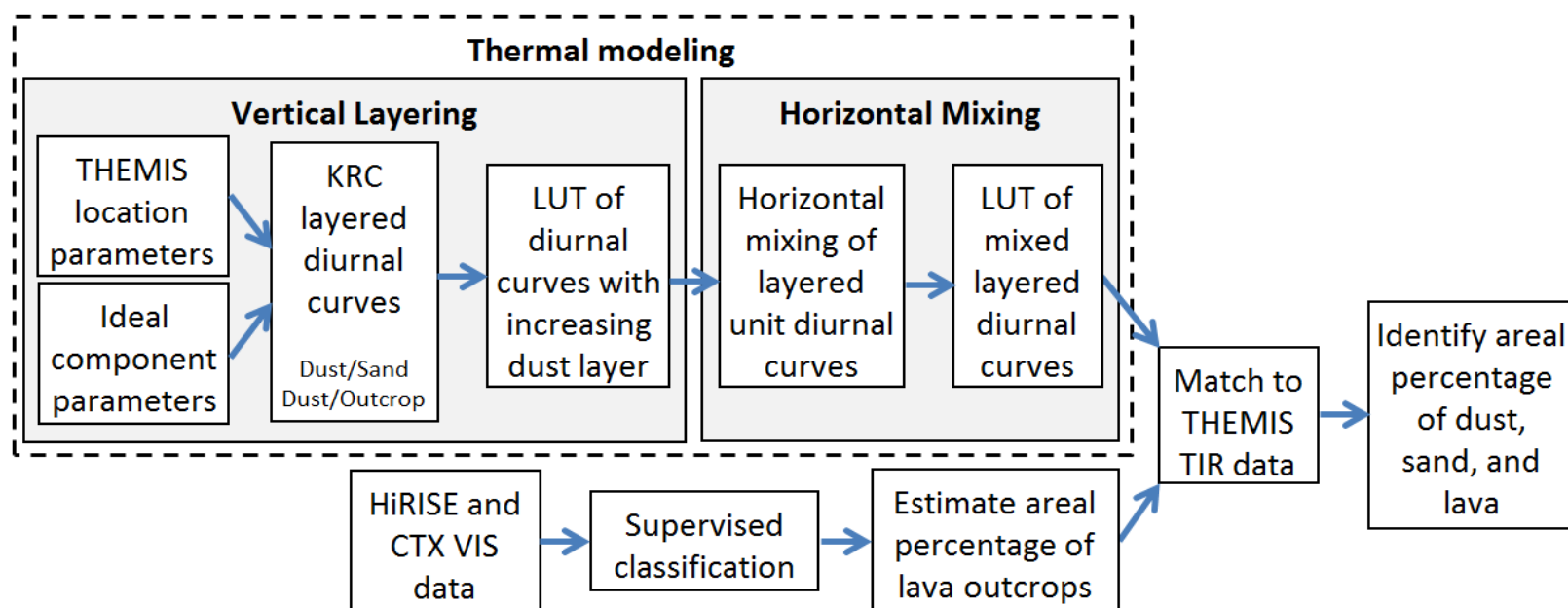


Figure 33. Flowchart of the method combining modeling and remote sensing techniques to identify the horizontal mixing and vertical layering of dust, sand, and lava outcrops present on the surface.

Table 11. Description of the ideal components used in the KRC model from Putzig and Mellon (2007) and Fergason et al. (2006).

Material	Particle Size	TI	Porosity	Heat Capacity	Conductivity	Density
		tiu	(%)	$\text{J kg}^{-1} \text{K}^{-1}$	$\text{J s}^{-1} \text{k}^{-1} \text{m}^{-1}$	$\text{Kg m}^{-3}$
Dust	2 $\mu\text{m}$	56	0.53	837	0.003797	1386.5
Sand	295 $\mu\text{m}$	223	0.43	837	0.0496582	1681.5
Lava Outcrops	>1 m	2200	0.05	837	2.89987	2802.5

### **5.3.3 MARSTHERM Modeling of Horizontally Mixed Areas**

MARSTHERM was used to numerically model one-component and horizontally mixed two-component single layer diurnal and seasonal temperature curves (Putzig, 2013). Unfortunately, this model does not include vertical layering of different materials and is limited to the mixture of two components. Three idealized surface materials of dust, sand, and rock were first used to create single component runs and then mixtures of sand/rock and dust/rock (Table 11). A series of location parameters, defined by the THEMIS stamps, were required to determine the solar azimuth and longitude at the collection time (Table 12). Single component (without layering or mixing) runs were completed to understand and quantify the difference in the diurnal and seasonal temperature responses of the three particle sizes. Mixed two-component (without any layering) models of either dust/rock or sand/rock were run with different areal percentages summing to 100%. Successive mixed runs varied the areal percentage of the two components by 10% to produce a comprehensive suite of mixed surfaces. These runs were also completed for a series of THEMIS collection parameters (i.e. different seasons) for accurate comparison to different THEMIS data. Results of the dust/rock and sand/rock idealized mixed runs were compared with the average day and night brightness temperatures calculated from the THEMIS data for each flow.

**Table 12. Input parameters for MARSTHERM to model single layered, horizontally mixed systems (Putzig, 2013).**

Variable	Range of Potential Values
Thermal Inertia	5 to 5000 tiu
Effecting Semi-Infinity CO <sub>2</sub>	0.001 to 60 kg/m <sup>2</sup>
Surface Pressure	0 to 1000 mb
Atmospheric Dust Opacity	0 to 1000
Lowest (Southern Most) Latitude	-90 to 90
Albedo of Bare Ground	0 to 1
Bare Ground Emissivity at 15 $\mu$ m	0 to 1
Bare Ground Emissivity Not at 15 $\mu$ m	0 to 1
Surface Slope Angle	0° to 90°
Surface Slope Azimuth	0° to 360° E of N
Solar Longitude (Season)	0° to 360°
Mode	Diurnal or Seasonal Cycle

#### **5.3.4 Modeling Vertically Layered Units in the KRC Model**

To quantify the vertical layering present in Daedalia Planum, the KRC model was used to determine the effect of varying thicknesses of dust cover over sand and lava outcrops (Kieffer, 2013). The same three idealized surface materials (dust, sand, and lava outcrops) were used in the layered thermal model with fixed values of albedo, TI, density, and heat capacity (Table 11). A more detailed set of location parameters, derived from THEMIS stamps, were required compared to the MARSTHERM model to understand the radiance balance on the surface (Table 13; Appendix D). Using the defined components, the KRC model establishes the properties of each layer with the specified thickness of the top layer and calculates the diurnal curves for the layered unit. Results modeled the surface temperature variation produced by sand with a layer of dust and lava outcrops with a layer of dust. Successive runs increased the thickness of the dust layer to create a complete look-up table (LUT) for use in a horizontal mixing code. Similar to the MARSTHERM application, these runs were completed for a series of different seasons for accurate comparison to THEMIS data. Before comparison with the THEMIS data, the produced layered diurnal and seasonal curves must be horizontally mixed to reflect the complex surfaces in Daedalia Planum.

**Table 13. KRC input parameters, including a description and how it is derived, used to calculate vertically layered diurnal temperatures and thermal inertia (Kieffer, 2013).**

Variable	Derived from	Description
<i>Location Parameters</i>		
Lat	THEMIS Stamp	Location latitude
Lon	THEMIS Stamp	Location longitude
Elev	THEMIS Stamp	Location elevation
SLOPE	THEMIS Stamp	Location slope
SLOAZI	THEMIS Stamp	Azimuth
TAUD	Seasonal Dependent Parameter	Dust Opacity
Ls	THEMIS Stamp	Season
TAURAT	Standard	Ratio of Thermal to Visible Opacity of Dust
DUSTA	Standard	Single Scattering Albedo of Dust
<i>Material Properties</i>		
Mat 1	'Basalt'	Top layer material composition
Inertia 1	Rock, Sand or Dust Constant	Top layer thermal inertia
Por 1	Rock, Sand or Dust Constant	Top layer Porosity
Thick	Rock, Sand or Dust Constant	Top layer thickness
Mat 2	'Basalt'	Bottom layer material composition
Inertia 2	Rock, Sand or Dust Constant	Bottom layer thermal inertia
Por2	Rock, Sand or Dust Constant	Bottom layer porosity



#### 5.3.4.1 Horizontal Mixture of Vertically Layered Units

An Interactive Data Language (IDL) script was written to calculate the horizontal mixtures of the layered KRC runs to predict the diurnal curve for a complex surface with both vertical layering and horizontal mixing (Appendix E). This code is based on the linear mixture of emitted flux in the Stefan-Boltzmann equation ( $\epsilon\sigma T_s^4 = \epsilon\sigma \sum_i A_i T_{s_i}^4$  where  $T_{s_e}$  is the effective surface temperature,  $T_{s_i}$  is the component surface temperature, and  $A_i$  is the fractional area of the component; Putzig and Mellon, 2007). The user defines the areal percentage of the layered units (dust/sand and dust/lava outcrop) and at each point along the diurnal curve the temperatures of each KRC layered run are linearly combined based on the user input. This code was run with different areal percentages summing to 100% of sand with a layer of dust and rock with a layer of dust as the two surface endmember components. Successive runs varied the areal percentage of the two components by 5%. The first set of mixed layered runs had the same dust thickness for both components and additional runs modeled scenarios in which the dust layer covering the sand was thicker than the dust covering the lava outcrop. This situation may occur where wind is strong enough to clear the lava outcrops rising above the surrounding dust covered surface. Additionally, single layer runs as defined by the KRC model for each of the ideal components (for continuity) were horizontally mixed using the same methods as described.

### 5.3.5 Look-Up Tables Matched to THEMIS Data

With the completion of both the remote sensing method to derive surface temperatures from THEMIS data and the thermal numerical model to predict the diurnal temperature curve given specific input parameters, these two methods were compared to quantify the possible combinations of dust, sand, and lava outcrops on the flow surfaces. All results from the horizontal mixing of the KRC runs, including both single and layered systems, were compiled into an extensive look-up table (LUT). These results were compared with the average day and night brightness temperatures calculated from the THEMIS data for each flow. Specific care must be taken to compare models and THEMIS derived values from similar seasons (Figure 34). Not only does the temperature of the surface vary over the course of a day, but seasonal variations exist as well due to the orbit of Mars. Matching of the THEMIS data (using the remote sensing method) and the mixed layered model diurnal curves (using a thermal numerical model) was also completed by a simple IDL script used to quarry the model runs. HiRISE (where available) and CTX data were then assessed to visually estimate the percentage of lava outcrops within the area to accurately identify the correct areal percentages of the sand and outcrop components from the LUTs.

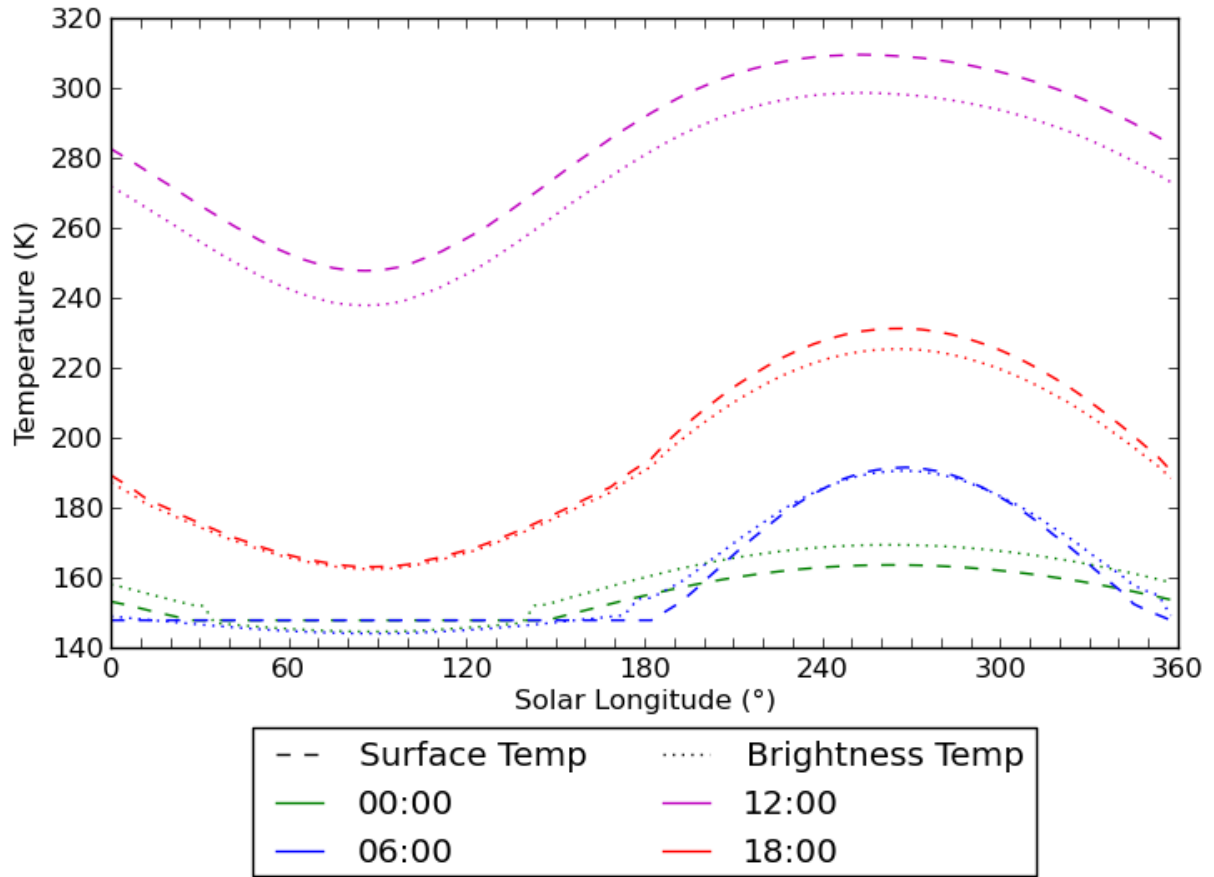


Figure 34. Seasonal curves for dust at four different times of day (6 hour increments) to demonstrate the seasonal and diurnal variability. The diurnal curve usually reaches the peak at ~12:00, but the maximum temperature reached by the surface varies by ~60 K depending on the season.

### 5.3.6 Supervised Classification of Lava Outcrops in HiRISE Data

An additional remote sensing method using visible datasets was used to further constrain the possible distribution of dust, sand, and lava outcrops on the surface. 15 HiRISE (0.30 m/pixel) data were used to qualitatively investigate the presence of lava outcrops on the lava flow surfaces. A supervised classification was applied the visible datasets to quantitatively identify the amount of exposed lava outcrops on the surface of the rough flows (Figure 35A). The locations of lava outcrops can be identified visually due to the distinct features in this wavelength region. These elevated areas are recognized by bright surfaces alongside minor shadowing and smooth surfaces are darker and either lack distinct features or display ripples that suggest the presence of sand (Figure 35B). These supervised classifications were further quantitatively analyzed to identify the areal percentage of identified lava outcrops in areas sampled by 70 ROIs established in the last chapter (section 4.3.5) to investigate the thermophysical variation on the lava flows. These results were used as supporting information to the THEMIS data and modeled diurnal cycles to quantify the combinations of dust, sand, and lava outcrops on the surface.

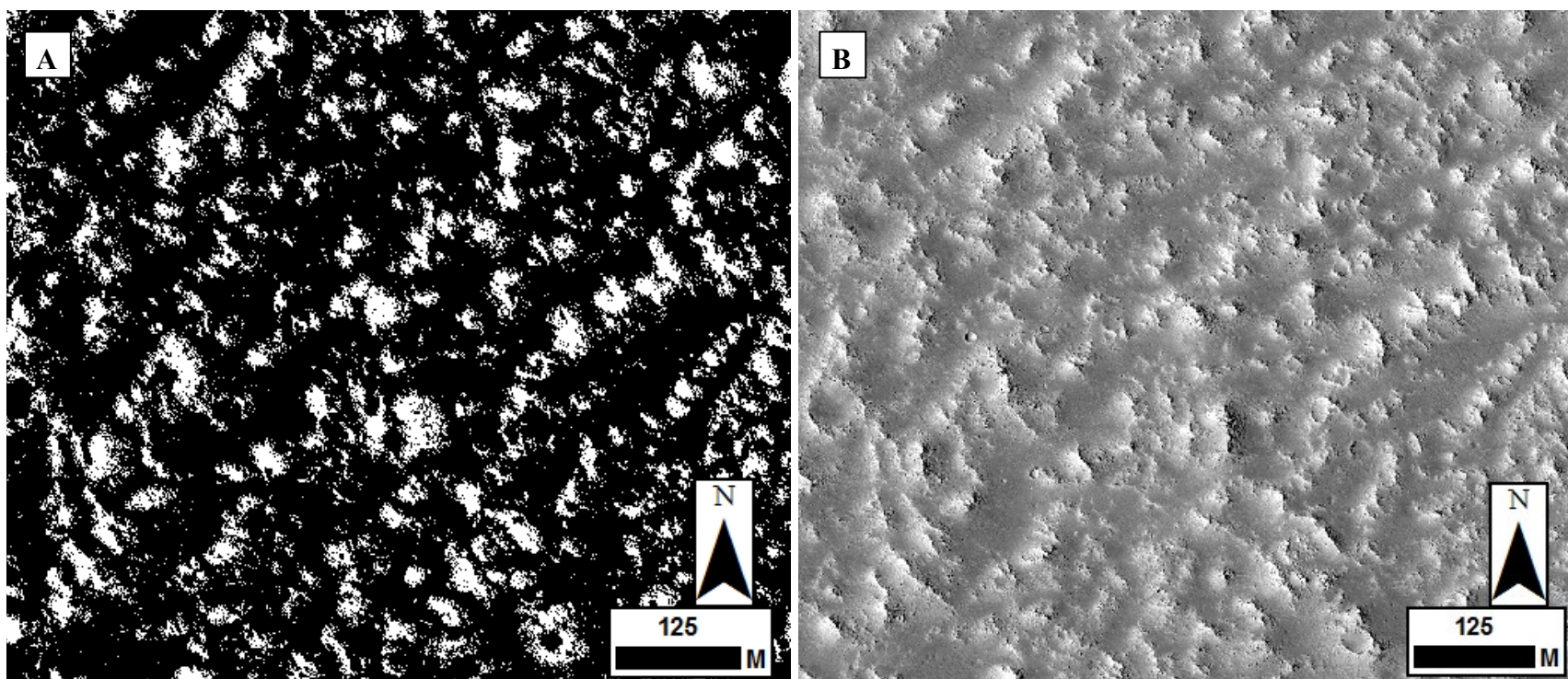


Figure 35. (A) Supervised classification of a rough category C flow with ~40% lava outcrops in white and sand/dust in black and (B) HiRISE data from which the supervised classification was derived (PSP\_002711\_1550).

### 5.3.7 ROTO Data

The Routine Off-nadir Targeted Observation (ROTO) data acquired over the Daedalia Planum flow field provide an innovative approach to understand the surface roughness and unique thermophysical properties of these lava flows. A ROTO sequence triplet was collected during a 5 day period: I68222002 (nadir), I68197002 (13°), and I68172002 (28°) (Table 14). The goal was to define the surface morphology of this lava flow field using the increasing emission angles of the ROTO data. This region was previously modeled to have some of the roughest surfaces on Mars, so it was a prime target for this type of analysis (Bandfield, 2009). Derived Projected Brightness Temperature (PBT) data with these unique emission angles were examined to better understand the thermophysical variation on the flows caused by differences in roughness suggesting the presence of different distributions of dust, sand, and lava outcrops. Three delta temperature ( $\Delta T$ ) images were produced by taking the difference between two selected ROTO images: I68222002 (nadir) minus I68197002 (-13°), I68197002 (-13°) minus I68172002 (-28°), and I68222002 (nadir) minus I68172002 (-28°). Variability with the increasing emission angles may be due to the orbital location/orientation, thermal inertia properties of the surface (specifically the surface roughness), or albedo. This sequential triplet, with the limited time between collections, enables other observation parameters such as solar distance, local time, solar longitude, and incidence angle to be eliminated as potential sources of error. Therefore, any observed differences strongly suggest that surface morphology/roughness is present on the surface.

**Table 14. ROTO data collection parameters.**

<b>Material</b>	<b>Collection Angle</b>	<b>Local Time</b>	<b>Solar Longitude</b>	<b>Incidence Angle</b>	<b>North Azimuth Angle</b>
I68222002	0°	17.95	357.929	88.97	262.23
I61897002	13°	17.83	356.893	87.12	262.19
I68172002	25°	17.70	355.852	85.20	2802.5

## **5.4 Results**

### **5.4.1 Mixtures of Single Layer Systems**

Initial comparison of the single-layer, horizontally mixed results from MARSTHERM and THEMIS data of the targeted rough flows strongly suggests the presence of up to 40% rock (lava outcrops) on the flows (Figure 36). Within these derived diurnal plots, two methods are used to predict the diurnal curve of a horizontally mixed surface. The first method uses the areal-weight of each component to predict the mixed area TI before running the model to predict a diurnal curve (area-wt average dotted line). The second method predicts the diurnal curve for each component separately and then the brightness temperature values are combined based on the areal-weight of each component (solid line). Comparison of these two methods demonstrates the variability possible in the predicted values depending on how the thermal signatures of two different materials are mixed (i.e. before or after the modeling process). Specific care must be taken to combine the predicted brightness temperature after the predictive model is run rather than combining the properties beforehand because this will lead to an overestimation of the thermal inertia and particle or block size. This comparison demonstrates that a significant

amount (up to 40%) of lava outcrops are exposed (to an unknown degree) on the rough flow surfaces. If lava outcrops were completely mantled, the THEMIS data would only match the results of model runs with 0% rock abundance. However, the most realistic scenario includes a horizontal mixing model of two-layered vertical endmembers with dust over sand and dust over lava outcrops. Distinct ripple features can be seen in the low-lying areas of the rough flow surfaces in HiRISE data, indicating that the most accurate model should include a significant sand component with the presence of vertical layering of dust.



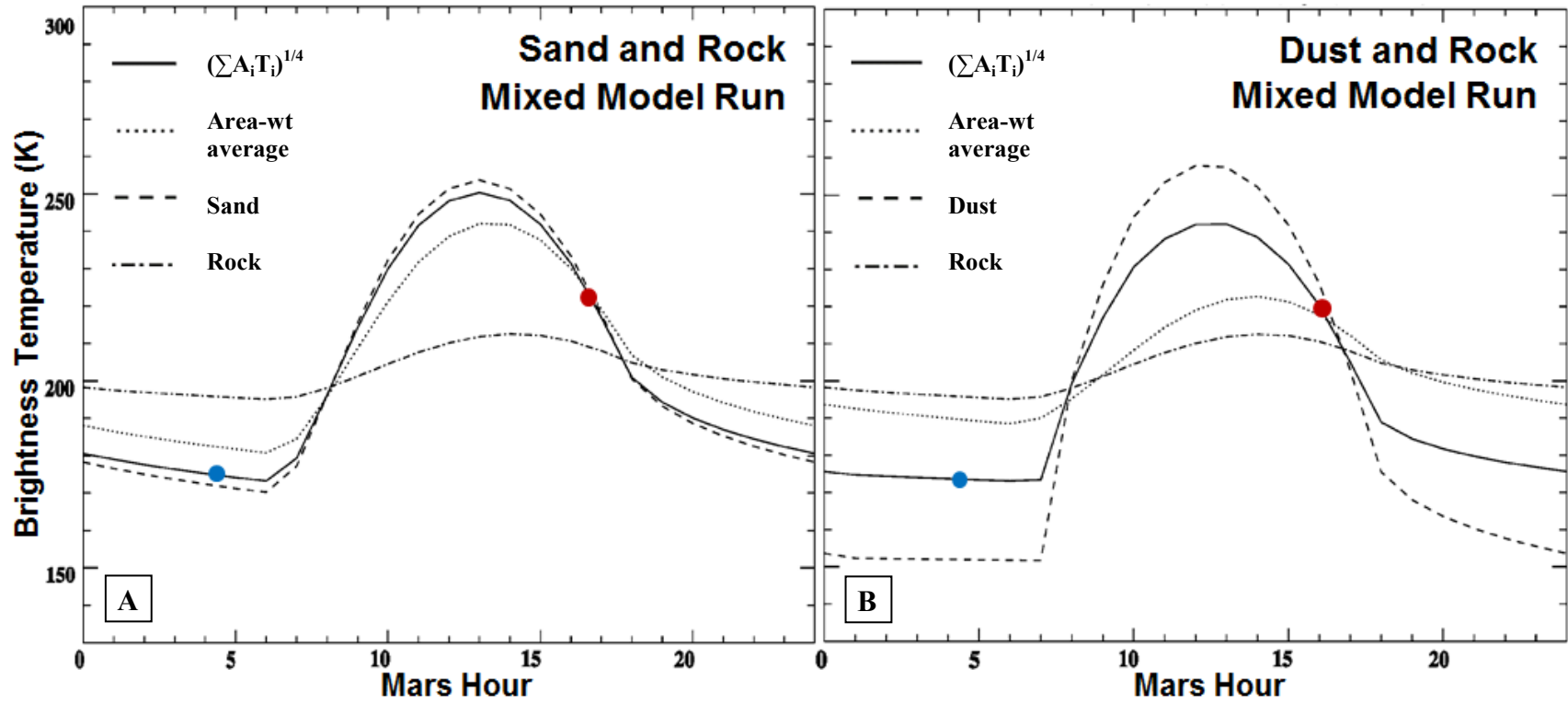
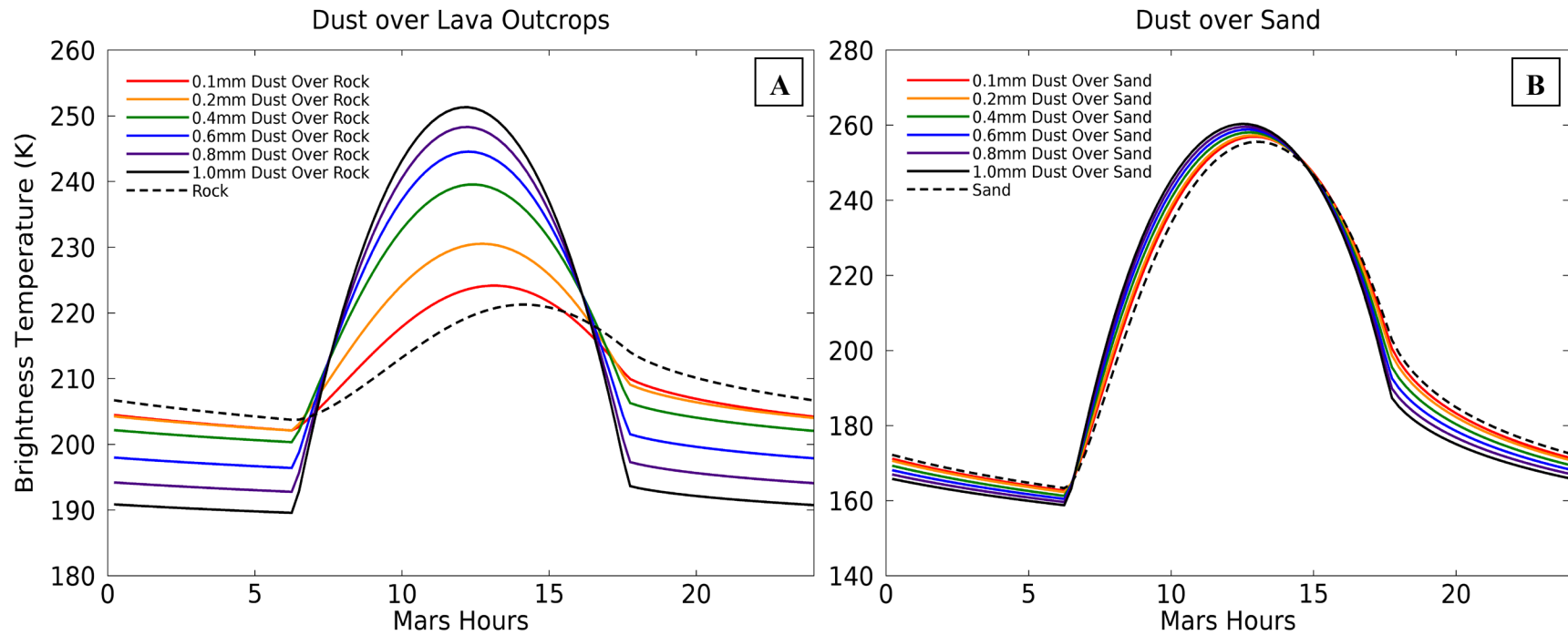


Figure 36. Modeled diurnal brightness temperature curves of a (A) 90% sand and 10% rock mixture and (B) 60% dust and 40% rock mixture that best match the THEMIS data for a category C rough flow. The local time for two THEMIS stamps are denoted by red and blue circles (day = 16:31 and night = 4:46).

### 5.4.2 Layered Units

With initial analysis of mixed surfaces without any layering demonstrating the presence of significant observable lava outcrops, the effect of layered units (specifically a covering of dust) must be incorporated. The process of calculating the diurnal and seasonal surface temperatures for layered units (dust over sand and dust over rock) is only the initial step in the modeling approach, but the resulting temperature diurnal curves provide significant information about the effect of dust over a surface (Figure 37). The analysis of increasing thicknesses of dust demonstrates that the signature of the lava outcrops is significantly more affected or masked by the presence of a dust cover compared to a base layer of sand. This is realistic because the shape of the diurnal temperature curves for dust and outcrops are drastically different (they represent opposite sides of the spectrum) with dust having the greatest temperature change over a day and outcrops or bedrocks the least. Also, the hour at which the peak temperature is reached by the proposed surface shifts to an earlier time with increasing dust thickness, which occurs because finer materials heat up faster than larger objects. In regards to the dust/sand analysis, the increase in dust layer has a slightly stronger affect initially compared with the relatively constant shift of the sand signature to a more dust signature. An additional aspect to note is that at 1 mm coverage, the predicted surface does not completely resemble a dust diurnal temperature signature and the underlying material can still be investigated.



**Figure 37. Diurnal temperature curves of (A) rock (lava outcrop) with increasing thickness of dust cover and (B) sand with increasing thickness of dust cover. These plots show how increasing dust thickness masks the thermal signature of the lower layer and that the dust has a greater impact on the thermal response of rock.**

### 5.4.3 Horizontal Mixtures of Layered Systems

Comparison of the horizontal mixtures of the layered KRC runs with the THEMIS-derived thermal responses of targeted category C rough flows reveals that multiple combinations of dust/sand and dust/lava outcrop can produce very similar diurnal curves. Without further support from the visible supervised classification to constrain the possible amount of lava outcrops identifiable on the surface, this comparison suggests that these flow surfaces may have 40-80% lava outcrops with a dust cover thickness ranging from 0.2 mm to 1.5 mm (Table 15; Figure 38). Rather than a continuous layer of dust covering the sand and lava outcrop components, this analysis suggests the presence of a significantly thicker layer of dust over the sand component, with up to an order of magnitude difference. However, this horizontal mixing technique does not take into account the transition zones between the two dust thicknesses nor any minor variability. Due to the spatial resolution of the THEMIS dataset (100 m) this is likely to have little effect on the averaged response of a pixel, but this complication may require further investigation if new higher spatial resolution TIR data is developed in the future. To further constrain the possible areal percentages of sand/dust and outcrop/dust, the qualitative analysis of the supervised classifications using HiRISE data were used to estimate the corresponding areal percentages of these two layered units for each flow. This combined analysis using visible and thermal infrared data with thermal modeling suggests that the areal percentage of lava outcrops on these flow surfaces is a maximum of 40%.

**Table 15. Results of the comparison between the KRC vertically layered and horizontally mixed diurnal curves and THEMIS derived temperatures at two specific times. These values represent the potential areal percentages of layered sand and lava outcrops layered components (the bold and underlines percentages corresponding to the HiRISE classification results).**

Rough Category C Flows			
Thickness of dust over lava outcrops	Thickness of dust over sand	Sand Areal Percentage	Lava Outcrop Areal Percentage
mm	mm	%	%
<b><u>0.2</u></b>	<b><u>4-5</u></b>	<b><u>60</u></b>	<b><u>40</u></b>
0.6	3-3.5	50	50
0.7	2.5-3.5	50	50
0.7	4-4.5	45	55
0.75	2.5-4	45	55
0.8	2.5-3.5	45	55
0.8	4-5	40	60
0.85	2.5-3	45	55
0.85	3.5-4.5	40	60
0.9	3.5-5	40	60
0.95	2-4	40	60
0.95	4-5	35	65
1	2-3	40	60
1	3.5-4.5	35	65
1.5	0.85-2.5	20	80

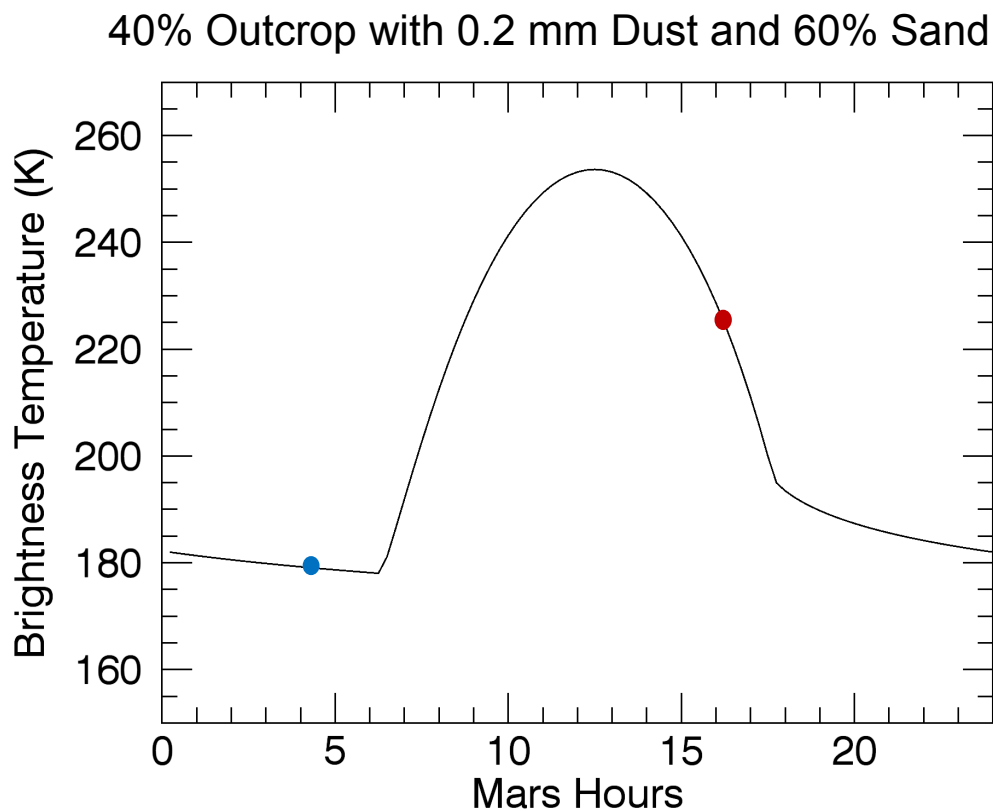


**Figure 38.** Diurnal curve of a horizontally mixed layered system that best matches the THEMIS data for category C rough flows 5, 18, and 29. The local time for THEMIS stamps are shown (day: 16:31 and night: 4:46).

Results strongly suggest that the maximum dust thickness over the lava outcrops for category C rough flows is 0.2 mm. This dust cover estimate is significantly less than previous studies suggested for the area (roughly 4 mm; Putzig and Mellon, 2007) due to the use of higher spatial resolution datasets (TES has a spatial resolution of 3 km compared to THEMIS at 100 m) and the assumption that only a single layered unit was present of dust over rock. Assuming uniform material properties at the pixel spatial resolution of TES and thus ignoring the presence of any horizontal mixing on the surface with sand caused an overestimation of the dust layer. If

lava outcrops were not identifiable, THEMIS data would only match model runs with 0% rock abundance.

Horizontal mixtures of layered KRC runs for smooth category B (low daytime and high nighttime temperature response with low thermal inertia) flows demonstrate a significantly greater presence of the sand component on these surfaces (roughly 15-25% higher than rough flows). These results suggest that the lava flow surfaces in Daedalia Planum do in fact have a complex combination of vertical layering and horizontal mixing of dust, sand, and exposed lava that varies by flow surface type. This quantifiable difference demonstrates that the thermophysical variation assessed in the previous chapter is predominantly due to differences in the areal distribution of dust, sand, and lava outcrops on the surface. With category B flows containing more vertical layering of dust and horizontal mixing of sand compared to category C flows.

A non-homogeneous layer of dust is present on the surface of these rough flows with 0.2 mm over the lava outcrops and between 4-5 mm of dust over the sand. This significant difference in dust thickness suggests the presence of winds in Daedalia Planum strong enough to clear the lava outcrop peaks of significant layers of dust. This could also cause pooling of the dust in the low-lying regions filled with sand, further explaining the dust thickness results documented for the horizontal mixtures of layered KRC runs. Exposed lava outcrops with 0.2 mm of dust covering can be targeted for further spectral analysis by removing of the dust signature using the defined areal percentages and a linear deconvolution model.

#### 5.4.4 ROTO Data

Although the local collection time is very similar for each of the images, there are slight differences that provide detail about the surface roughness. I68172002 at  $28^\circ$  is the earliest collection at 17.7 local time and I68222002 at nadir is the latest at 17.95 local time. Ignoring the difference in emission angle and considering only the diurnal temperature curve of a material, earlier local time data should have a slightly higher temperature compared to the latter. The degree of this difference is proportional to the diurnal curve and thermophysical properties of the material. For example, a surface completely covered with dust will have a greater difference between time sequential images, whereas a surface dominated by blocky material or lava outcrops may show no difference.

Analysis of the temperature difference between stamps demonstrates the presence of distinct differences between the flows in this ROTO sequence (Figure 39). For example, in the bottom portion of the scene, an older lava flow can be differentiated from the other flows displaying a lower temperature with progressively later images. This demonstrates that the smooth flows respond with the expected trend of a surface covered by dust. Alternatively, flows in the northern portion display the inverse response of either only a minor decline in temperature with time (indicative of larger particle sizes or blocky material) or a warming (when only local time variation is considered). This increase in temperature is suggestive of rougher surfaces and may occur because of the emission angle in relation to the exposure to the sun. At the  $28^\circ$  emission angle, the data detect the shadowed sides of the rough surface preferentially. The ROTO data also suggest that such a sequence would be useful for any study of impact craters having rough ejecta and crater walls.



A few thermal properties of the surface need to be considered to fully understand the ROTO data. Temperature data collected at different emission angles may be affected by either the surface roughness and/or a mixture of dust, sand, and rock outcrops. Application of the KRC thermal inertia model can provide increasing detail on thermophysical mixing studies. The ability to model the amount of dust, sand, and rock of the surface can also inform the ROTO results. Similarly, the ROTO data may help to validate the thermal inertia modeling and ultimately, further constrain the potential thermophysical causes of the temperature variations seen in the ROTO data.

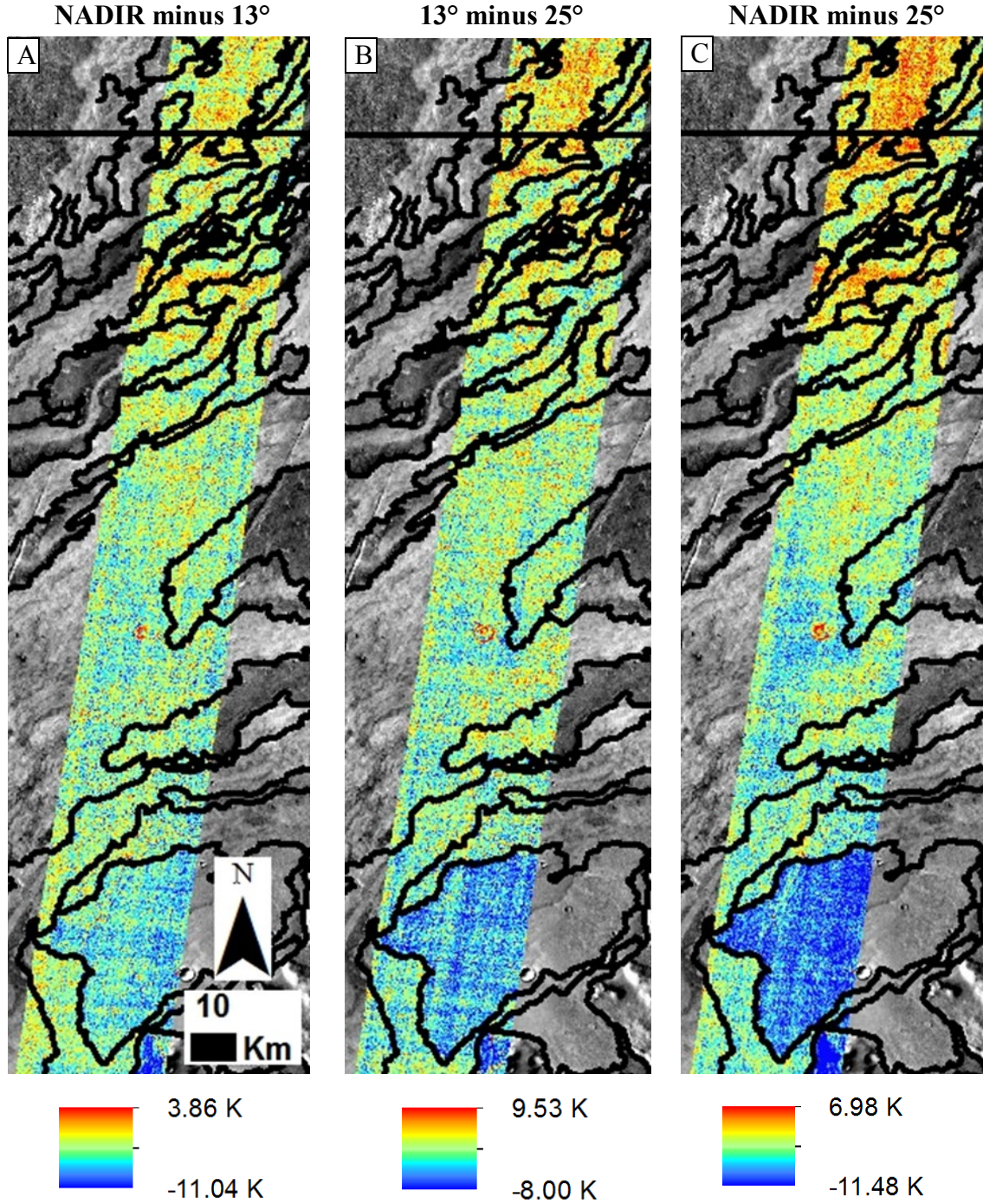


Figure 39. Temperature differences between ROTO images with lava flow boundaries shown in black (Crown et al., 2015) with higher negative values suggestive of fine grained surfaces. (A) I68222002 (nadir) minus I68197002 (-13°), (B) I68197002 (-13°) minus I68172002 (-28°), and (C) I68222002 (nadir) minus I68172002 (-28°). Note that these comparisons always follow the formula (later local time minus earlier local time).

## 5.5 Conclusion

Dust significantly hinders thermal infrared studies of the surface materials on Mars. With a relatively high DCI of 0.95-0.97, Daedalia Planum was previously considered too dusty for this type of study because a significant layer masks the signature of the material underneath. This study established a method by which the horizontal mixing and vertical layering of dust, sand, and lava outcrops can be quantified to determine the potential for further spectral analysis. This technique is critical to investigating some of the youngest flows on Mars that can provide significant information about the evolution of volcanism in the Tharsis region (Crown and Ramsey, 2016).

To investigate the surface properties of the rough category C lava flows, a two method approach was developed using both remote sensing techniques and numerical thermal models. The remote sensing technique utilizes THEMIS data to discern the change in brightness temperature over a day and the thermal numerical model uses ideal components (based on constraints identified from orbital datasets) to predict the diurnal and seasonal temperature curve of a hypothetical surface. Daytime and nighttime temperature values for the rough flows in Daedalia Planum were collected from THEMIS data to understand the thermophysical properties of the flow surfaces. The KRC thermal model calculates the diurnal curve of a surface with layered components: sand with a layer of dust and lava outcrop with a layer of dust for this study. Analysis of these layered runs demonstrates the more pronounced masking effect of dust over lava outcrops proportional to the thickness of the dust top layer. This comparison emphasizes the necessity to accurately estimate the dust thickness and areal percentage of lava outcrops on these flows to determine whether or not the outcrops can be targeted for other works.

To model a complex system with both layering and mixing, the layered diurnal curves were horizontally mixed using an IDL script with areal percentages summing to 100%. Results of the dust/sand and dust/rock layered mixed runs were compared with the average day and night brightness temperatures calculated from THEMIS data for the rough category C flows to identify the corresponding match that defines the horizontal mixing and vertical layering of the ideal components on the surface. The comparison of these two methods demonstrates that multiple combinations of vertically layered and horizontally mixed systems of dust, sand, and lava outcrops can follow similar diurnal curves. Estimated areal percentages of identifiable lava outcrops in HiRISE data calculated using a supervised classification constrained the possible matches between the remote sensing technique and thermal modeling. Comparison of the model results, THEMIS data of the category C rough flows, and visible supervised classification percentages demonstrates the presence of up to 40% rock (lava outcrops) on these flows, which can be targeted for future detailed compositional investigation (Figure 38; Table 15). This corresponds with a maximum dust thickness over the outcrops of approximately 0.2 mm and 4-5 mm over the sand.

This new thermophysical modeling reveals that lava flows in Daedalia Planum are not completely or uniformly dust mantled and some flow surfaces contain up to 40% observable outcrops with a 0.2 mm layer of dust (which is below the optical thickness). The dust cover on the rough category C lava flows is estimated to be significantly lower than previous estimates by Putzig and Mellon (2007) who measured a 4mm thickness using 3km spatial resolution TES data. Qualitative analysis of visible HiRISE data constrained the maximum areal percentage of lava outcrops on these flow surfaces to be roughly 40% further decreasing the maximum dust thickness to less than 0.2 mm. These results also indicate the presence of a significantly thicker

layer of dust over the sand component in the low-lying regions of the flow surface. The presence of a non-homogeneous layer of dust on the rough category C flows suggests the presence of winds in Daedalia Planum strong enough to reduce the development of a thick dust layer over the lava outcrop peaks.

Combined visible surface morphology analysis, thermophysical investigation, and thermal numerical modeling of the temperature curve can be used to quantify the horizontal mixing and vertical layering of dust, sand, and lava outcrops on lava flows in Daedalia Planum, Mars. This unique multi-instrument and modeling approach utilizes both remote sensing and predictive estimates to accurately derive surface properties in an area previously considered too dusty for thermal studies. Results from this study also demonstrate that complex surfaces may be incorrectly assessed when modeling only layering or mixing. With this information, the spectral signatures of the exposed outcrops can now be specifically targeted and separated from the sand and dust in low-lying areas. These spectral results are expected to constrain any compositional changes between flows and variations in the emplacement process over time. This method also has applications to other less explored sites on Mars considered too dust-covered.

## **5.6 Acknowledgements**

This research was supported through continuing funding of an original Mars Odyssey Participating Scientist Program project (grant number: NMO710630) and a NASA Earth and Space Science Fellowship (award number: 80NSSC17K0460). All data discussed in this paper are available in the cited references. THEMIS data are publicly available at the ASU Mars Image Explorer (<https://viewer.mars.asu.edu>) and CTX and HiRISE data are publically available from

the NASA Planetary Data System (<https://pds.nasa.gov>). The author would also like to acknowledge the seminal work of the late Josh Bandfield on both the THEMIS data calibration and modeling of RMS surface roughness on Mars. His planetary intellect and insights will be missed.

## **6.0 Concluding Remarks**

A multi-instrument and multispectral approach was used to investigate the effects of complex surfaces below the spatial resolution of thermal infrared instrumentation (at the subpixel level). These studies focus on 1) identifying pixels affected by significant shadowing at the time of ASTER collection (at both the pixel and subpixel scale) and deriving an areal percentage correction to those pixels, 2) identifying different particles sizes using WorldView-2 data to address the uniform material assumption at the pixel scale of ASTER TIR data and developing an improved understanding of the relationship between ATI values and mixed pixels, 3) developing a method to quantify the thermophysical variation between lava flows in an area considered too dusty for analysis and identifying surfaces with significant portions of lava outcrops, and 4) modeling the horizontal mixing and vertical layering of dust, sand, and lava outcrops on the surface of lava flows to identify the thickness of dust over potentially exposed lava outcrops. The studies of the North Coulee of the Mono-Inyo Crater system provide important corrections and improvements to significant complications that affect lower spatial resolution TIR data (compared with VIS data resolutions) and can hinder the accurate derivation of surface properties from these datasets.

With the use of a multi-instrument approach with different spatial and spectral resolutions, complex surfaces can be investigated for any complications from shadowing or mixed pixels. For thermal inertia measurements that represent the resistance of a material to changes in temperature over time, shadows will lower the maximum daytime temperature reached by a material and thus artificially raise the calculated ATI value. This is particular detrimental to studies of hazardous or difficult to reach areas if a significant portion of the scene

cannot be analyzed due to shadows cast from topographic variations. By utilizing hillshade calculations derived from a DEM, these shadowed areas can be identified remotely and pixels corrected based on the areal percentage of shadowing within each pixel. The maximum correction for the daytime temperature and albedo data was calculated from statistical analysis of north and south facing slopes that contain similar particle and block size distributions and thus should display a similar ATI value. Results demonstrated that with the use of higher spatial resolution DEMs, the complications of shadowing on remote sensing datasets can be corrected for, allowing for complete analysis of a study area. This is an important improvement for thermal hazard studies of areas affecting local populations. Furthermore, this method can be applied to planetary studies to investigate highly variable topographic regions affected by shadowing, particularly with limited orbital collection opportunities.

Another significant complication to thermal infrared data is the assumption of pure pixels on the surface with uniform material properties at the pixel scale. Analysis of higher spatial resolution data reveals that the surfaces are significantly more complex with varying mixtures of different particle and block sizes with significantly different thermal inertia responses. With the advancement in technology, it is important to understand how different mixtures of particle and block sizes can display the same thermal inertia value and determine whether or not these mixtures can be identified remotely. ASTER data were used to calculate the ATI over the study area and WorldView-2 and the photogrammetry datasets were used to define the particle and block size distribution on the surface of the North Coulee. Comparison the ATI values and particle and block size distributions revealed distinct correlations between datasets. Fine particle sizes dominate the lower portion of the ATI range and the highest values contained predominately moderate sizes. This suggests that pixels covering the coarse areas do not solely



represent the signature of the large block material and likely contain exposed fine or moderate material. Furthermore, moderate materials are aligned on the surface to create an inverse size grading that allows for smaller particles to settle beneath in empty pockets. These results demonstrated that the use of the current assumption of uniform material at the pixel scale will cause incorrect derivation of moderate and coarse size materials in the higher range of ATI values. Thus, intermediate ATI values are the most affected by the mixed pixel problem with the presence of different particle and block sizes. This technique demonstrates that through the use of multiple datasets at different spatial scales, the surface properties can be constrained and better understood.

With the increasing amount of data collected from orbital and ground-based instruments (with different specifications), it is important to understand the effect of spatial scale on data interpretation and the use of multiple datasets to correct possible analytical weaknesses present by using just one dataset. The analysis of ASTER, WorldView-2, and point cloud data built upon this hypothesis by providing layers of validation and an understanding of spatial scale in relation to a study. Point cloud density data produced from photographs collected during a field campaign validated the particle size categories defined using WorldView-2 data and also provided additional detail through a roughness calculation that is particularly sensitive to the scale of the study. By utilizing multiple spatial resolution datasets, an area may either be studied at different spatial scales or the detail of a lower resolution may be improved.

A major obstacle to thermal infrared studies of the Martian surface is the mantling by eolian material (e.g., dust and sand). The detection of coarse grained particles/rock outcrops are obscured by fine particles. However, if the fine particle sized upper layer is less than the optical thickness of the remote sensing instrumentation, the underlying bedrock signature can still be

present in the data. Thus, low TI regions like Daedalia Planum, may be explained by the horizontal mixing and vertical layering of larger lava outcrops and fine-grained material (dust or sand) in low-lying regions rather than a continuous layer of dust. Multiple visible and thermal infrared datasets, with both high spatial and spectral resolutions, were used to determine the cause of the thermophysical variation between individual flows in Daedalia Planum, Mars, which are most likely caused by different mixing relationships on the flow surfaces due to the homogenous composition and similar young ages of the flow field. Thermal infrared data from THEMIS were used to quantify the thermophysical response of each flow and assess the temperature diurnal response. Visible data from CTX and HiRISE were used to interpret the surface morphology and estimate the presence of minimally dust covered lava outcrops. This study demonstrated the presence of a complex relationship between the flow surface morphology and the vertical layering and/or horizontal mixing of sand, sand, and lava outcrops. Through this quantitative analysis, specific flows (category C rough flows with lower daytime temperatures, higher nighttime temperatures, and higher thermal inertias) were determined to contain the highest concentration of identifiable lava outcrops due to a thinner layer of dust compared with low-lying areas. This study demonstrated the distinct thermophysical variation between flows with smooth and rough surface morphology and the potential to determine the distribution of dust, sand, and lava outcrops on the surface. This thermophysical technique can also be applied to other dusty areas on Mars to identify target sites for detailed studies.

With the identification of the best flows to target for relatively exposed lava outcrops, a multi-method approach was developed to predict the diurnal temperature curves of different surface distributions using ideal components and matching the results with the temperatures derived from THEMIS data. To quantify the horizontal mixing and vertical layering of dust,

sand, and lava outcrops on the surface of these lava flows, thermal numerical models were used to predict the diurnal curves of different combinations of these components. The KRC thermal model (Kieffer, 2013) was used to calculate the diurnal and seasonal temperature curves of layered units using ideal material components of the same composition (basaltic), but with different particle sizes (dust, sand, and lava outcrops). These layered units consisted of dust over sand and dust over lava outcrop. An IDL code was written to horizontally mix the layered thermal model results based on different areal percentages of dust/sand and dust/lava outcrops. Once complete, these horizontally mixed layered diurnal temperature curve were compared with values derived from THEMIS daytime and nighttime temperature data to identify the degree of horizontal mixing and the thickness of the dust layering. Supervised classifications of visible data from HiRISE were used to estimate the exposed lava outcrop on the surface of the rough flows to provide further constraint on the possible areal percentages of dust, sand, and lava outcrops.

This method suggests that significantly less dust is present on the lava outcrops than previously thought. Comparison of the temperature values derived from THEMIS datasets, the classification analysis of lava outcrops in CTX and HiRISE data, and the horizontally mixed KRC layered runs demonstrate that the rough category C flows contain up to 40% lava outcrops on the surface with less than 0.2 mm of dust covering the outcrops. The thickness of the dust layer over the sand component is significantly higher than that covering the lava outcrops. The presence of a non-homogeneous layer of dust on the rough category C flows suggests the presence of winds in Daedalia Planum strong enough to significantly reduce the thickness of the dust cover on the lava outcrop peaks even though the low-lying sand regions of the flow surface remain covered. This multi-instrument remote sensing and modeling approach successfully

identified the horizontal mixing and vertical layering of dust, sand, and lava outcrops on these flow surfaces.

Using these methods, the spectral signatures of the partially exposed outcrops can now be specifically targeted and separated from the sand and dust in low-lying areas using a linear deconvolution approach on THEMIS emissivity data similar to Christensen et al. (2000) and Ramsey and Christensen (1998). These spectral results are expected to constrain any compositional changes between flows and variations in the emplacement process over time. Any variation identified in THEMIS emissivity spectra and the flow modeling may suggest ongoing changes at the time of the eruption such as increased partial melting or mixing magmatic sources of differing compositions.

These studies demonstrate the use of multi-instrument and multispectral approaches to investigating complex surfaces at a scale below the spatial resolution of thermal infrared datasets. With the use of both visible and thermal infrared datasets, the presence of mixed pixels (with different distributions of particle and block sizes) and shadowing was better understood and compensated for to accurately interpret the surface properties from remote sensing data. A combined method using thermal infrared and visible data along with thermal numerical modeling was used to identify areas on the surface with significant amounts of larger block sizes and quantify the horizontal mixing and vertical layering of dust, sand, and lava outcrops on lava flow surfaces in Daedalia Planum, Mars. These methods have applications to hazardous areas on Earth and other less explored sites on Mars considered too dust-covered.

## Appendix A

### Hillshade Data throughout the Day

This appendix includes additional hillshade data calculated at different times throughout the day of May 31, 2014 to understand the effect of shadows over a complete diurnal cycle.

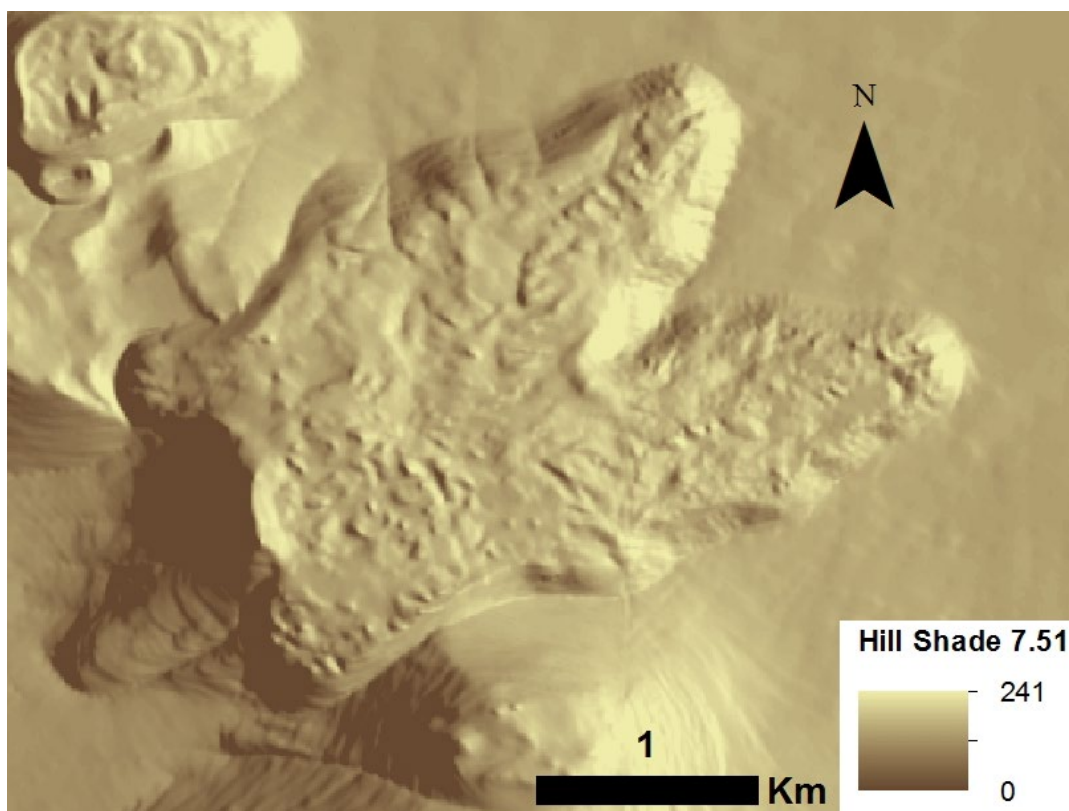


Figure 40. Hillshade calculated for 07:51 local time on May 31, 2014.

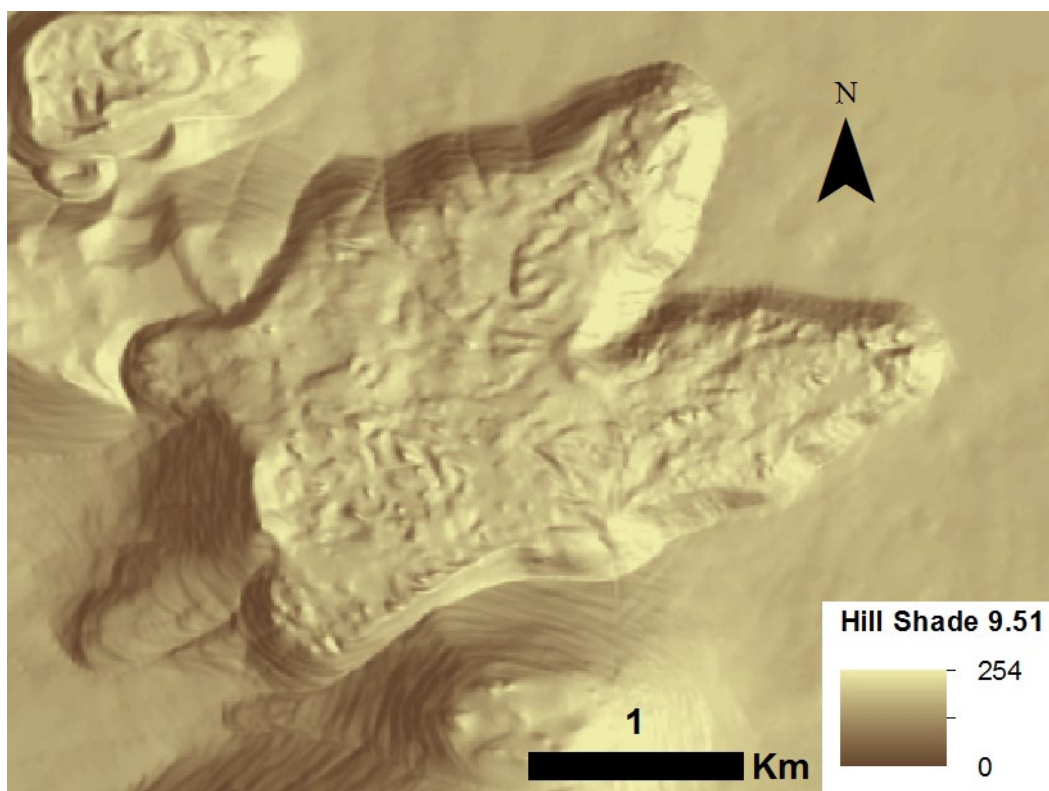


Figure 41. Hillshade calculated for 09:51 local time on May 31, 2014.

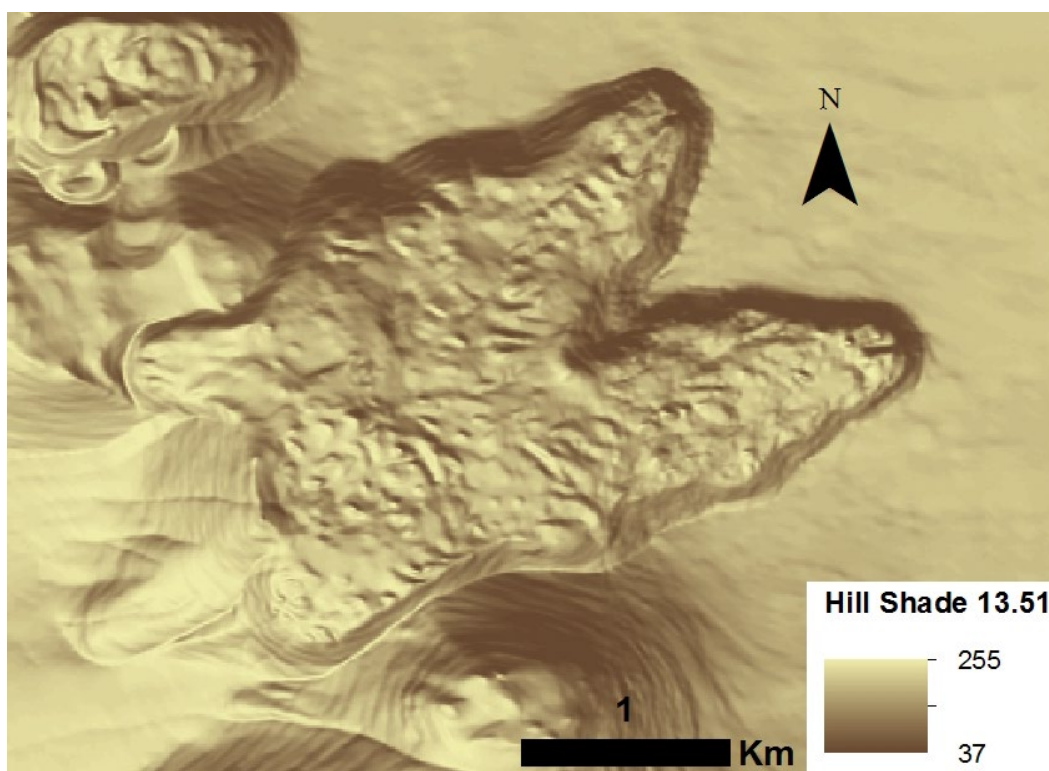


Figure 42. Hillshade calculated for 13:51 local time on May 31, 2014.



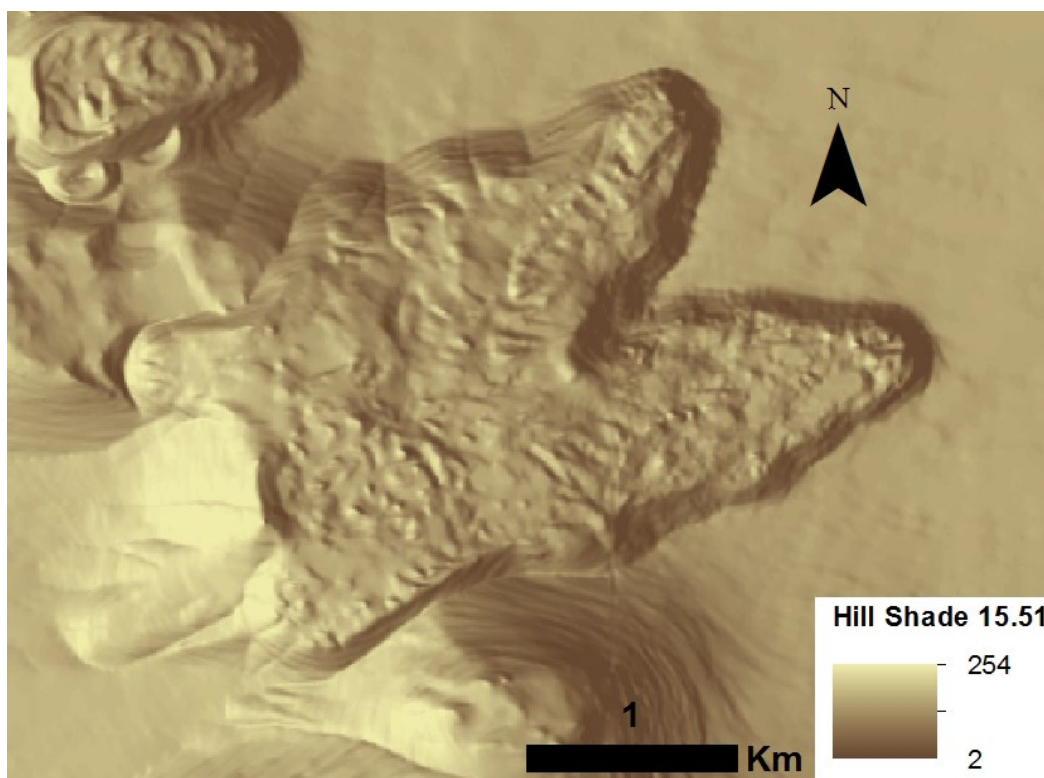


Figure 43. Hillshade calculated for 15:51 local time on May 31, 2014.

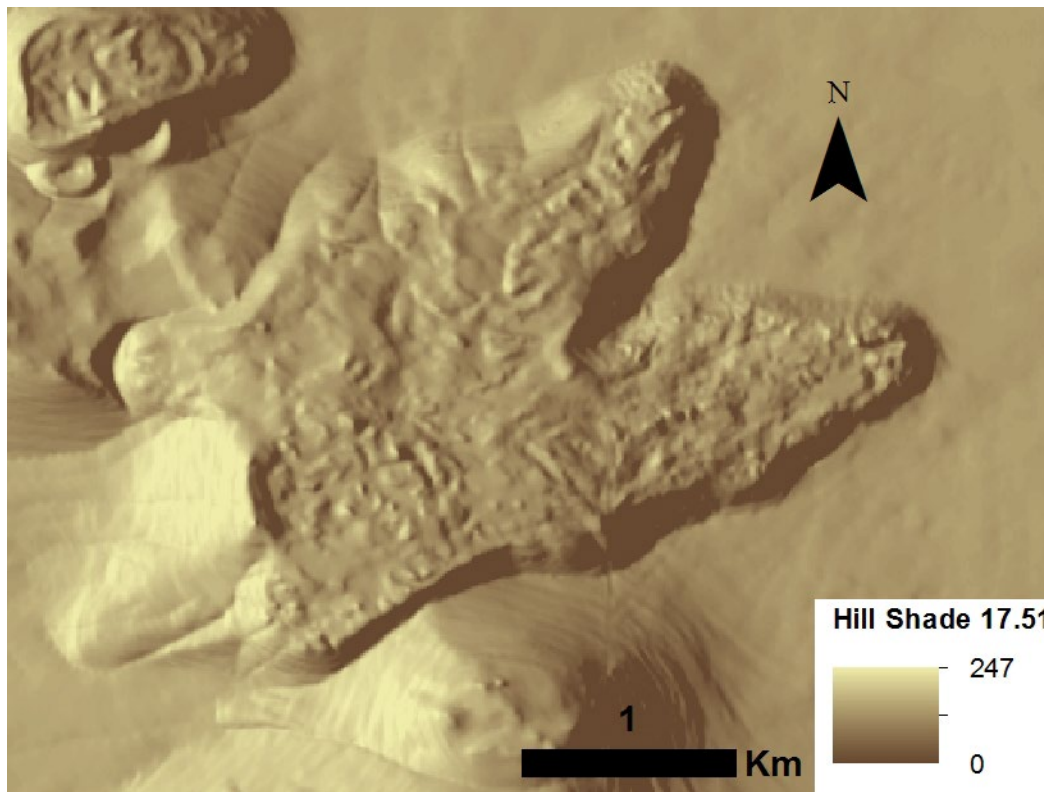


Figure 44. Hillshade calculated for 17:51 local time on May 31, 2014.

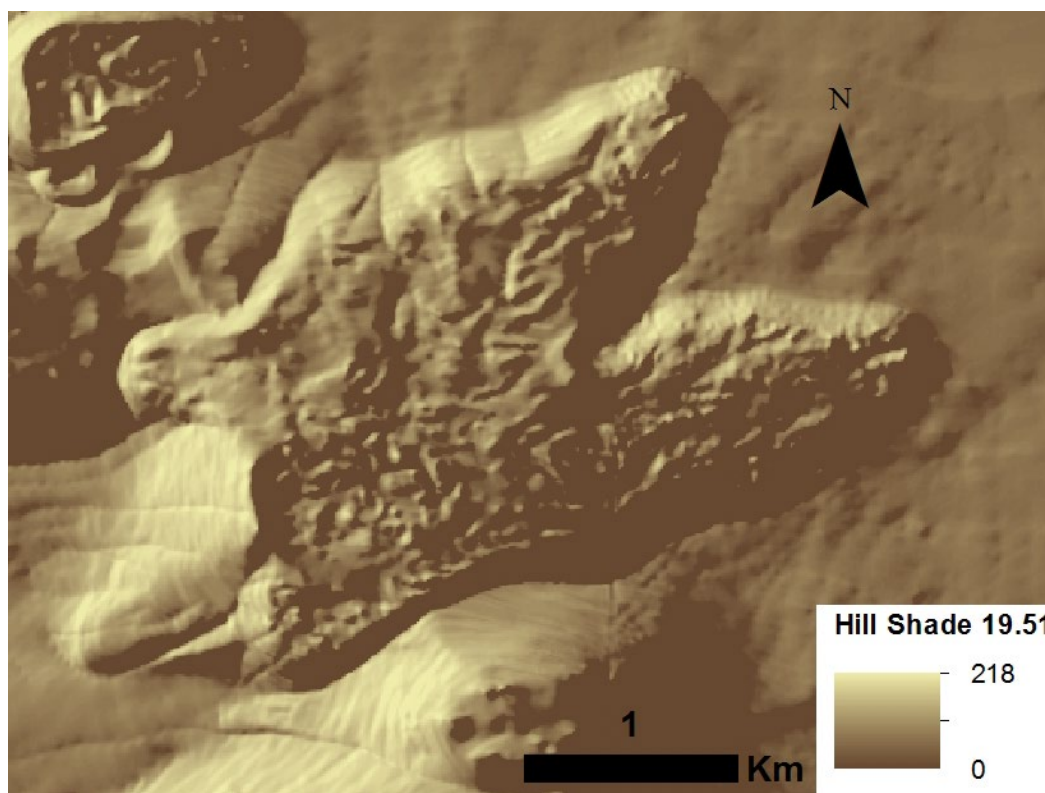


Figure 45. Hillshade calculated for 19:51 local time on May 31, 2014.



## Appendix B

### Varying Kernel Size for Roughness Calculation

To determine the appropriate kernel size for the roughness calculation, a range of values were applied from 0.102 m to 20 m. The following are the different kernel calculations.

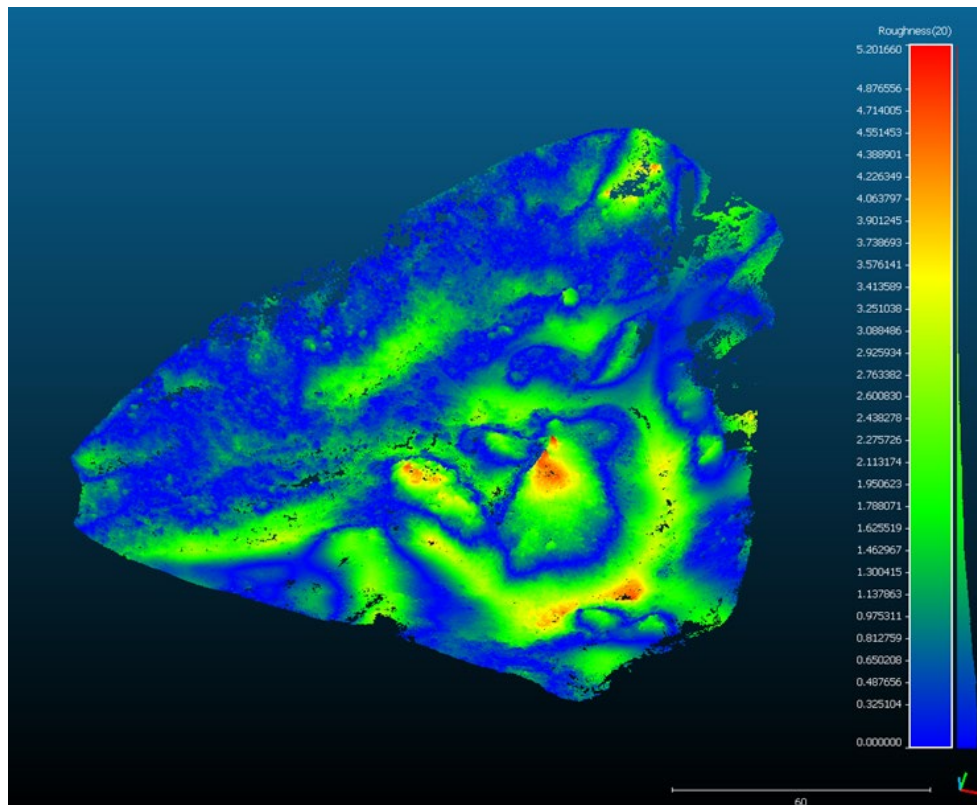


Figure 46. Kernel size 20 m roughness calculation.

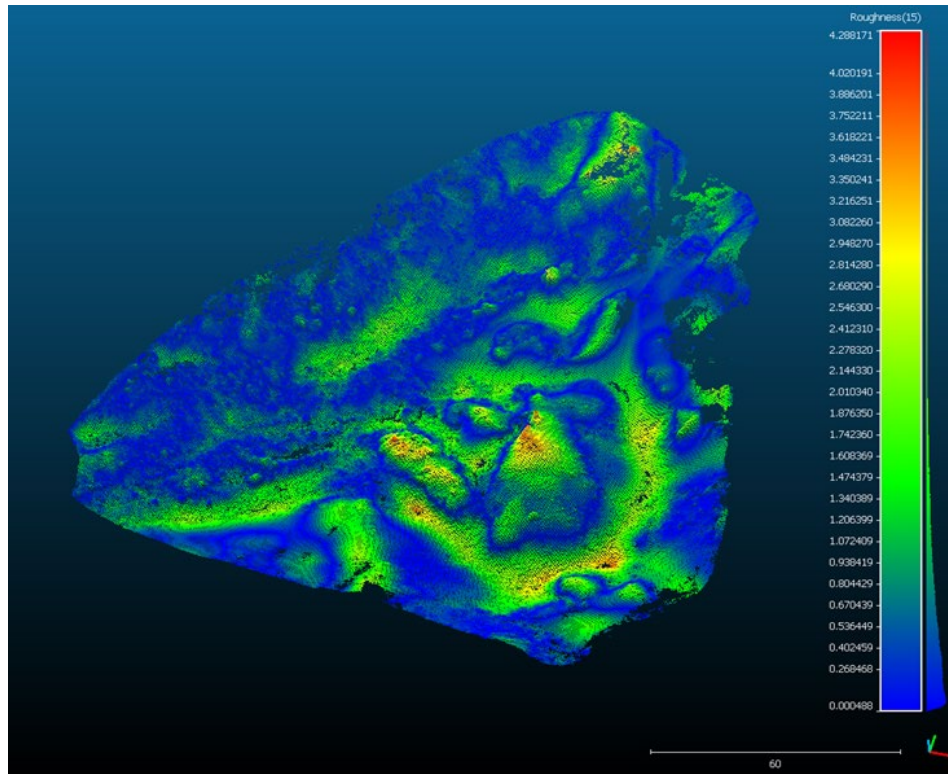


Figure 47. Kernel size 15 m roughness calculation.

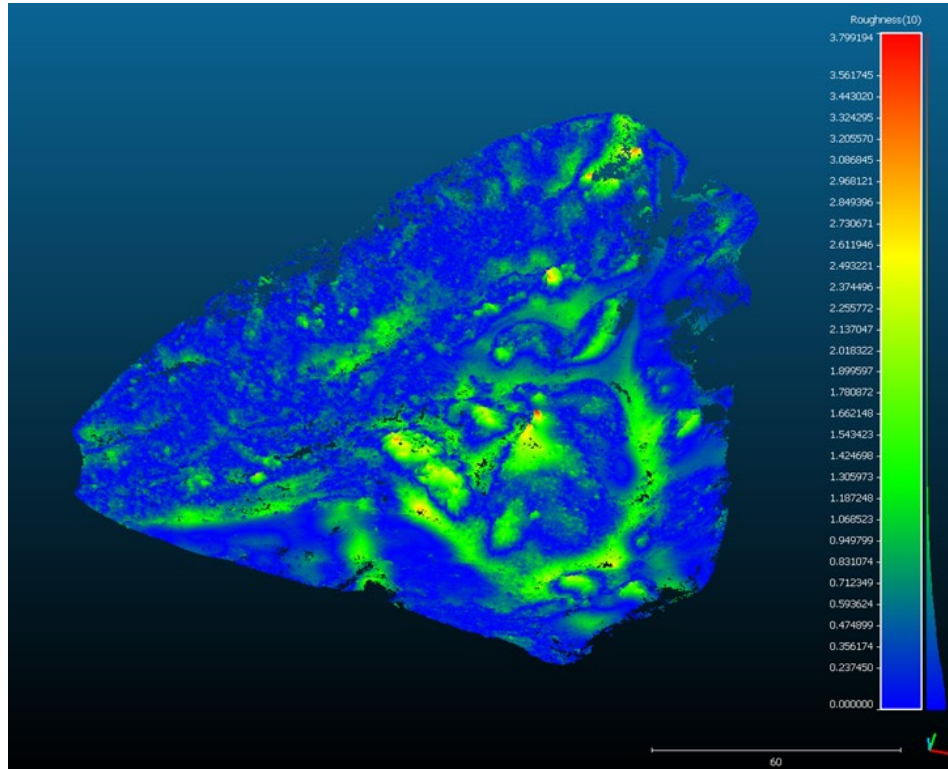


Figure 48. Kernel size 10 m roughness calculation.

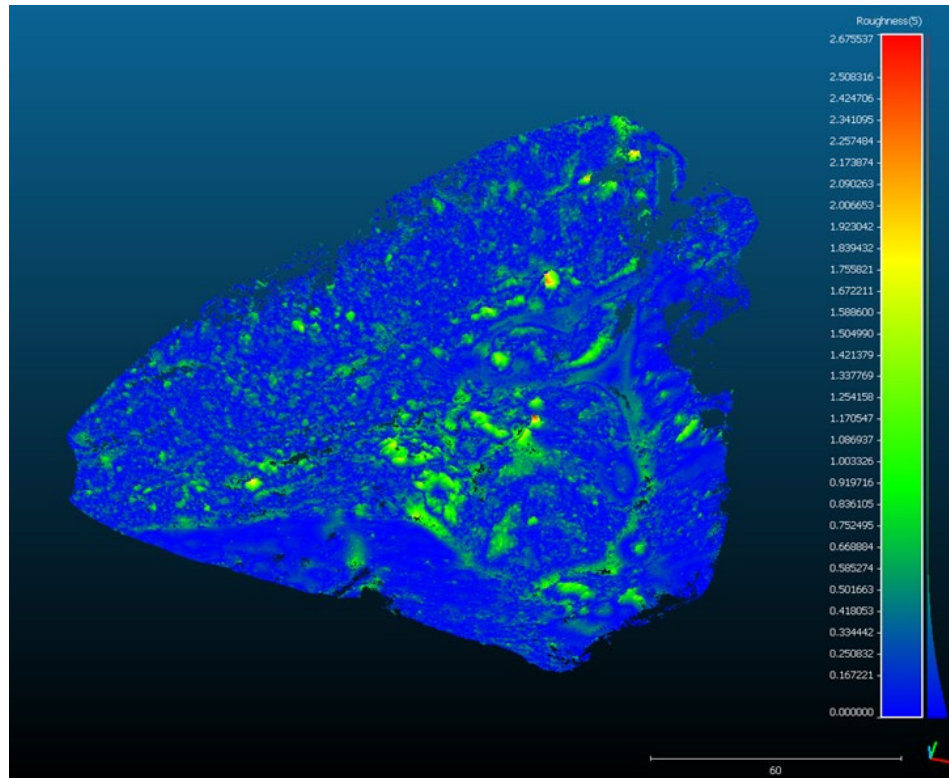


Figure 49. Kernel size 5 m roughness calculation.

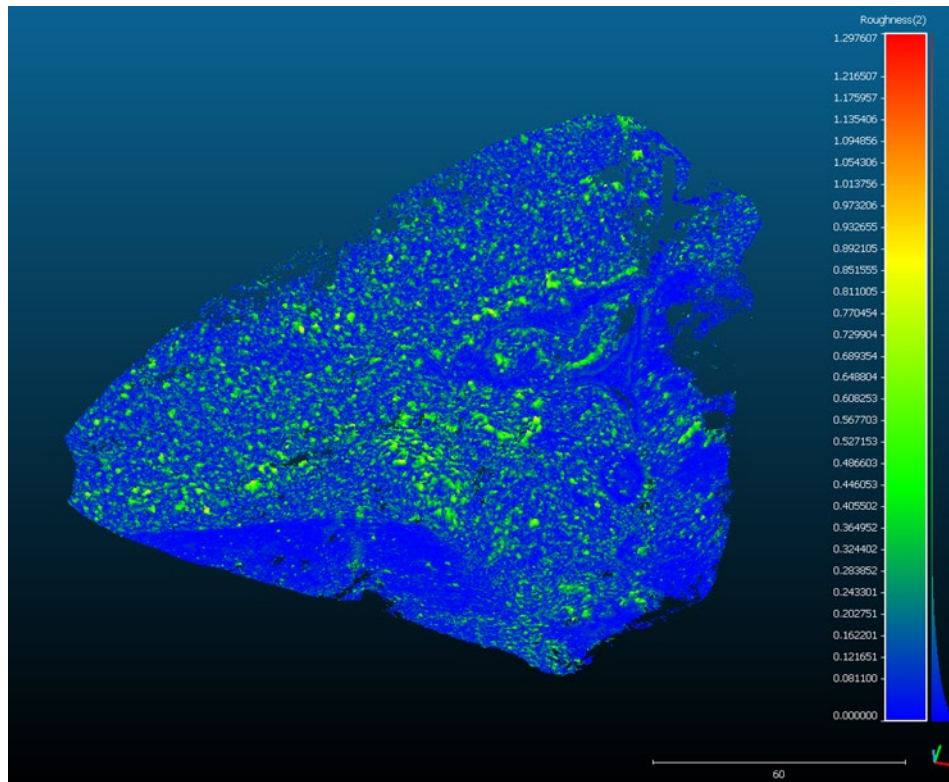


Figure 50. Kernel size 2 m roughness calculation.



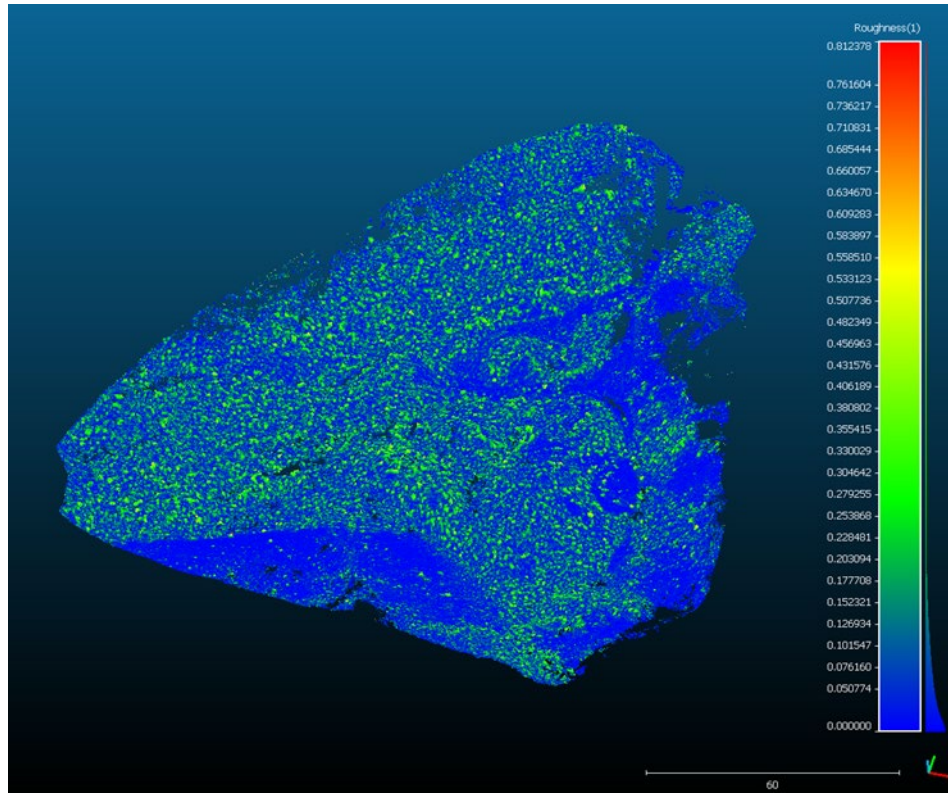


Figure 51. Kernel size 1 m roughness calculation.

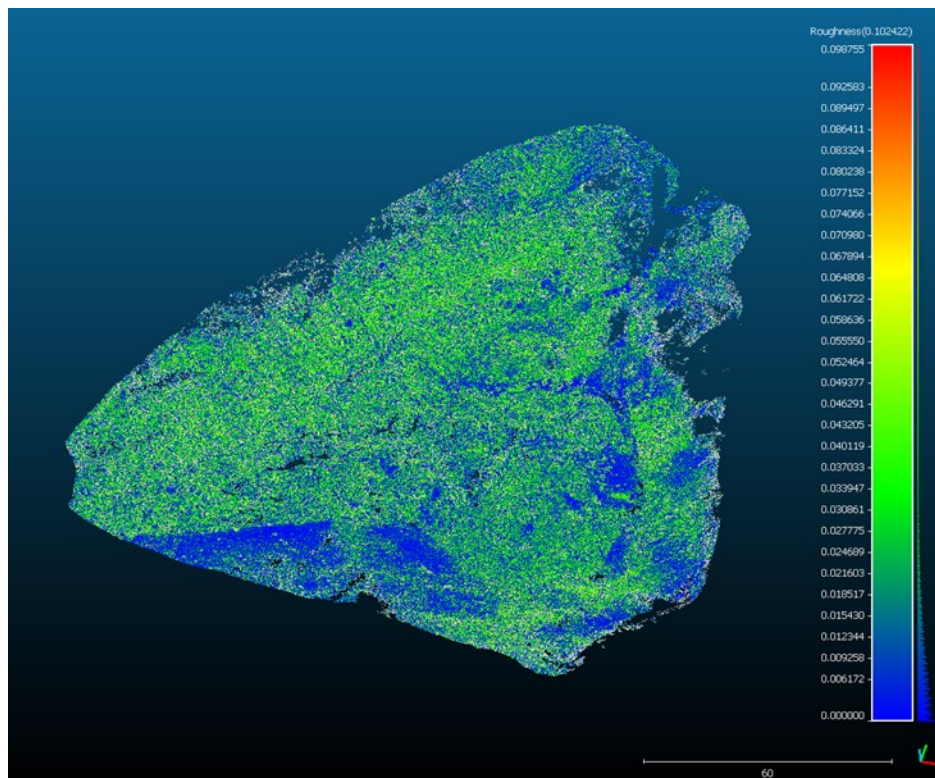


Figure 52. Kernel size 0.102422 m roughness calculation (the automatically assigned value).

## **Appendix C**

### **Daytime and Nighttime Category Assessment for Each Flow**

Statistical analysis of the ROIs placed on each lava flow identified in Daedalia Planum was used to determine the category of each flow. The following tables list the delta temperature ( $\Delta T$ ) value for every flow with every stamp analyzed and the assignment of either high or low compared to the flow field.

## C.1 Daytime High/Low Assignment and $\Delta T$

**Table 16. High/Low daytime temperature assignment for each flow in each THEMIS stamp with surface morphology and category descriptions.**

Day	1	2	3	4	5	6	7	8	9	10	11	12	13	14	15	16	17	18	19	20	21	22	23	24	25	26	27	28	29	30	31	32	33	34	35	36	37	38	39	40	41	42	43	
High/Low	H	H	L	L	L	L	L	L	H	L	L	L	L	L	L	L	L	L	L	L	L	L	L	L	L	L	L	L	L	L	H	H	H	H	L	L	L	L	L	L	L	H	L	
Morph. Category	S	S	R	R	R	R	R	R	S	R	R	R	R	R	S	R	R	S	R	R	S	S	R	R	R	R	R	R	R	S	S	R	R	R	R	R	R	R	R	R	S	R	R	S
	B	B	C	C	D	D	C	C	B	D	C	C	D	C	C	D	D	C	C	C	D	C	C	D	D	C	C	C	C	D	B	B	B	A	C	C	C	C	C	C	C	B	C	
I37594005	H		L																					L																				
I10328002	H		L																					L																				
I10640003	H		L																					L																				
I35460004	H	H	L		L			L																L	L																			
I52249005	H	H	L		L			L																L	L																			
I51712003	H	H	L		L			L																L	L																			
I45619003	H	H	L		L																			L		H																		
I43297003	H		L		L			L																	L																			
I46368002	H	H	L		L			L									L							L			L																	
I35822002	H	H	L		L	L		L						L	L										L																			
I07370003	H	H	L		L	L	L	L		L				L	L	L																												
I50688002	H	H	L		L	L	L	L		L				L	L	L	L				L																							
I51737003	H	H	L			L	L	L		L		L		L	L	L					L			L		L																		
I52274005	H	H	L			L	L	L		L		L		L	L	L					L			L	L																			
I37619002	H	H	L			L				L		L	L			L	L				L			L		L																		
I10665002	H	H	L			L		L	H	L		L	L	L		L	L	L	L	L		L	L		L		L																	
I47117003	H		L					L	H	L	L	L	L		L	L	L	L	L	L		L	L		L		L																	
I45644003			L					L	H	L	L	L	L				L		L	L																								
I37332002			L					L	H	L	L	L	L				L		L	L		L	L		L		L																	
I35485003			L	L				L	H	L	L	L	L				L	L	L	L		L	L		L		L																	
I50713002	H		L	L				L	H	L	L	L	L		L			L	L	L		L	L		L		L																	
I51225003																																												
I24168003																																												
I51762004				L					H		L	L			L			L	L	L		L	L																					
I40252004	H		L	L							L	L			L			L	L	L		L	L																					
I52299002	H			L					H		L	L						L	L	L		L	L					L		L														
I40851003									H		L	L						L	L	L		L	L					L		L														
I49764002				L					H		L	L							L	L	L		L	L					L		L													
I35847004				L					H		L									L		L							L	L	L													
I37045005				L					H		L																			L	L	L												
I36446003				L					H		L										L																							
I10066002																																												
I47142005																																												
I51250002																																												
I52836005																																												
I51787003																																												
I51837003																																												
I51862002																																												
I51887003																																												
I51912003																																												
I59103002																																												

**Table 17. Daytime  $\Delta T$  for each flow in each THEMIS stamp with surface morphology and category descriptions.**

Day	1	2	3	4	5	6	7	8	9	10	11	12	13	14	15	16	17	18	19	20	21	22	23	24	25	26	27	28	29	30	31	32	33	34	35	36	37	38	39	40	41	42	43	
Total	H	H	L	L	L	L	L	L	H	L	L	L	L	L	L	L	L	L	L	L	L	L	L	L	L	L	L	L	L	L	H	H	H	H	L	L	L	L	L	L	L	H	L	
Morph. Category	S	S	R	R	R	R	R	R	S	R	R	R	R	R	S	R	R	S	R	R	S	S	R	R	R	R	R	R	R	S	S	R	R	R	R	R	R	R	R	R	S	S		
I37594005	1.15		-1.84																					-2.67																				
I10328002	0.57		-2.76																					-4.35																				
I10640003	1.40		-2.66																					-4.63																				
I35460004	1.31	0.32	-1.32		-1.90		-0.83																	-1.13	-0.49																			
I52249005	1.53	1.11	-2.27		-2.48		-1.67																	-3.69	-0.53																			
I51712003	1.85	0.76	-2.48		-2.37		-2.87																	-3.84	-1.94																			
I45619003	1.85	0.75	-1.81		-2.59																			-2.09																				
I43297003	0.24		-2.01		-2.12		-1.00			-1.18														-1.27		-1.14																		
I46368002	1.48	1.51	-2.01		-2.68		-0.48			-3.18					-0.16									-3.35		-0.33																		
I35822002	0.07	0.43	-1.98		-2.17	-0.93	-0.92			-1.66				-0.70	-0.41	-1.01											-0.87																	
I07370003	1.59	1.60	-1.38		-2.67	-1.33	-2.45	-2.08		-5.71				-3.10	-2.71	-4.62																												
I50688002	0.54	0.33	-1.73		-2.61	-0.66	-1.95	-1.43		-2.61				-2.37	-2.26	-2.57	-2.30			-2.73																								
I51737003	0.76	1.22	-1.01		-0.16	-0.70	-0.95			-2.51		-1.07		-1.64	-1.32	-2.19	-1.92			-3.17				-1.58		-2.54																		
I52274005	1.14	1.46	-1.13		-0.41	-0.37	-0.87			-3.31		-1.10		-1.38	-0.85	-2.75	-2.51			-4.24				-1.51		-3.16																		
I37619002	0.97	1.58	-0.83		-0.50					-1.72		-0.09	-1.47			-0.66	-0.85			-2.32				-0.03		-1.52																		
I10665002	1.24	1.89	-0.55		-0.13		-0.63	1.27	-3.03	-0.45	-2.65	-0.36			-2.08	-1.98	-0.14	-1.26	-4.22				-0.13	-0.52		-2.82																		
I47117003	0.85		-0.99				-0.12	1.74	-2.26	-2.24	-0.07	-2.39			-0.28	-2.51	-1.93	-0.30	-0.98	-3.80			-0.19	-1.05		-2.93																		
I45644003	0.13		-1.71				-0.01	1.81	-1.12	-1.65		-1.55				-0.03	-0.38	-2.35																										
I37332002			-1.88				-0.91	1.18	-1.64	-2.16	-0.76	-1.81				-0.59	-0.03	-1.03	-2.78				-0.07	-0.46		-1.32																		
I35485003			-1.72	-0.05			-0.91	0.83	-1.21	-1.85	-1.24	-1.60				-1.49	-0.85	-1.43	-2.34		-1.09	-1.11	-1.88		-1.75																			
I50713002	0.16		-1.54	-1.03			-1.50	0.01	-2.00	-2.35	-1.69	-2.41			-2.00			-1.77	-1.89	-2.79	-1.87	-1.99	-2.81		-2.80																			
I51225003			-2.09	-1.63			-2.20	0.49	-2.55	-3.24	-2.34	-3.06			-2.11			-2.26	-2.53	-3.75	-2.66	-2.59	-3.45																					
I24168003			-1.16	-2.31				0.82	-3.33	-3.48	-2.14	-4.48			-2.56			-3.03	-3.14	-5.59	-2.25	-3.11	-3.82																					
I51762004			-0.10				1.59		-1.44	-0.20					-0.10			-0.68	-0.95	-2.34	-0.19	-0.68																						
I40252004	0.12		-1.66	-2.07					-3.58	-2.02					-2.50			-2.73	-2.80	-4.47	-2.07	-2.62																						
I52299002	0.46		-0.95				0.93		-2.25	-0.53								-0.93	-1.30	-3.17	-0.12	-0.63																						
I40851003			0.22				1.31		-1.41	-0.77								-1.66	-3.02	-0.96	-2.46																							
I49764002			-0.03				1.27		-1.28	-0.85									-1.13	-2.32	-0.45	-1.31																						
I35847004			-0.33				0.96		-1.43										-2.20			-0.24																						
I37045005			-0.60				0.94		-1.34										-2.15																									
I36446003			-0.38				1.12		-1.37										-1.89																									
I10066002																																												
I47142005																																												
I51250002																																												
I52836005																																												
I51787003																																												
I51837003																																												
I51862002																																												
I51887003																																												
I51912003																																												
I59103002																																												

## C.2 Nighttime High/Low Assignment and $\Delta T$

**Table 18. High/Low nighttime temperature assignment for each flow in each THEMIS stamp with surface morphology and category descriptions.**

Night	1	2	3	4	5	6	7	8	9	10	11	12	13	14	15	16	17	18	19	20	21	22	23	24	25	26	27	28	29	30	31	32	33	34	35	36	37	38	39	40	41	42	43	
Total	L	L	H	H	L	L	H	H	L	L	H	H	L	H	H	L	L	H	H	L	H	H	H	L	L	H	H	H	H	L	L	L	L	H	H	H	H	H	H	H	H	L	H	
Morph. Category	S	S	R	R	R	R	R	R	S	R	R	R	R	R	S	R	R	S	R	R	S	S	R	R	R	R	R	R	R	S	S	R	R	R	R	R	R	R	R	S	R	R	S	
I04742005	B	B	C	C	D	D	C	C	B	D	C	C	D	C	C	D	D	C	C	D	C	C	C	D	D	C	C	C	C	D	B	B	B	A	C	C	C	C	C	C	C	B	C	
I26258019	L		H				H			L														L		H																		
I05491009	L						H			L														L		H																		
I31411002	L		H				H			L														L		H																		
I31648008	L	L	H		L					L				H	H	L	L							L																				
I27718004	L	L	H				H			L				H	H	L	L				L			L																				
I13092002	L	L	H		L		H			L				H	H	L	L				L																							
I25971011	L		H		L		H			L				H	H	L							H		L																			
I31885004	L	L	H		L		H			L				H	H	L	L				L																							
I05878006	L	L	H			L	H	H		L				H	H	L	L				L					L																		
I04767002	L	L	H			L	H	H					H		H			H	H				H			L																		
I18321003	L	L	H			L	H	H	L	L		H			H	L	L	H	H	L			H	H		L																		
I08100019		L	H			L	H		L	L	H	H	L		H		L	H	H	L			H	H		L																		
I08487010	L		H			L		H	L	L	H	H	L		H			H	H	L			H	H																				
I06627006	L		H			L	H		L	L	H	H	L		H			H	H	L			H	H																				
I18633011	L	L	H					H	L			H	H					H	H																									
I09423011			H						L	L	H	H						H	H	L																								
I29178002	L		H				H	L	L	L	H	H							H																									
I14340006	L		H	H					L		H	H							H																									
I28030002	L		H	H					L		H	H							H																									
I52280002																																												
I53791002																																												
I27743004	L		H						L		H																																	
I07014012	L		H	H					L		H																																	
I54790005																																												
I51818006																																												



**Table 19. Nighttime  $\Delta T$  for each flow in each THEMIS stamp with surface morphology and category descriptions.**

[illegible]

## **Appendix D**

### **Location and Collection Information for THEMIS Stamps**

The following table provides the location and collection information used in the MARSTHERM and KRC models to determine the diurnal and seasonal temperatures on the surface.

## THEMIS Stamp Information

**Table 20. THEMIS stamp information used to define the collection parameters used in the thermal numerical models.**

File ID	Center Lat (°)	Local Time	Orbit	Solar Long (°)	Mars Year	Incid. Angle	Center Long	North Azimuth	Emission Angle	Max Bright Temp	Min Bright Temp	Avg Surface Temp	Dust Opacity
I37594005	-23.14	16.01	37594	100.47	30	75.48	239.14	262.20	1.3071	223.62	194.56	211.91	0.17
I10328002	-24.11	16.38	10328	16.38	27	71.57	238.97	262.12	1.2690	232.50	211.91	223.79	0.05
I10640003	-30.12	16.51	10640	30.41	27	77.72	237.97	262.26	1.2853	221.62	196.48	214.87	0.02
I35460004	-23.38	15.08	35460	22.40	30	55.82	238.64	262.45	22.5489	248.55	235.57	241.76	0.04
I52249005	-24.24	16.30	52249	26.16	32	72.01	238.52	261.96	1.2767	230.34	216.18		
I51712003	-24.50	15.95	51712	5.11	32	63.29	238.46	261.97	1.3151	250.64	230.69		
I45619003	-25.71	16.07	45619	88.79	31	77.83	238.18	262.20	1.3070	216.75	182.77	204.37	
I43297003	-23.88	14.99	43297	2.35	31	50.09	238.34	262.15	16.9003	262.98	251.12	256.47	0.10
I46368002	-18.57	16.25	46368	116.57	31	74.54	239.06	262.15	1.3842	221.22	189.57	205.81	-0.01
I35822002	-23.81	15.44	35822	36.10	30	63.32	238.20	262.16	1.5845	238.28	223.76	230.99	0.06
I07370003	-27.92	17.06	7370	240.07	26	68.07	237.53	262.05	1.2986	269.27	255.65	258.72	0.27
I50688002	-23.86	15.57	50688	320.69	31	50.81	238.09	262.01	1.3407	277.53	264.77	268.61	0.17
I51737003	-23.24	15.97	51737	6.12	32	63.42	237.99	261.87	1.3088	251.15	230.17		
I52274005	-24.49	16.31	52274	27.11	32	72.49	237.80	261.97	1.3221	236.29	212.60		
I37619002	-23.73	16.01	37619	101.40	30	75.80	237.84	262.12	1.2835	226.30	195.46	209.67	0.04
I10665002	-25.57	16.55	10665	31.35	27	76.62	237.49	262.25	1.2871	231.63	197.84	215.77	0.02
I47117003	-25.06	16.39	47117	146.38	31	74.92	237.44	262.16	1.2913	243.49	207.52	223.94	0.08
I45644003	-23.37	16.08	45644	89.70	31	76.65	237.57	262.16	1.3857	219.43	190.64	206.31	
I36134004	-24.30	15.58	36134	47.61	30	67.51	237.41	262.17	1.3102	232.47	220.33	226.73	0.10
I37332002	-22.76	15.96	37332	90.79	30	74.95	237.61	262.19	1.3141	213.63	203.54	209.37	-0.02

I35485003	-22.53	15.10	35485	23.36	30	55.82	237.56	262.52	22.5492	248.04	238.16	242.97	0.06
I50713002	-23.70	15.57	50713	321.85	31	50.96	237.40	261.91	1.3368	277.49	265.76	268.41	0.17
I51225003	-24.37	15.69	51225	344.77	31	55.95	237.26	261.96	1.2722	266.31	250.36		
I24168003	-28.38	17.25	24168	245.81	28	69.97	236.67	262.19	1.2768	271.08	250.31	256.17	0.26
I51762004	-24.44	15.98	51762	7.12	32	64.09	237.17	261.89	1.3336	245.69	228.71		
I40252004	-25.17	16.31	40252	214.75	30	61.31	237.06	252.20	1.3092	273.75	255.23	261.70	0.13
I52299002	-25.52	16.33	52299	28.06	32	73.21	236.98	261.99	1.3029	240.38	202.21		
I40851003	-22.42	15.96	40851	245.65	30	54.45	237.30	262.20	1.3452	274.06	263.54	266.97	0.26
I49764002	-23.44	15.94	49764	275.17	31	53.47	237.14	261.98	1.3853	279.96	271.20	273.92	0.16
I35847004	-23.43	15.45	35847	37.03	30	63.48	237.03	262.16	1.6591	233.43	224.98	229.34	0.05
I37045005	-23.84	15.89	37045	80.49	30	74.62	236.94	262.22	1.2687	216.01	205.23	211.33	0.05
I36446003	-24.03	15.71	36446	58.94	30	70.65	236.84	262.28	1.3510	232.47	193.68	218.17	0.07
I10066002	-24.05	16.26	10066	8.13	27	67.89	236.81	262.64	1.2768	246.00	219.18	232.96	0.11
I47142005	-26.29	16.39	47142	147.43	31	75.22	236.41	262.13	1.2346	235.98	202.50	223.02	0.06
I51250002	-24.03	15.71	51250	345.85	31	56.25	236.64	261.83	1.3011	264.39	247.93		
I52836005	-25.27	16.67	52836	48.01	32	80.97	236.41	261.94	1.3128	217.74	189.64	208.81	0.12
I51787003	-24.29	16.00	51787	8.13	32	64.47	236.55	261.89	1.3219	240.15	217.79		
I59652002	-23.98	17.42	59652	348.27	32	79.98	235.49	261.88	1.3060	223.05	209.12	218.05	-0.03
I51837003	-24.05	16.03	51837	10.12	32	65.24	235.31	261.87	1.2893	242.47	230.10		
I51862002	-25.86	16.04	51862	11.12	32	66.10	234.41	261.90	1.2770	239.77	226.14		
I51887003	-26.50	16.05	51887	12.11	32	66.69	233.67	261.89	1.2637	239.79	228.85		
I51912003	-27.31	16.06	51912	13.10	32	67.34	232.90	261.89	1.2417	241.39	227.13		
I59103002	-26.12	17.23	59103	323.88	32	73.43	232.59	261.95	1.3199	250.21	230.42	241.90	0.20
I51937003	-27.38	16.08	51937	14.08	32	67.79	232.24	261.89	1.2958	244.13	222.43		
I51962005	-27.30	16.10	51962	15.07	32	68.19	231.60	261.92	1.2934	241.06	228.09		

## Appendix E

### Horizontally Mixing Layered KRC Runs

The following code was written in IDL to horizontally mix the KRC layered thermal model runs based on a linear mixture with defined percentages.

#### IDL code

```
;-----  
;Horizontal Mixture of KRC Layered Diurnal and Seasonal Cycles  
;PRO krc_integration  
;-----  
;IDL code written by Christine Simurda  
;3/17/18  
;-----  
  
;close all variables  
close, /all  
  
;Read in files  
file1 = dialog_pickfile(path='Z:\csimurda\Mixed Models\Krc  
Runs', FILTER='*.txt',TITLE='Select Component 1 File')  
temp1 = read_ascii(file1, delimiter=',')  
temp1 = temp1.field01 ;to eliminate field binning and changing  
variables from string to float  
  
;determine the location of and then extract the file name for  
output filename of temp1  
posfile1 = strpos(file1, '.txt')
```

```

subfile1 = strmid(file1, posfile1-8, 8)

file2 = dialog_pickfile(path='Z:\csimurda\Mixed Models\Krc
Runs', FILTER='*.txt',TITLE='Select Component 2 File')
temp2 = read_ascii(file2, delimiter=',')
temp2 = temp2.field01 ;to eliminate field binning and changing
variables from string to float

;determine the location of and then extract the file name for
output filename of temp 2
posfile2 = strpos(file2, '.txt')
subfile2 = strmid(file2, posfile2-8, 8)

;output file name
outputname = subfile1 + '_' + subfile2

;determine output file location
outputdir = strmid(file1, 0, posfile1-8) + outputname + '\\'
file_mkdir, outputdir
outputfilesav = outputdir + outputname + '.sav'
outputfiletxt = outputdir + outputname + '.txt'

;Define time for input into new array
time = dindgen(96, start=0.25, increment=0.25)

;Define areal percentages arrays
a1 = findgen(19, start =0.05, increment=0.05)
a2 = reverse(a1)

;Make an Open Array
result = fltarr(96, 20)

;Math OPERATIONS Note=Do not use uppercases
For i=0, 95 do begin
    For j=0, 18 do begin
        result(i,j+1)=((a1(j)*(temp1(i)^4)) +
(a2(j)*(temp2(i)^4)))^(0.25)
    Endfor
Endfor

;Fill in time row
result(*,0) = time

;Plot
for k=0, 18 do begin

```

```

w=strcmp(trim(string(round(a1(k)*100))),1)+subfile1+'_'+strcmp(trim(string(round(a2(k)*100))),1)+subfile2
    p = plot(result(:,0), result(:,k+1), xrange=[0,24],
yrange=[150,270], window_title=w, ylabel='Brightness Temperature (K)', xtitle='Mars Hours', font_size=18)
    f = outputdir + w + '.png'
    p.save, f, border=30, resolution=300
    p.close
endfor

;save as idl variable
save, result, filename=outputfilesav

;save as text file (csv style)
openw, lun, outputfiletxt, /get_lun
printf, lun, result, FORMAT='(95(F8.3, :, ", "),F8.3)'
;printf, lun, result, FORMAT='(95(F8.3,1X),F8.3)'
free_lun, lun
close, /all

stop
END

```

## Bibliography

- Achauer, U., Greene, L., Evans, J. R., & Hato, H. M. (2010). The ASTER Global DEM. *Photogrammetric Engineering and Remote Sensing*, 76, 344-348.
- Aguilar, M. A., del Mar Saldana, M., & Aguilar, F. J. (2014). Generation and Quality Assessment of Stereo-Extracted DSM From GeoEye-1 and WorldView-2 Imagery. *IEEE Transactions on Geoscience and Remote Sensing*, 52(2), 1259-1271. <https://doi.org/10.1109/TGRS.2013.2249521>.
- Arvidson, R., Adams, D., Bonfiglio, G., Christensen, P., Cull, S., Golombek, M., Guinn, J., Guinness, E., Heet, T., Kirk, R., Knudson, A., Malin, M., McEwen, A., Mushkin, A., Parker, T., Seelos IV, F., Seelos, K., Smith, P., Spencer, D., Stein, T., & Tamppari, L. (2008). Mars Exploration Program 2009 Phoenix Landing Site Selection and Characteristics. *Journal of Geophysical Research: Planets*, 113, (E12). <https://doi.org/10.1029/2007JE003021>.
- Bailey, R. A. (1989). *Quaternary Volcanism of Long Valley Caldera, Mono-Inyo Craters Volcanic Chain, and Vicinity, Eastern California: Field Trip Guidebook T313*. Washington, DC: American Geophysical Union.
- Bailey, R. A., Dalrymple, G. B., & Lanphere, M. A. (1976). Volcanism, Structure, and Geochronology of Long Valley Caldera, Mono County, California. *Journal of Geophysical Research*, 81(5), 725-44.
- Bandfield, J. L. (2009). Effects of Surface Roughness and Graybody Emissivity on Martian Thermal Infrared Spectra. *Icarus*, 202(2), 414-428. <https://doi.org/10.1016/j.icarus.2009.03.031>.
- Bandfield, J. L., Rogers, D., Smith, M. D., & Christensen, P. R. (2004). Atmospheric Correction and Surface Spectral Unit Mapping using Thermal Emission Imaging System Data. *Journal of Geophysical Research: Planets*, 109, E10008. <https://doi.org/10.1029/2004JE002289>.
- Bemis, S. P., Micklethwaite, S., Turner, D., James, M. R., Akciz, S., Thiele, S. T., & Bangash, H. A. (2014). Ground-based and UAV-Based Photogrammetry: A Multi-scale, High-Resolution Mapping Tool for Structural Geology and Paleoseismology. *Journal of Structural Geology*, 69(A), 163-178.
- Birdseye, C. H. (1940). Stereoscopic Photographic Mapping. *Annual Association of American Geographers*, 30, 1-24. <https://doi.org/10.1080/00045604009357193>.
- Bleacher, J. E., Greeley, R., Williams, D. A., Cave, S. R., & Neukum, G. (2007). Trends in Effusive Style at the Tharsis Montes, Mars, and Implications for the Development of the



- Tharsis Province. *Journal of Geophysical Research: Planets*, 112, E09005. <https://doi.org/10.1029/2006JE002873>.
- Bursik, M., & Sieh, K. (1989). Range Front Faulting and Volcanism in the Mono Basin, Eastern California. *Journal of Geophysical Research*, 94(B11), 15587-5609.
- Campbell, B. A., Ghent, R. R., & Shepard, M. K. (2003). Limits on Inference of Mars Small-Scale Topography from MOLA Data. *Geophysical Research Letters*, 30(3), 1116. <https://doi.org/10.1029/2002GL016550>.
- Chandler, J. H., Ashmore, P., Paola, C., Gooch, M., & Varkaris, F. (2002). Monitoring River-Channel Change Using Terrestrial Oblique Digital Imagery and Automated Digital Photogrammetry. *Annals of the Association of American Geographers*, 92(4), 631-644.
- Chen, Y., Smith, P. E., Eversen, N. M., York, D., & Lajoie, K. R. (1996). The Edge of Time: Dating Young Volcanic Ash Layers with the  $^{40}\text{Ar}$ - $^{39}\text{Ar}$  Laser Probe. *Science*, 274, 1176-1178.
- Choodarathnakara, A. L., Kumar, T. A., Koliwad, S., & Patil, C. G. (2012). Mixed Pixels: A Challenge in Remote Sensing Data Classification for Improving Performance, *International Journal of Advanced Research in Computer Engineering & Technology*, 1(9), 261-271.
- Christensen, M. N., Gilbert, C. M., Lajoie, K. R., & Al-Rawi, Y. (1969). Geological-Geophysical Interpretation of Mono Basin, California-Nevada, *Journal of Geophysical Research*, 74(22), 5221-5239.
- Christensen, P.R., Bandfield, J.L., Smith, M.D., Hamilton, V. E., & Clark, R. N. (2000). Identification of a Basaltic Component on the Martian Surface from Thermal Emission Spectrometer Data. *Journal of Geophysical Research: Planets*, 105(E4), 2156-2202.
- Christensen, P.R., Bandfield, J. L., Hamilton, V. E., Ruff, S. W., Kieffer, H. H, Titus, T. N., Malin, M. C., Morris, R. V., Lane, M. D., Clark, R. L., Jakosky, B. M., Mellon, M. T., Pearl, J. C., Conrath, B. J., Smith, M. D., Clancy, R. T., Kuzmin, R. O., Roush, T., Mehall, G. L., Gorelick, N., Bender, K., Murray, K., Dason, S., Greene, E., Silverman, S., & Greenfield, M. (2001). The Mars Global Surveyor Thermal Emission Spectrometer Experiment: Investigation Description and Surface Science Results. *Journal of Geophysical Research: Planets*, 106(E10), 23823-23871. <https://doi.org/10.1029/2000JE001370>.
- Christensen, P. R., Bandfield, J. L., Bell III, J. F., Gorelick, N., Hamilton, V. E., Ivanov, A., Jakosky, B. M., Kieffer, H. H., Lane, M.D., Malin, M.C., McConnochie, T., McEwen, A. S., McSween Jr., H. Y., Mehall, G. L., Moersch, J E., Nealson, K. H., Rice Jr., J. W., Richardson, M. I., Ruff, S. W., Smith, M. D., Titus, T. N., & Wyatt, M. B. (2003). Morphology and Composition of the Surface of Mars: Mars Odyssey THEMIS Results. *Science*, 300(5628), 2056-2061. <https://doi.org/10.1126/science.1080885>.

- Christensen, P. R., Gorelick, N. S., Mehall, G. L., & Murray, K. C. (2008). *THEMIS Public Data Releases, Planetary Data System Node*. Arizona State University. <http://themis-data.asu.edu>.
- Christensen, P. R., Jakosky, B. M., Kieffer, H. H., Malin, M. C., Mcsween Jr., H. Y., Nealon, K., Mehall, G. L., Silverman, S. H., Ferry, S., Caplinger, M., & Ravine, M. (2004). The Thermal Emission Imaging System (THEMIS) for the Mars 2001 Odyssey Mission. *Space Science Reviews*, 110, 85-130. <https://doi.org/10.1023/B:SPAC.0000021008.16305.94>
- Christensen, P. R., McSween Jr., H. Y., Bandfield, J. L., Ruff, S. W., Rogers, A. D., Hamilton, V. E., Gorelick, N., Wyatt, M. B., Jakosky, B. M., Kieffer, H. H., Malin, M. C., & Moersch, J. E. (2005a). Evidence for Magmatic Evolution and Diversity on Mars from Infrared Observations. *Nature*, 436, 504-509.
- Christensen, P. R., Ruff, S. W., Ferguson, R., Gorelick, N., Jakosky, B. M., Lane, M. D., McEwen, A. S., McSween, H. Y., Mehall, G. L., Milam, K., Moersch, J. E., Pelkey, S. M., Rogers, A. D., & Wyatt, M. B. (2005b). Mars Exploration Rover Candidate Landing Sites as Viewed by THEMIS. *Icarus*, 176(1), 12-43. <https://doi.org/10.1016/j.icarus.2005.01.004>.
- Cracknell, A.P. & Xue, Y. (1996). Thermal Inertia Determination from Space - A Tutorial Review. *International Journal of Remote Sensing*, 17, 431-461.
- Craddock, M. A., & Craddock, R. A. (2006). Thermal Conductivity Measurements of Particulate Materials: 3. Natural Samples and Mixtures of Particle Sizes, *Journal of Geophysical Research*, 111, E09013. <https://doi.org/10.1029/2006JE002706>.
- Craddock, R.A., Greeley, R., & Christensen, P.R. (1990). Evidence for an Ancient Impact Basin in Daedalia Planum, Mars, *Journal of Geophysical Research*, 95(B7), 10729-10741.
- Crown, D. A., Berman, D. C., & Ramsey, M. S. (2015). *Lava Flow Fields of Southern Tharsis, Mars: Flow Types, Interactions, and Ages*. Paper presented at Lunar and Planetary Science Conference XLVI, Lunar and Planetary Institute, Houston. Abstract. #1349.
- Crown, D. A., Ramsey, M. S., & Berman, D. C. (2010). *Mapping Arsia Mons Lava Flow Fields: Insights into Flow Emplacement Processes and Flow Field Development*. Paper presented at Lunar and Planetary Science Conference XLI, Lunar and Planetary Institute, Houston. Abstract. #2225.
- Crown, D.A., & Ramsey, M.S. (2017). Morphologic and Thermophysical Characteristics of Lava Flows Southwest of Arsia Mons, Mars. *Journal of Volcanology and Geothermal Research*, 342, 13-28. <https://doi.org/10.1016/j.jvolgeores.2016.07.008>.
- Crumpler, L. S., Head, J. W., & Aubele, J. C. (1996). Calderas on Mars: Characteristics, Structure and Associated Flank Deformation. In W. J. McGuire, A. P. Jones, J. Neuberg (Eds.), *Volcano Instability on the Earth and Other Planets*, Geological Society of America Special Publication (Vol. 110, pp. 307-348).

- DigitalGlobe WorldView 2 data sheet. (2013). Retrieved February 2016, from DigitalGlobe. Accessed at: [http://global.digitalglobe.com/sites/default/files/DG\\_WorldView2\\_DS\\_PROD.pdf](http://global.digitalglobe.com/sites/default/files/DG_WorldView2_DS_PROD.pdf)
- Eckert, S. (2012). Improved Forest Biomass and Carbon Estimations Using Texture Measures from WorldView-2 Satellite Data. *Remote Sensing*, 4(4), 810-829. <https://doi.org/10.3390/rs4040810>.
- Edgett, K. S. & Lancaster, N. (1993). Volcaniclastic Aeolian Dunes: Terrestrial Examples and Application to Martian Sands. *Journal of Arid Environments*, 25(3), 271-297. <https://doi.org/10.1006/jare.1993.1061>.
- Edgett, K. S. & Malin, M. C. (2000). New Views of Mars Eolian Activity, Materials, and Surface Properties: Three Vignettes from the Mars Global Surveyor Mars Orbiter Camera. *Journal of Geophysical Research: Planets*, 105(E1), 1623-1650. <https://doi.org/10.1029/1999JE001152>.
- Edwards, C. S., Nowicki, K. J., Christensen, P. R., Hill, J., Gorelick, N., & Murray, K. (2011). Mosaicking of Global Planetary Image Datasets: 1. Techniques and Data Processing for Thermal Emission Imaging System (THEMIS) Multi-spectral Data. *Journal of Geophysical Research: Planets*, 116, E10008. <https://doi.org/10.1029/2010JE003755>.
- Ferguson, R. L., Christensen, P. R., & Kieffer, H. H. (2006). High Resolution Thermal Inertia Derived from the Thermal Emission Imaging System (THEMIS): Thermal Model and Applications. *Journal of Geophysical Research: Planets*, 111, E12004. <https://doi.org/10.1029/2006JE002735>.
- Foschi, P. G. (1994). A Geometric Approach to a Mixed Pixel Problem: Detecting Subpixel Woody Vegetation, *Remote Sensing of Environment*, 50(3), 317-327. [https://doi.org/10.1016/0034-4257\(94\)90081-7](https://doi.org/10.1016/0034-4257(94)90081-7).
- Frankel, K. L., & Dolan, J. F. (2007). Characterizing Arid Region Alluvial Fan Surface Roughness with Airborne Laser Swath Mapping Digital Topographic Data, *Journal of Geophysical Research: Earth Surface*, 112, F02025. <https://doi.org/10.1029/2006JF000644>.
- Garry, W. B., Williams, D. A., & Bleacher, J. E. (2014). *Geologic Mapping of Arsia and Pavonis Montes, Mars*. Paper presented at Lunar and Planetary Science Conference XLV, Lunar and Planetary Institute, Houston. Abstract #2133.
- Garry, W. B., Williams, D. A., Dapremont, A. M., & Shean, D. E. (2018). *The 1:1,000,000 Geologic Map of Arsia Mons, Mars*. Paper presented at Planetary Geologic Mappers Meeting 2018. Abstract #7028.
- Giacomini, L., Carli, C., Sgavetti, M., & Massironi, M. (2012). Spectral Analysis and Geological Mapping of the Daedalia Planum Lava Field (Mars) using OMEGA Data. *Icarus*, 220(2), 679-693. <https://doi.org/10.1016/j.icarus.2012.06.010>.

- Giacomini, L., Massironi, M., Martellato, E., Pasquare, G., Frigeri, A., & Cremonese, G. (2009). Inflated Flows on Daedalia Planum (Mars)? Clues from a Comparative Analysis with the Payen Volcanic Complex (Argentina). *Planetary and Space Science*, 57(5-6), 556-570. <https://doi.org/10.1016/j.pss.2008.12.001>.
- Giles, P. T. (2001). Remote Sensing and Cast Shadows in Mountainous Terrain. *Photogrammetric Engineering and Remote Sensing*, 67(7), 833-839.
- Golombek, M. P., Arvidson, R. E., Bell III, J. F., Christensen, P. R., Crisp, J. A., Crumpler, L. S., Ehlmann, B. L., Fergason, R. L., Grant, J. A., Greeley, R., Haldemann, A. F. C., Kass, D. M., Parker, T. J., Schofield, J. T., Squyres, S. W., & Zurek, R. W. (2005). Assessment of Mars Exploration Rover Landing Site Predictions, *Nature*, 436, 44-48, <https://doi.org/10.1038/nature03600>.
- Gupta, N., & Panchal, V. K. (2011). Artificial Intelligence for Mixed Pixel Resolution, *IEEE International Geoscience and Remote Sensing Symposium, Vancouver, BC*, 2801-2804. <https://doi.org/10.1109/IGARSS.2011.6049796>.
- Haberle, R. M., & Jakosky, B. M. (1991). Atmospheric Effects on the Remote Determination of Thermal Inertia on Mars. *Icarus*, 90(2), 187-204. [https://doi.org/10.1016/0019-1035\(91\)90100-8](https://doi.org/10.1016/0019-1035(91)90100-8).
- Haneberg, W. C. (2008). Using Close Range Terrestrial Digital Photogrammetry for 3-D Rock Slope Modeling and Discontinuity Mapping in the United States, *Bulletin of Engineering Geology and the Environment*, 67, 457-469.
- Hardgrove, C., Moersch, J., & Whisner, S. (2009). Thermal Imaging of Alluvial Fans: A New Technique for Remote Classification of Sedimentary Features. *Earth and Planetary Science Letters*, 285(1-2), 124-130. <https://doi.org/10.1016/j.epsl.2009.06.004>
- Head, J. W., Siebert, N., Pratt, S., Smith, D., Zuber, M., Solomon, S., McGovern, P. J., Garvin, J. B., & the MOLA Science Team (1998a). *Volcanic Calderas on Mars: Initial Views Using Mars Orbiter Laser Altimeter (MOLA) Data*. Paper presented at Lunar and Planetary Science Conference XXIX, Lunar and Planetary Institute, Houston. Abstract #1488.
- Head, J. W., Siebert, N., Pratt, S., Smith, D., Zuber, M., Solomon, S., McGovern, P. J., Garvin, J. B., & the MOLA Science Team (1998b). *Characterization of Major Volcanic Edifices on Mars Using Mars Orbiter Laser Altimeter (MOLA) Data*. Paper presented at Lunar and Planetary Science Conference XXIX, Lunar and Planetary Institute, Houston. Abstract #1322.
- Hellman, M., & Ramsey, M. (2004). Analysis of Hot Springs and Associated Deposits in Yellowstone National Park using ASTER and AVIRIS Remote Sensing. *Journal of Volcanology and Geothermal Research*, 135(1), 195-219.
- Heng, B. C. P., J. H. Chandler, & Armstrong, A. (2010). Applying Close Range Digital Photogrammetry in Soil Erosion Studies. *Photogrammetric Record*, 25(131), 240-265.

- Hildreth, W. (1979). The Bishop Tuff: Evidence for the Origin of Compositional Zonation in Silicic Magma Chambers. In C. E. Chapin, W. E. Elston (Eds.), *Ash-Flow Tuffs, Geological Society of America Special Paper* (Vol. 180, pp. 396-403).
- Hildreth, W. (2004). Volcanological Perspectives on Long Valley, Mammoth Mountain, and Mono Craters: Several Contiguous but Discrete Systems. *Journal of Volcanology and Geothermal Research*, 136(3-4), 169-98.
- Hildreth, W. & Mahood, G. A. (1986). Ring-Fracture Eruption of the Bishop Tuff. *Geological Society of America Bulletin*, 97, 396-403.
- Hill, D. (2006). Unrest in Long Valley Caldera, California, 1978-2004. *Geological Society of London, Special Publications*, 269(1), 1-24.
- Hobi, M. L., & Ginzler, C. (2012). Accuracy Assessment of Digital Surface Models Based on WorldView-2 and ADS80 Stereo Remote Sensing Data. *Sensors*, 12(5), 6347-6368. <https://doi.org/10.3390/s120506347>.
- Hodge, R., Brasington, J., & Richards, K. (2009). In-situ Characterization of Grain-Scale Morphology Using Terrestrial Laser Scanning. *Earth Surface Processes and Landforms*, 34, 954-968.
- Immitzer, M., Atzberger, C., & Koukal, T. (2012). Tree Species Classification with Random Forest Using Very High Spatial Resolution 8-Band WorldView-2 Satellite Data. *Remote Sensing*, 4(9), 2661-2693. <https://doi.org/10.3390/rs4092661>.
- Izett, G. A. (1982). The Bishop Ash Bed and Solme Older Compositionally Similar Ash Beds in California, Nevada and Utah. *U.S. Geological Survey Open-File Report*, 82-582.
- Jakosky, B. M. (1986). On the thermal properties of Martian fines. *Icarus*, 66(1), 117-124. [https://doi.org/10.1016/0019-1035\(86\)90011-4](https://doi.org/10.1016/0019-1035(86)90011-4).
- Johnson, J. R., Christensen, P. R., & Lucey, P. G. (2002). Dust Coatings on Basaltic Rocks and Implications for Thermal Infrared Spectroscopy of Mars. *Journal of Geophysical Research: Planets*, 107(E6). <https://doi.org/10.1029/2000JE001405>.
- Kahle, A. B. (1987). Surface Emittance, Temperature, and Thermal Inertia Derived from Thermal Infrared Multispectral Scanner (TIMS) Data for Death Valley, California. *Geophysics*, 52(7), 858-874.
- Kelleher, P. C., & Cameron, K. L. (1990). The Geochemistry of the Mono Craters-Mono Lake Islands Volcanic Complex, Eastern California. *Journal of Geophysical Research*, 95(B11), 17643-17.
- Kent, D. V., Hemming, S. R., & Turrin, B. D. (2002). Laschamp Excursion at Mono Lake? *Earth and Planetary Science Letters*, 197, 151-164.

- Kieffer, H. H. (2013). Thermal Model for Analysis of Mars Infrared Mapping. *Journal of Geophysical Research: Planets*, 118, 451-470.
- Kieffer, H. H., Neugebauer, G., Munch, G., Chase Jr., S. C., & Miner, E. (1972). Infrared thermal mapping experiment: The Viking Mars orbiter. *Icarus*, 16(1), 47-56. [https://doi.org/10.1016/0019-1035\(72\)90136-4](https://doi.org/10.1016/0019-1035(72)90136-4).
- Krosley, L. K., P. T. Shaffner, E. Oerter, & T. Ortiz (2006). *Digital Ground-Based Photogrammetry for Measuring Discontinuity Orientations in Steep Rock Exposures*. Paper presented at the 41<sup>st</sup> U. S. Symposium of Rock Mechanics, Golden, Colorado.
- Lachenbruch, A. H., Sass, J. H., Munroe, R. J., & Moses Jr., T. H. (1976). Geothermal Setting and Simple Heat Conduction Models for the Long Valley Caldera. *Journal of Geophysical Research: Solid Earth and Planets*, 81(5), 769-784, <https://doi.org/10.1029/JB081i005p00769>.
- Lane, S. N. (2003). The Measurement of River Channel Morphology Using Digital Photogrammetry. *The Photogrammetric Record*, 16(96), 937-961.
- Lane, S. N., James, T. D., & Crowell, M. D. (2000). Application of Digital Photogrammetry to Complex Topography for Geomorphological Research. *The Photogrammetric Record*, 16, 793-821. doi:10.1111/0031-868X.00152
- Lang, N. P., Tornabene, L. L., McSween Jr., H. Y., & Christensen, P. R. (2009). Tharsis-Sourced Relatively Dust-Free Lavas and their Possible Relationship to Martian Meteorites. *Journal of Volcanology and Geothermal Research*, 185(1-2), 103-115. <https://doi.org/10.1016/j.jvolgeores.2008.12.014>.
- Lorenz, R. D., & Scheidt, S. P. (2014). Compact and Inexpensive Kite Apparatus for Geomorphological Field Aerial Photography, With Some Remarks on Operations. *Journal of Geophysical Research*, 3(4), 1-8. <https://doi.org/10.1016/j.grj.2014.06.001>.
- Lowe, D. G. (2004). Distinctive Image Features from Scale-Invariant Keypoints. *International Journal of Computer Vision*, 60(2), 91-110. <https://doi.org/10.1023/B:VISI.0000029664.99615.94>.
- Malin, M. C., Bell III, J. F., Cantor, B. A., Caplinger, M. A., Calvin, W. M, Clancy, R. T., Edgett, K. S., Edwards, L., Haberle, R. M., James, P. B., Lee, S. W., Ravine, M. A., Thomas, P. C., & Wolff, M. J. (2007). Context Camera Investigation On Board the Mars Reconnaissance Orbiter. *Journal of Geophysical Research: Planets*, 112, E05S04. <https://doi.org/10.1029/2006JE002808>.
- Maltese, A., Capodici, F., Corbari, C., Ciruolo, G., La Loggia, G., & Sobrino, J. A. (2012). *Critical Analysis of the Thermal Inertia Approach to Map Soil Water Content Under Sparse Vegetation and Changeable Sky Conditions*. Paper presented at the 8531 Remote Sensing for Agriculture, Ecosystems, and Hydrology XIV, Abstract #85310T.

- Mars, J. C., & Lawrence, C. R. (2010). Spectral Assessment of New ASTER SWIR Surface Reflectance Data Products for Spectroscopic Mapping of Rocks and Minerals. *Remote Sensing of Environment*, 114(9), 2011-2025. <https://doi.org/10.1016/j.rse.2010.04.008>.
- Martin, T. Z. (2004). Thermal Correction of MRO CRISM Data Using Photoclinometry and Slope-dependent Thermal Models for the Martian Surface. *Bulletin of the American Astronomical Society*, 36, 1160.
- Matsushima, D., Asanum, J., & Kaihotsu, I. (2018). Thermal Inertia Approach Using a Heat Budget Model to Estimate the Spatial Distribution of Surface Soil Moisture over a Semiarid Grassland in Central Mongolia. *Journal of Hydrometeorology*, 19, 245-265. <https://doi.org/10.1175/JHM-D-17-0040.1>
- McEwen, A. S., Eliason, E. M., Bergstrom, J. W., Bridges, N. T., Hansen, C. J., Delamere, W. A., Grant, J. A., Gulick, V. C., Herkenhoff, K. E., Keszthelyi, L., Kirk, R. L., Mellon, M. T., Squyres S. W., Thomas, N., & Weitz, C. M. (2007). Mars Reconnaissance Orbiter's High Resolution Imaging Science Experiment (HiRISE). *Journal of Geophysical Research: Planets*, 112, E05S02. <https://doi.org/10.1029/2005JE002605>.
- Mellon, M. T., Feldman, W. C., & Prettyman, T. H. (2004). The Presence and Stability of Ground Ice in the Southern Hemisphere of Mars. *Icarus*, 169, 324-340.
- Mellon, M. T., McKay, C. P., & Grant, J. A. (2014). *Thermal Conductivity of Coarse and Fine Grained Soil Mixtures: Measurements and Mars applications*. Paper presented at 8th International Conference on Mars. Abstract #1107.
- Mellon, M. T. & Putzig, N. E. (2007). *The Apparent Thermal Inertia of Layered Surfaces on Mars*. Paper presented at Lunar and Planetary Science Conference XXXVIII. Lunar and Planetary Institute, Houston. Abstract #2184.
- Miller, C. (1985). Holocene Eruptions at the Inyo Volcanic Chain, California: Implications for Possible Eruptions in Long Valley Caldera. *Geology*, 13(1), 14-17.
- Morris, A. R., Anderson, F. S., Mougini-Mark, P. J., Haldemann, A. F. C., Brooks, B. A., & Foster, J. (2008). Roughness of Hawaiian Volcanic Terrains. *Journal of Geophysical Research*, 113(E12), E12007-1-E12007-20.
- Mougini-Mars, P. J. (2002). Prodigious Ash Deposits Near the Summit of Arsia Mons Volcano, Mars. *Geophysical Research Letters*, 29(16). <https://doi.org/10.1029/2002GL015296>.
- Mundt, J., Steutker, D., & Glenn, N. F. (2006). Mapping Sagebrush Distribution Using Fusion of Hyperspectral and Lidar Classification. *Photogrammetry Engineering and Remote Sensing*, 72(1), 47-54.
- Neugebauer, G., Munch, G., Kieffer, H., Chase Jr., S. C., & Miner, E. (1971). Mariner 1969 Infrared Radiometer Results: Temperatures and Thermal Properties of the Martian Surface. *Astronomical Journal*, 76(4), 719-728.

- Niethammer, U., James, M. R., Rothmund, S., Travelletti, J., & Joswig, M. (2012). UAV-based Remote Sensing of the Super-Sauze Landslide: Evaluation and Results. *Engineering Geology*, 128, 2-11. <https://doi.org/10.1016/j.enggeo.2011.03.012>.
- Notebaert, B., Verstraeten, G., Gover, G., & Poesen, J. (2009). Qualitative and Quantitative Applications of LiDAR Imagery in Fluvial Geomorphology. *Earth Surface Processes and Landforms*, 34, 217-231.
- Novack, T., Esch, T., Kux, H., & Stilla, U. (2011). Machine Learning Comparison between WorldView-2 and QuickBird-2-Simulated Imagery Regarding Object-Based Urban Land Cover Classification. *Remote Sensing*, 3(10), 2263-2282. <https://doi.org/10.3390/rs3102263>.
- Ozdemir, I., & Karnieli, A. (2011). Predicting Forest Structural Parameters Using the Image Texture Derived from WorldView-2 Multispectral Imagery in a Dryland Forest, Israel. *International Journal of Applied Earth Observation and Geoinformation*, 13(5), 701-710. <https://doi.org/10.1016/j.jag.2011.05.006>.
- Peacock, J. R., Mangan, M. T., McPhee, D., & Ponce, D. A. (2015). Imaging the Magmatic System of Mono Basin, California, with Magnetotellurics in Three Dimensions. *Journal of Geophysical Research: Solid Earth*, 120, 7273-7289. <https://doi.org/10.1002/2015JB012071>.
- Pelletier, J. D., Miasova, H., Harmon, R. S., & Overton, M. (2009). The Effects of Interdune Vegetation Changes on Eolian Dune Field Evolution: A Numerical-Modeling Case Study at Jockey's Ridge, North Carolina, USA. *Earth Surface Processes and Landforms*, 34(9), 1245-1254.
- Pratt, D. A., & Ellyett, C. D. (1979). The Thermal Inertia Approach to Mapping of Soil Moisture and Geology. *Remote Sensing of Environment*, 8(2), 151-168. [https://doi.org/10.1016/0034-4257\(79\)90014-2](https://doi.org/10.1016/0034-4257(79)90014-2).
- Presley, M. A., & Christensen, P. R. (1997). Thermal Conductivity Measurements of Particulate Materials: 2. Results. *Journal of Geophysical Research: Planets*, 102(E3), 6551-6566. <https://doi.org/10.1029/96JE03303>.
- Price, M. A. (2013). *Thermophysical Characteristics of Mantled Terrestrial Volcanic Surfaces: Infrared Analogs to Arsia Mons*, (Master's thesis). Retrieved from D-Scholarship. (<http://d-scholarship.pitt.edu/19741/>). PA: University of Pittsburgh.
- Price, M. A., Ramsey, M. S., & Crown, D. A. (2016). Satellite-based Thermophysical Analysis of Volcanoclastic Deposits: A Terrestrial Analog for Mantled Lava Flows on Mars. *Remote Sensing*, 8(2), 152.
- Putnam, W. (1937). *The Geology of the Mono Craters, California*, (Doctoral dissertation). Retrieved from Thesis Library. ([https://thesis.library.caltech.edu/7027/1/Putnam\\_wc\\_1937.pdf](https://thesis.library.caltech.edu/7027/1/Putnam_wc_1937.pdf)). CA: California Institute of Technology.



- Putzig, N.E., Barratt, E. M., Mellon, M. T., & Michaels T. I. (2013). *MARSTHERM: A Web-based System Providing Thermophysical Analysis Tools for Mars Research*. Paper presented at American Geophysical Union Annual Fall Meeting, P43C-2023.
- Putzig, N. E., & Mellon, M. T. (2007). Apparent Thermal Inertia and the Surface Heterogeneity of Mars. *Icarus*, 191(1), 68-94. <https://doi.org/10.1016/j.icarus.2007.05.013>.
- Ramsey, M.S. & Christensen, P.R. (1998). Mineral Abundance Determination: Quantitative Deconvolution of Thermal Emission Spectra. *Journal of Geophysical Research*, 103(B1), 577-596.
- Ramsey, M. S., & Crown, D. A. (2010). *Thermophysical and Spectral Variability of Arsia Mons Lava Flows*. Paper presented at the Lunar and Planetary Science Conference XLI, Lunar and Planetary Institute, Houston. Abstract #1111.
- Ramsey, M. S., & Crown, D. A. (2011). *Thermophysical Properties of Mantled Volcanic Surfaces: Can Terrestrial Analogues be used to Better Understand Martian Volcanism?* Paper presented at American Geophysical Union Fall Meeting. Abstract #P42C-06.
- Ramsey, M. S., Crown, D. A., & Harris, A. J. L. (2016). What Can Thermal Infrared Remote Sensing of Terrestrial Volcanoes Tell Us About Processes Past and Present on Mars? *Journal of Volcanology and Geothermal Research*, 311, 198-216. <https://doi.org/10.1016/j.jvolgeores.2016.01.012>.
- Ramsey, M. S., & Fink, J. H. (1996). Estimating Lava Vesicularity: A New Technique using Thermal Infrared Remote Sensing Data. *EOS, Transactions of American Geophysical Union*, 77(46), F803.
- Ramsey, M. S., Harris, A. J. L., & Crown, D. A. (2015). *Constraining the Rheologic Properties of Channelized Basaltic Flows on Earth and Mars*. Paper presented at American Geophysical Union Fall Meeting. Abstract #P31H-04.
- Richter, R. (1998). Correction of Satellite Imagery Over Mountainous Terrain. *Applied Optics*, 37(18), 4004-4015.
- Rosenburg, M. A., Aharonson, O., Head, J. W., Kreslavsky, M. A., Mazarico, E., Neumann, G. A., Smith, D. E., Torrence, M. H., & Zuber, M. T. (2011). Global Surface Slopes and Roughness of the Moon from the Lunar Orbiter Laser Altimeter. *Journal of Geophysical Research*, 116(E2), E02001.
- Rowan, L., Schmidt, R., & Mars, J. (2006). Distribution of Hydrothermally Altered Rocks in the Reko Diq, Pakistan Mineralized Area Based on Spectral Analysis of ASTER Data. *Remote Sensing of Environment*, 104(1), 74-87.
- Ruff, S. W., & Christensen, P. R. (2002). Bright and Dark Regions on Mars: Particle Size and Mineralogical Characteristics Based on Thermal Emission Spectrometer Data. *Journal of Geophysical Research: Planets*, 107(E12), 5119. <https://doi.org/10.1029/2001JE001580>.

- Russel, I. C. (1889). *Quaternary History of the Mono Valley, California*. U.S. Geological Survey Eighth Annual Report. 267-394.
- Sabol, D. E., Gillespie, A. R., McDonald, E., & Danillina I. (2006). *Differential Thermal Inertia of Geological Surfaces*. Paper presented at 2<sup>nd</sup> Annual International Symposium of Recent Advances in Quantitative Remote Sensing, University of Valencia, Torrent, Spain.
- Scheidt, S., Ramsey, M. S., & Lancaster, N. (2010). Determining Soil Moisture and Sediment Availability at White Sands Dune Field, New Mexico, from Apparent Thermal Inertia Data. *Journal of Geophysical Research: Earth Surface*, 115, F02019, <https://doi.org/10.1029/2009JF001378>.
- Scott, D. H., & Zimbelman, J. R. (1995). Geologic Map of Arsia Mons Volcano, Mars (Scale 1:1,000,000). (Geology Series Map 1-2480). USA: United States Geological Survey.
- Shepard, M. K., Campbell, B. A., Bulmer, M. H., Farr, T. G., Gaddis, L. R., & Plaut, J. J. (2001). The Roughness of Natural Terrain: A Planetary and Remote Sensing Perspective. *Journal of Geophysical Research*, 106, 32777-32795.
- Sheskin, D. J. (2011). *Handbook of Parametric and Nonparametric Statistical Procedures* (fifth edition). New York, NY, Chapman and Hall/CRC.
- Sieh, K., & Bursik, M. (1986). Most Recent Eruption of the Mono Craters, Eastern Central California. *Journal of Geophysical Research*, 91(B12), 12539-2571.
- Simurda, C. S., Ramsey, M. S., & Crown, D. A. (2015). *Thermophysical Characteristics of Lava Flows South of Arsia Mons*. Paper presented at Lunar and Planetary Science Conference XLVI, Lunar and Planetary Institute, Houston. Abstract #2332.
- Simurda, C. S., Ramsey, M. S., & Crown, D. A. (2016). *Surface Characteristics of the Daedalia Planum Lava Flow Field Derived from Thermophysical and Geological Mapping*. Paper presented at Lunar and Planetary Science Conference XLVII, Lunar and Planetary Institute, Houston. Abstract #2594.
- Smith, M. J., Chandler, J., & Rose, J. (2009). High Spatial Resolution Data Acquisition for the Geosciences: Kite Aerial Photography. *Earth Surface Processes. Landforms*, 34, 155–161. <https://doi.org/10.1002/esp.1702>.
- Snaveley, N., Grag, R., Seitz, S. M., & Szeliski, R. (2006). Photo Tourism: Exploring Photo Collections in 3D. *ACM Transactions on Graphics*, 25(3), 835-846. <https://doi.org/10.1145/1179352.1141964>
- Snaveley, N., Seitz, S. M., & Szeliski, R. (2007). Modeling the World from Internet Photo Collections. *Internal Journal of Computer Vision*, 80(2), 189-210. <https://doi.org/10.1007/s11263-007-0107-3>.

- Sturznegger, M., & Stead, D. (2009). Close-Range Terrestrial Digital Photogrammetry and Terrestrial Laser Scanning for Discontinuity Characterization on Rock Cuts. *Engineering Geology*, 106, 163-182.
- Tolt, G., Shimoni, M. & Ahlberg, J. (2011). A Shadow Detection Method for Remote Sensing Images Using VHR Hyperspectral and LIDAR Data. *2011 IEEE International Geoscience and Remote Sensing Symposium, Vancouver, BC*, 4423-4426. <https://doi.org/10.1109/IGARSS.2011.6050213>
- Thompson, M. M. (1958). Development of Photogrammetry in the U.S. Geological Survey. *Geological Survey Circular*, 218.
- Titus, T. N., Kieffer, H. H., & Christensen, P. N. (2003). Exposed Water Ice Discovered Near the South Pole of Mars. *Science*, 299, 1048–1051.
- Watanabe, H., & Matsuo, K. (2003). Rock Type Classification by Multi-band TIR of ASTER. *Journal of Geosciences*, 7(4), 347-358.
- Wentworth, C. K. (1922). A Scale of Grade and Class Terms for Clastic Sediments. *The Journal of Geology*, 30(5), 377-392.
- Westoby, M. J., Brasington, J., Glasser, N. F., Hambrey, M. J., & Reynolds, J. M. (2012). ‘Structure-from-Motion’ Photogrammetry: A Low-Cost, Effective Tool for Geoscience Applications. *Geomorphology*, 179, 300-314. <https://doi.org/10.1016/j.geomorph.2012.08.021>.
- Wilson, C., & Hildreth, W. (1997). The Bishop Tuff: New Insights from Eruptive Stratigraphy. *Journal of Geology*, 105, 407-439.
- Wood, S. H. (1983). *Chronology of Late Pleistocene and Holocene Volcanics, Long Valley and Mono Basin Geothermal Areas, Eastern California: Report 83 747-76*. Occidental College, Los Angeles, California: U.S. Geological Survey Final Technology Report: Geothermal Research Program
- U.S. Geological Survey (1998). Future Eruptions in California’s Long Valley Area – What’s Likely? [Fact Sheet-073-97]. Retrieved from <https://pubs.usgs.gov/fs/fs073-97/fs073-97.pdf>. Accessed 2018.
- U.S. Geological Survey (2013). USGS NED n38w120 1/3 arc-second 2013 1x1 degree ArcGrid. Retrieved from <http://nationalmap.gov/viewer.html>. Accessed 2014.
- U.S. Geological Survey (2018). USGS NED 1/3 arc-second n38w119 1x1 degree ArcGrid 2018. Retrieved from <https://nationalmap.gov/elevation.html>. Accessed 2018.
- Yamaguchi, Y., Kahle, A., Tsu, H., Kawakami, T., & Pniel, M. (1998). Overview of Advanced Spaceborne Thermal Emission and Reflectance Radiometer (ASTER). *IEEE Transactions on Geoscience and Remote Sensing*, 36, 1062-1071.

Zhang R., Tian, J., Mi, S., Su, H., He, H., Li, Z., & Liu, K. (2016). The Effect of Vegetation on the Remotely Sensed Soil Thermal Inertia and a Two-Source Normalized Soil Thermal Inertia Model for Vegetated Surfaces. *IEEE Journal of Selected Topics in Applied Earth Observations and Remote Sensing*, 9(4), 1725-1735. <https://doi.org/10.1109/JSTARS.2016.2521444>.